

## **Response of middle atmosphere chemistry and dynamics to volcanically-elevated sulfate aerosol: 3-D coupled model simulations**

Jassim A. Al-Saadi, R. Bradley Pierce, T. Duncan Fairlie, Mary M. Kleb, Richard S. Eckman, William L. Grose, Murali N. Natarajan, and Jennifer R. Olson

NASA Langley Research Center, Hampton, Virginia

### **Abstract**

The NASA Langley Research Center IMPACT model has been used to examine the response of the middle atmosphere to a large tropical stratospheric injection of sulfate aerosol, such as that following the June 1991 eruption of Mt. Pinatubo. The influence of elevated aerosol on heterogeneous chemical processing was simulated using a three-dimensional climatology of surface area density (SAD) developed using observations made from the HALOE, SAGE II, and SAM satellite instruments beginning in June 1991. Radiative effects of the elevated aerosol were represented by monthly-mean zonally-averaged heating perturbations obtained from a study conducted with the ECHAM4 GCM combined with an aerosol microphysical model. Two elevated-aerosol simulations were integrated for  $3\frac{1}{2}$  years following the volcanic injection. One simulation included only the aerosol radiative perturbation, and one simulation included both the radiative perturbation and the elevated SAD. These perturbation simulations are compared with multiple-year control simulations to isolate the relative contributions of transport and heterogeneous chemical processing in the middle-atmospheric response to volcanically elevated aerosol.

### **Introduction**

Accurate assessment and prediction of the atmospheric responses to changing composition are challenging, given the complexity of the Earth climate system, yet crucial for providing guidance in public policy-making decisions. Confident prediction of future atmospheric states requires the use of three-dimensional (3-D) general circulation models (GCMs), which simulate the global atmospheric circulation from fundamental principles, and a comprehensive formulation of relevant chemical processes. Because changes in atmospheric composition have the potential for altering climate, a significant modeling advance is the interactive coupling of the chemical processes with the dynamical and radiative processes, permitting the evolving constituent fields to influence the circulation and thermal structure of the simulated atmosphere. As summarized in the most recent Scientific Assessment of Ozone Depletion [World Meteorological Organization, 1999], "Ultimately, when computer resources allow and the GCM formulation is adequate, [fully coupled models] will be the preferred 3-D tool for assessment and prediction."

Recent studies have adopted different approaches in conducting chemistry-climate coupling studies over seasonal to decadal timescales, but demonstrate an evolution of modeling capabilities toward such 3-D coupled GCMs with fully interactive chemistry. Chipperfield [1999] has reported results of multi-annual simulations conducted with a 3-D chemical transport model (CTM) which combines a comprehensive photochemical model with analyzed meteorological fields, reproducing much of the observed daily, seasonal, and interannual variability in column ozone. This model implements a partial coupling in that the model-simulated ozone distribution is used to determine vertical transport. Although simulated (GCM-generated) rather than assim-

lated dynamical fields may be used with such CTMs to predict future atmospheric states [e.g., Eckman et al., 1995], full chemical-radiative coupling is not possible with CTM approaches. Various GCM studies have demonstrated components of fully-coupled model development while pursuing alternate approaches in applications to climate change studies. Parameterized or simplified chemistry schemes have been implemented within GCMs to conduct focused decadal forcing and response studies [Hansen et al., 1997; Shindell et al., 1998]. In particular, the model used by Shindell et al. [1998] may be considered partially coupled in that the changing abundances of ozone and other greenhouse gases influence the radiative balance, although resulting ozone transport changes are not calculated interactively. Steil et al. [1998] have shown first results of a 15-year integration of a 3-D GCM which includes a comprehensive chemistry scheme, although the model was not radiatively coupled (modeled constituent distributions were not used in radiative calculations). Several studies have presented results of radiatively coupled GCM simulations with comprehensive chemistry: Rasch et al. [1995] present multi-annual simulations with radiative coupling of the modeled stratospheric water vapor but not ozone, Zhao et al. [1997] present seasonal results for Northern-Hemisphere winter from a model with full chemical/radiative coupling, and Austin et al. [2000] present series of one-year simulations with ozone/radiative coupling. Considered together, such studies suggest that it is now feasible to conduct decadal simulations using interactive models with comprehensive chemistry.

The period following the June 1991 eruption of Mount Pinatubo in the Philippines provides an excellent case study for the application of dynamical/chemical atmospheric models in assessing chemical perturbations. Greatly elevated levels of sulfate aerosol spread globally throughout the stratosphere within a few months of the eruption, constituting what was probably the largest natural stratospheric perturbation of the 20th century [WMO, 1999]. Record-low column ozone amounts were observed following the eruption, and observational and modeling studies have at least partially attributed these declines to enhanced catalytic ozone destruction in the lower stratosphere mediated by heterogeneous chemical reactions on sulfate aerosol. Previous modeling studies which have included both comprehensive stratospheric chemistry schemes and some degree of chemical-radiative coupling have pursued different approaches in simulating the post-Pinatubo stratosphere. Tie et al. [1994] present results of a 3-year integration using a 2-D interactive chemical-dynamical-radiative model coupled with an aerosol microphysical model. Rosenfield et al. [1997] present 2<sup>1</sup>/<sub>2</sub>-year integrations conducted with a 2-D coupled chemical-dynamical-radiative model in which the time-dependent aerosol evolution is represented using satellite-observed extinction measurements. Zhao et al. [1997] present Northern Hemisphere results from 4-month integrations of a coupled 3-D GCM with different stratospheric aerosol loadings specified as monthly-mean surface area densities obtained from previous 2-D modeling studies. Chipperfield [1999] presents 6-year integrations of a 3-D CTM, driven by analyzed atmospheric fields and using modeled O<sub>3</sub> to calculate diabatic transport, in which liquid aerosol composition is determined using a monthly-mean H<sub>2</sub>SO<sub>4</sub> climatology.

The NASA Langley Research Center (LaRC) Interactive Modeling Project for Atmospheric Chemistry and Transport (IMPACT) model has been developed as a tool for assessing and predicting global changes in the composition, thermal structure, and circulation of Earth's atmosphere over decadal timescales. Our studies focus on natural and anthropogenic processes which have contributed to stratospheric ozone changes over the past two decades, the expected recovery in stratospheric ozone over the next several decades, and how the coupling between chemistry and climate might modify that expected recovery. The suitability of the model's dynamical characteristics for conducting such studies has been established using results of a 5-year coupled simula-

tion [Pierce et al., 2000]. The chemical climatology is briefly presented herein, and detailed chemical climatologies will be presented in the near future. These comparisons establish a reference model simulation which serves as a baseline for ongoing perturbation simulations.

In this paper we analyze the response of the atmosphere to a large volcanic eruption using multi-year coupled IMPACT model simulations. A new approach is the use of a 3-D time-dependent aerosol surface area density distribution reconstructed from observationally-based regressions. The stratospheric gas-phase chemistry scheme is similar to those used in the previous studies [Tie et al., 1994; Rosenfield et al., 1997; Zhao et al., 1997; Chipperfield, 1999]. The parameterization of heterogeneous reactions on sulfate aerosol is comparable to the studies of Tie et al. [1994] and Zhao et al. [1997], considering the two primary reactions (hydrolysis of  $\text{N}_2\text{O}_5$  and of  $\text{ClONO}_2$ ), but less comprehensive than the studies of Rosenfield et al. [1997] (which considers reactions of  $\text{HCl}$ ) and Chipperfield [1999] (which considers  $\text{HCl}$  and also bromine species). The representation of aerosol radiative characteristics differs widely in these studies. The 2-D studies [Tie et al., 1994; Rosenfield et al., 1997] include reasonably detailed representations of aerosol-induced radiative and photolytic changes (i.e., from absorption and scattering), the GCM study [Zhao et al., 1997] does not consider these effects, and the 3-D CTM study [Chipperfield, 1999] implicitly includes direct radiative effects through the analyzed temperature fields. In the present study, aerosol radiative effects are parameterized as monthly- and zonally-averaged heating anomalies obtained from a study in which a GCM was interactively coupled to an aerosol microphysics model [Stenchikov et al., 1998]. The horizontal resolution of the IMPACT model is approximately twice as fine as the other models, and the vertical resolution is comparable to the 3-D models and somewhat coarser than the 2-D models. The upper boundary of the model domain in the IMPACT model is above the mesopause, significantly higher than in the other 3-D models, which significantly improves representation of the stratospheric diabatic circulation [Lawrence, 1997; Rind et al., 1999; Pierce et al., 2000].

The present study is the first application of a 3-D coupled GCM with comprehensive chemistry to investigate the combined chemical, radiative, and dynamical response to volcanically-elevated stratospheric sulfate aerosol over a multi-year period. These simulations allow us to validate the modeled responses to a large transient perturbation and to assess the significance of such responses with respect to atmospheric interannual variability. Establishing such confidence is a prerequisite to conducting chemical sensitivity studies in the context of simultaneous atmospheric forcings (e.g., trace gas emissions, volcanic eruptions, El Niño/Southern Oscillation, Quasi-Biennial Oscillation, solar cycle).

The simulations conducted in this study are described next, followed by a discussion of basic model chemical characteristics and a description of the post-Pinatubo aerosol parameterizations used in the model. Results and conclusions follow. A description of the IMPACT model is given in Appendix A.

## Simulations

Two multiple-year control simulations, designated BL1 and BL2, were conducted to establish the baseline behavior and interannual variability of the IMPACT model. The BL1 and BL2 simulations differed only in the introduction of a temperature perturbation in the initial condition of the BL2 simulation. Two elevated-aerosol simulations were integrated for  $3\frac{1}{2}$  years following the volcanic injection; a simulation designated AH included only the aerosol radiative perturbation, and a simulation designated AHS included both the radiative perturbation and elevated SAD in

chemical calculations. These simulations allow assessment of the relative contributions of transport and heterogeneous chemical processing to the response of the middle atmosphere to elevated aerosol. The influence of aerosol absorption and scattering on photolysis rates is not simulated, however the influence of overhead column O<sub>3</sub> changes on photolysis is explicitly captured in these coupled simulations. Heterogeneous chemical reactions on PSC and sulfate aerosol surfaces are enabled in all simulations. A background “clean” aerosol SAD distribution [WMO, 1991] is used in the BL1, BL2, and AH simulations.

The baseline simulation BL1 was initialized on January 1 from a previous coupled IMPACT model simulation. The BL1 simulation was integrated for a total of 5 years, years 2-5 of which are analyzed here. Over this period, global mean temperatures remain stable (decrease of less than 0.01% per year), global mass-weighted N<sub>2</sub>O decreases by less than 0.05% per year, and global total ozone has a mean increase of 0.1% per year. The dynamical fidelity of this simulation is described in detail by Pierce et al. [2000].

A second baseline simulation (BL2) was conducted to allow a better assessment of model interannual variability. The BL2 simulation was initialized from the BL1 simulation on June 1 of Year 2 by superimposing a small (peak amplitude of 0.01 K) random temperature perturbation throughout the troposphere. The two simulations diverge significantly from each other within a month as these slight initial differences in tropospheric temperature yield differing tropospheric evolution, followed by differing forcing of the stratosphere. The BL2 simulation was integrated over the same 3<sup>1</sup>/<sub>2</sub>-year time period as the elevated-aerosol simulations.

The AH and AHS simulations were also both initialized from the BL1 simulation on June 1 of the second year, thus Year 2 corresponds to 1991 for obtaining SAD and aerosol heating values from the post-Pinatubo data sets. The use of calendar year as a label in presentation of model results refers only to these aerosol characteristics, as the model is not constrained by the dynamical characteristics of particular years.

## **Baseline chemical characteristics**

The fidelity of the IMPACT model representation of the distribution and seasonal evolution of chemical constituents is illustrated through select comparisons with observations. The dynamical climatology of the IMPACT model is presented in Pierce et al. [2000]. An in-depth chemical climatology will be presented elsewhere. For these background comparisons, seven-year mean climatologies are constructed from the 7 full years of baseline model simulations (Years 2-5 of BL1 and 3-5 of BL2). Each individual year of the BL1 and BL2 simulations is considered an independent realization of the “true” model climate.

## **Seasonal altitude-latitude comparisons**

Zonally- and seasonally-averaged distributions of modeled CH<sub>4</sub>, O<sub>3</sub>, and HCl are compared with Version 19 HALOE observations [Russell et al., 1993] for December-January-February (DJF) and June-July-August (JJA) seasons. The observed climatologies extend from 1993-1999 to reduce the impacts of the Pinatubo eruption. The observed climatologies are restricted to 50 degrees latitude in the winter hemisphere, due to poor sampling poleward of this latitude, and to altitudes with seasonal mean CH<sub>4</sub> mixing ratios of less than 1.8 ppmv, to filter out noise in the tropospheric retrievals. Differences are expressed in percent (model-HALOE)/HALOE. Estimated uncertainties in the HALOE measurements are 20% for CH<sub>4</sub> [Park et al., 1996], 15% for O<sub>3</sub> [Bruhl et al., 1996], and 15% to 20% for HCl [Russell et al., 1996].

Figure 1 shows observed, modeled, and the difference in CH<sub>4</sub> distributions for DJF (panels (a), (b), and (c)) and JJA (panels (d), (e), and (f)). The modeled DJF and JJA CH<sub>4</sub> distributions are generally in very good agreement with the HALOE observations with differences on the order of 10% or less, well within the quoted HALOE CH<sub>4</sub> uncertainty. Regions with larger differences include the subtropics between 10 mb and 0.1 mb, where model biases are positive in the winter hemisphere and negative in the summer hemisphere. The positive biases are largest in the Southern Hemisphere (SH) during JJA (figure 1(f)), exceeding 30% (0.2 ppmv). These biases are associated with seasonal asymmetries in the observed CH<sub>4</sub> distribution. Lofting of high equatorial CH<sub>4</sub> isopleths into the SH during DJF (figure 1(a)) and into the Northern Hemisphere (NH) during JJA (figure 1(d)) is due to the strong wintertime component of the Brewer-Dobson circulation which extends across the equator into the summer hemisphere. The observed upper stratospheric asymmetries are also partly associated with the semi-annual oscillation (SAO) which is lacking in the model simulation. The large positive biases (greater than 40%) found above 10mb over the summer poles are associated with localized regions of low CH<sub>4</sub> mixing ratios in the observed distribution. These low CH<sub>4</sub> mixing ratios persist into the fall equinox in both hemispheres but are absent during the spring equinox (not shown), so they are not likely to be associated with seasonal (winter) descent of low CH<sub>4</sub> mixing ratios from the mesosphere. Instead, they may reflect the advection of mesospheric air downward into the upper stratosphere by the secondary circulation associated with the equatorial SAO.

The model CH<sub>4</sub> mixing ratios are generally higher than observed by 10% in middle latitudes of the lower stratosphere during each hemisphere's summer season, although these differences are within the uncertainty of the HALOE measurement. This positive summertime middle latitude bias suggests either too little descent of lower CH<sub>4</sub> mixing ratios from the middle stratosphere during the previous winter, or too much transport of high CH<sub>4</sub> mixing ratios across the middle latitude tropopause which may arise due to the relatively coarse vertical resolution (3 km) of the model in this region. Although not apparent in figure 1 due to the restriction of HALOE CH<sub>4</sub> values to less than 1.8 ppmv, the model tropospheric CH<sub>4</sub> (approximately 1.7 ppmv) is lower than observed by HALOE (approximately 1.8 ppmv) because the surface boundary conditions for the model CH<sub>4</sub> and other trace gases are fixed at 1990 levels whereas CH<sub>4</sub> is observed to be increasing. In general, the differences between the observed and modeled CH<sub>4</sub> are consistent with a slightly weaker winter component of the Brewer-Dobson circulation in the IMPACT model and with relatively coarse vertical resolution of the model near the tropopause.

Figure 2 shows observed O<sub>3</sub>, modeled O<sub>x</sub>, and the differences for DJF (panels (a), (b), and (c)) and JJA (panels (d), (e), and (f)). The agreement between the modeled and observed ozone is very good in the upper stratosphere (20mb to 1mb) during DJF (figure 2(c)) and JJA (figure 2(f)), with a slight model negative bias of 10% or less which is within the uncertainty of the HALOE O<sub>3</sub> measurement. The modeled O<sub>x</sub> distribution shows peak mixing ratios of about 9.5 ppmv at 10mb in the tropics, in good agreement with the observed peak which ranges from 9.5 to 10 ppmv. The meridional gradients in O<sub>3</sub> are well represented in the model except at polar latitudes in the summer hemisphere between 10 mb and 50 mb, where the model overestimates O<sub>3</sub> by about 30% (2 ppmv). This overestimate probably arises due to model underestimates of the NO<sub>x</sub>-catalyzed O<sub>x</sub> destruction occurring in the lower stratosphere during periods of continuous sunlight, as discussed below with respect to column O<sub>3</sub>. There are small, but systematic, biases in the vertical gradients of stratospheric O<sub>3</sub> in the model during both DJF and JJA. The model O<sub>3</sub> distribution is systematically low in the upper stratosphere (1.0-10 mb) and high in the lower stratosphere (10-100 mb). This bias in the vertical gradient of O<sub>3</sub> is consistent with underestimates in the Brewer-

Dobson circulation which would lead to reduced vertical transport of air with low O<sub>3</sub> mixing ratios below the tropical peak at 10 mb (leading to overestimates in ozone) and of air with higher O<sub>3</sub> mixing ratios above the tropical peak (leading to underestimates in ozone). Large percentage overestimates in the lowermost stratosphere are likely due to the relatively coarse model vertical resolution near 100 mb. The overestimate above 1.0 mb is due to our comparison of modeled total Ox to observed O<sub>3</sub> which is not valid in the mesosphere where the Ox budget includes a significant contribution from atomic oxygen.

Figure 3 shows observed, modeled, and the difference in HCl distributions for DJF (panels (a), (b), and (c)) and JJA (panels (d), (e), and (f)). The modeled and observed HCl show similar increases with altitude, but the model reaches peak HCl mixing ratios slightly less than the 3.25 ppbv observed by HALOE. This slight underestimate in the HCl peak is because surface concentrations of chlorine source gases are fixed at 1990 values in the model simulations while they have continued to increase throughout most of the HALOE observational record. Lower stratospheric reductions in the modeled HCl at polar latitudes during NH (figure 3(b)) and SH (figure 3(e)) winter are evident and reflect the heterogeneous conversion of chlorine from HCl to ClO and Cl<sub>2</sub>O<sub>2</sub> during polar night. The agreement between modeled and observed HCl distributions is well within the 15-20% uncertainty of the HALOE HCl measurement throughout the stratosphere except below 20mb, where the model shows high biases in the tropics and low biases in middle latitudes during both DJF and JJA. These biases are associated with the lowest HCl mixing ratios and are again consistent with a weaker than observed Brewer-Dobson circulation in the model. A weak circulation would result in decreased upward transport of low HCl air into the tropical lower stratosphere, producing a positive tropical bias, and decreased downward transport of high HCl air into the middle latitude lower stratosphere, producing a negative middle latitude bias. Alternatively, the biases in HCl could be accounted for by overestimates in the extent of meridional mixing between the tropics and middle latitudes in the lowermost stratosphere. Overestimates in meridional mixing would result in increases in tropical HCl mixing ratios, decreases in middle latitude mixing ratios, and a general weakening of the subtropical meridional gradients. The modeled HCl meridional gradient is in fact weaker than observed; however, if excessive meridional mixing was the cause of the modeled HCl biases, we would expect to see an anti-correlated bias in CH<sub>4</sub>, which is not the case. In particular, there is no tropical negative bias in the model CH<sub>4</sub> (figures 1(c) and 1(f)) in spite of the fact that the model tropospheric CH<sub>4</sub> is lower than observed, as discussed above.

Most of the differences between the observed and modeled CH<sub>4</sub>, O<sub>3</sub>, and HCl are smaller than the quoted uncertainties in the HALOE observations but are systematic and appear to be associated with an underestimate in the strength of the model Brewer-Dobson circulation. To assess the overall quality of the IMPACT model circulation, we applied the assessment criteria used to evaluate candidate wind fields for the NASA Global Modeling Initiative (GMI) model [Douglass et al., 1999] to the IMPACT baseline simulation. The GMI tests focus on comparisons between modeled and observed N<sub>2</sub>O and CO<sub>2</sub> distributions and consider three different candidate wind and temperature fields. Two are GCM generated, from a middle-atmosphere version of the Community Climate Model 2 (CCM2) [Hack et al., 1994] and a middle-atmosphere version of the Goddard Institute for Space Studies (GISS) model [Hansen et al., 1983], and the third is an assimilated data set from the Goddard Earth Observing System Data Assimilation System (GEOS DAS) [Schubert et al., 1993].

The IMPACT model scored well overall on the GMI tests. The combined score for the IMPACT model was 0.61 out of 1.0, second only to the CCM2 which had a combined score of

0.73. Of particular interest are the results of the residual circulation tests in the upper and lower stratosphere (tests 2a and 2b in Douglass et al. [1999]). Test 2a assessed the lower stratospheric circulation by comparing the modeled N<sub>2</sub>O with in-situ Airborne Tunable diode Laser (ATLAS) [Podolske and Loewenstein, 1993] observations. The IMPACT model scored 0.84 out of 1.0 on test 2a, better than the best GMI candidate (CCM2) which scored 0.68. Test 2b assessed the middle to upper stratospheric circulation by comparing modeled N<sub>2</sub>O with Cryogenic Limb Array Etalon Spectrometer (CLAES) [Roche et al., 1993] observations. The IMPACT model scored 0.48 out of 1.0 on this portion of the test, higher than any of the GMI candidates (CCM2 was the best GMI candidate for this portion of the test with a score of 0.37). The low scores of all models on this component of the test result from failing to accurately reproduce the observed annual cycle of N<sub>2</sub>O in the middle to upper stratosphere. This failure is linked to errors in simulating the quantitative details of the annual cycle of the stratospheric circulation, particularly the winter component of the Brewer-Dobson circulation. These circulation deficiencies are likely responsible for the differences between the IMPACT model and HALOE observations discussed here. However, the GMI comparisons indicate that the stratospheric transport characteristics of the IMPACT model are quite good relative to other middle atmospheric models, and we can find no clear evidence for a systematic bias in the strength of the model Brewer-Dobson circulation.

### Column ozone

Climatological monthly-mean column ozone and yearly standard deviation of column ozone from the model and TOMS observations are shown in figure 4. TOMS data from 1984 (about 1½ years after the eruption of El Chichon) to 1990 are used for this pre-Pinatubo comparison. As discussed in Appendix B, signatures of quasi-periodic forcings not represented in the model have been removed from the TOMS data. The model (figure 4(b)) reproduces the major features and seasonal evolution of the observed (figure 4(a)) ozone distribution, including the tropical meridional minimum, the spring maximum and autumn minimum in NH high latitudes, and the spring high-latitude minimum and mid-latitude maximum in the SH. The model typically overestimates column O<sub>3</sub> in mid- to high-latitudes (figure 4(c)). Largest NH overestimates, in excess of 60 Dobson Units (DU) or about 15%, occur in polar spring and summer; one reason for this overestimate is that the maximum in high-latitude O<sub>3</sub> occurs approximately one month later in the model than observed. Largest SH overestimates, of up to 80 DU (25%), occur in sub-polar latitudes during the winter/spring period. The model underestimates tropical column O<sub>3</sub> by 10 to 20 DU, or less than 10% (figure 4(c)). This underestimate is primarily due to an underestimate of the tropospheric O<sub>3</sub> column; because tropospheric sources of nitrogen oxides are not represented in this version of the model, in-situ tropospheric O<sub>3</sub> production is too small. The corresponding standard deviation in monthly-mean column O<sub>3</sub> is shown in figures 4(d) for TOMS and 4(e) for the model. High-latitude spring is the time of largest variability in column O<sub>3</sub> due to variations in the evolution of the stratospheric winter polar vortex and the timing of the final warming. The largest model standard deviation, of about 75 DU, occurs in northern polar latitudes in March. The largest apparent NH deviation in TOMS, 30 DU in polar latitudes, occurs one month later, however TOMS can not view the north polar regions in March. Still, the modeled standard deviation exceeds that from TOMS in the northern polar regions throughout spring (figure 4(f)). Largest SH standard deviation values occur in polar latitudes in November in both the model and TOMS data, but the peak deviation in the model of about 35 DU is 20 DU smaller than that from TOMS data.

The largest difference in SH column O<sub>3</sub>, in sub-polar latitudes during the winter/spring period, contrasts with the relatively modest overestimate in the NH. A contributing factor to this

overestimate in the SH vortex collar region is a mid-stratospheric winter vortex which is consistently smaller than observed. Figure 5 shows the seasonal evolution of the 50 mb polar area where temperature is less than 195 K, obtained from seven model years and 21 years (1979-1999) of the National Center for Environmental Prediction (NCEP) reanalysis [Kalnay et al., 1996]. This temperature is a reference threshold for the formation of polar stratospheric clouds and subsequent heterogeneous chemical processing. At this altitude in the SH, the areal extent of the cold pool is about one-third smaller in the model than in the NCEP data (figure 5(a)), thus it is likely that the meridional extent of rapid springtime halogen-catalyzed O<sub>3</sub> loss is underestimated in the model. In the NH (figure 5(b)), the mean cold pool area in the model is somewhat larger than in the NCEP reanalysis, and the observed large interannual variability in NH vortex cold pool area is well represented by the model, however the mean cold pool area is approximately an order of magnitude smaller in the NH than in the SH.

The summer high-latitude overestimates in column O<sub>3</sub> are preceded by spring underestimates, particularly in the SH (figure 4(c)). Concurrent with these underestimates, figure 5 shows that in both hemispheres modeled cold polar temperatures persist for approximately one month later than observed. This persistence is a result of a delayed final warming in the model, which largely explains the modeled spring underestimate of polar column O<sub>3</sub>. These underestimates are within the standard deviation of both the model and TOMS, suggesting that the modeled polar winter/spring halogen-catalyzed O<sub>3</sub> destruction is reasonable in magnitude. Because model halogen source gas mixing ratios at the ground are fixed at 1990 levels, corresponding to the end of the TOMS record considered here, this apparent model underestimate of spring high-latitude O<sub>3</sub> may also be partially due to the increases in stratospheric halogen abundance from 1984 to 1990 inherent in TOMS observations.

The consistent overestimates of column ozone in mid- and high-latitude summer (figure 4(c)) are a result of O<sub>3</sub> overestimates in the lower stratosphere (figure 2) and are also characteristic of other middle atmospheric chemical models [Douglass et al., 1996; Steil et al., 1998; Chipperfield, 1999]. These overestimates may stem from one or both of two possible causes. First, the in-situ photochemical loss in the high-latitude mid-stratosphere may be underestimated. High-latitude O<sub>3</sub> destruction in the summer stratosphere is primarily driven by NO<sub>x</sub>-catalyzed cycles during periods of low aerosol loading [Johnston, 1975], and there is evidence that standard photochemical models underestimate the NO<sub>x</sub>-catalyzed loss when using the JPL97 rate compilation used in this version of the IMPACT model [Gao et al., 1999; Osterman et al., 1999]. A recent study [Portmann et al., 1999] shows that the use of updated rate recommendations for reactions influencing nitrogen oxide abundance yields decreases in column O<sub>3</sub> of 2-4% in mid-latitudes and up to 10% in high latitudes. A similar response in the IMPACT model would significantly reduce mid-latitude overestimates, but could not eliminate the higher latitude overestimates. The second possibility is that too much O<sub>3</sub> is transported poleward from mid-latitudes following the breakdown of the winter vortex. During winter the modeled O<sub>3</sub> abundance is too large in mid-latitudes of both hemispheres, probably due to either circulation deficiencies or coarse model vertical resolution near the tropopause as discussed above. This high O<sub>3</sub> is mixed poleward in spring during the vortex final warming, when the modeled column O<sub>3</sub> rapidly exceeds TOMS values. The overestimate then remains relatively constant throughout both NH and SH summer.

## Aerosol parameterizations

Heterogeneous chemical processing on stratospheric liquid sulfate aerosols is simulated by



considering the hydrolysis reactions of  $\text{N}_2\text{O}_5$  and  $\text{ClONO}_2$  (reactions 88 and 89, Table A3, Appendix A). Other heterogeneous reactions in liquid aerosol, such as those involving HCl and bromine species, are not included in this version of the IMPACT model. These reactions may be important under some atmospheric conditions, in particular the cold temperatures characteristic of the tropical lower stratosphere and high-latitude winter stratosphere [e.g., Tie et al., 1994; Lary et al., 1996; Solomon et al., 1996; Tie and Brasseur, 1996; Zhao et al., 1997]. Results from a preliminary version of the IMPACT model which includes the heterogeneous reactions of HCl with  $\text{ClONO}_2$  and HOCl in liquid aerosol will be briefly discussed where relevant.

### Surface area density climatology

To represent the global temporal evolution of sulfate aerosol in the post-Pinatubo period in a physically consistent manner, a three-dimensional climatology of aerosol surface area density (SAD) was developed using observations made from the HALOE, SAGE II, and SAM satellite instruments beginning in June 1991. Monthly regressions of SAD as a function of methane and potential temperature were performed separately for the Northern and Southern Hemispheres. During the June-December 1991 period, combined SAM II and SAGE II zonal mean SAD data were regressed against IMPACT model methane using ECMWF potential temperatures. (The IMPACT model  $\text{CH}_4$  was taken from a simulation which included a Pinatubo-aerosol heating perturbation, in order to represent the observed elevation in tropical stratospheric  $\text{CH}_4$  which followed the eruption; see discussion below.) From January 1992 onward, HALOE SAD was regressed against simultaneous HALOE  $\text{CH}_4$  and NMC analyzed potential temperature (used in the retrieval of HALOE data products). The resulting series of monthly regressions was interpolated in time, to fill in latitudes during periods not observed by the instruments, and then extrapolated with respect to  $\text{CH}_4$  to fill in  $\text{CH}_4$  values not observed by the instruments.

These climatological regressions, together with the 3-D model  $\text{CH}_4$  and potential temperature, are used to reconstruct an instantaneous 3-D SAD distribution. This approach allows large zonal asymmetries in SAD, observed particularly in the winter middle stratosphere [Harvey et al., 1999], to be properly represented. For example, figure 6 shows NH polar orthographic maps of  $\text{CH}_4$  and SAD at 50 mb in mid-March from the AHS simulation. The interior of the arctic vortex is characterized by low  $\text{CH}_4$  values (figure 6(a)) and low SAD values (figure 6(b)). An extrusion of high-latitude air (with low  $\text{CH}_4$  mixing ratio) into mid-latitudes is evident over northeast Asia. While this feature is also present in the SAD distribution, more striking is a corresponding filament of air with high SAD values on the eastern flank of this extrusion. Proper representation of heterogeneous chemical processing, particularly for heterogeneous reactions which have a strong temperature dependence, depends on capturing strong local enhancements which may result from such zonal structure.

Figure 7 shows September monthly-mean zonally-averaged cross-sections of reconstructed model SAD for 4 successive years of the AHS simulation. The peak SAD values descend, move toward high latitudes, and decrease in magnitude with time, in good agreement with observations [e.g., Thomason et al., 1997]. In September 1991 (figure 7(a)) peak SAD values of approximately  $24 \mu\text{m}^2/\text{cm}^3$  exist near 30 mb in tropical latitudes. Very low SAD values are found in the SH winter vortex, and somewhat elevated SAD values are found in NH mid- and high-latitudes, centered around 70 mb, following poleward and downward transport from the tropics. By September 1992 (figure 7(b)) the SAD peak has broadened to essentially all latitudes and has descended to 50mb in the tropics. In September 1993 (figure 7(c)) and 1994 (figure 7(d)), highest SAD values are found in the SH extratropics as the volcanic aerosol has descended to the lower stratosphere.

However, in September 1994 SAD values are still elevated over background levels by a factor of 2 throughout the stratosphere [Thomason et al., 1997].

### **Aerosol radiative characteristics**

The aerosol radiative forcing in the AH and AHS simulations was incorporated using monthly-mean zonally-averaged heating perturbations obtained from a study conducted with the ECHAM4 GCM [Stenchikov et al., 1998]. These radiative perturbations extend from the ground to 10 mb, include both solar and infrared contributions, and include modulation of the radiative forcing by the GCM-simulated cloud distribution. The radiative forcing data extend over a 2-year period following the eruption of Mount Pinatubo, thus it was necessary to extrapolate the heating perturbations to obtain the  $3\frac{1}{2}$  years of data required by the present simulations. At each altitude and latitude, a log-normal decay of the heating perturbations was assumed, and the decay rate determined by regression of the 2-year time-series of heating perturbations. Aerosol-induced changes in downward thermal and net solar radiative fluxes at the surface are not considered in the present simulations.

Figure 8 shows September aerosol radiative heating anomalies for the 4 years considered here, corresponding to the SAD distributions shown in figure 7. In September 1991 (figure 8(a)) peak aerosol heating rates of approximately 0.3 K/day at 30 mb in tropical latitudes coincide with the modeled peak in SAD (figure 7(a)). The small negative heating anomaly over the equator at 10 mb is due to a longwave cooling anomaly which is larger than the shortwave heating anomaly. Slight anomalies of approximately 0.01 K/day result in the tropical troposphere, including a net cooling in the lower troposphere and a net heating in the upper troposphere. By September 1992 (figure 8(b)) the peak heating anomaly has decreased to about 0.2 K/day, and net heating has extended into mid- and high-latitudes of the lower stratosphere following the poleward and downward transport of the aerosol particles (figure 7(b)). The stratospheric heating anomaly decays exponentially during the latter 2 years, with peak values falling to approximately 0.05 K/day in 1993 (figure 8(c)) and 0.01 K/day in 1994 (figure 8(d)). As noted by Stenchikov et al. [1998], heating anomalies of about 0.3 K/day persist in the equatorial region through August 1992, similar to previous studies but possibly on the high side of the reported range, and their simulations yield a peak increase in stratospheric temperature of 3-4 K, in good agreement with observations.

## **Results**

The response to elevated aerosol is presented in this section. Responses to heating and increased surface area density are considered separately where relevant for distinguishing the effects of altered circulation and photochemistry. Particular focus is placed on quantifying responses which are significant with respect to interannual variability. For many of the results shown here, the reference (pre-volcanic) atmospheric state is represented by monthly-averaged 7-year climatologies of the BL1 and BL2 simulations, as in the above discussion of baseline chemical characteristics. The yearly standard deviations from these climatologies are used to judge the significance of post-volcanic responses; responses larger than twice the baseline standard deviation (2-sigma) are considered significant. For time-dependent comparisons, these baseline monthly means and standard deviations are used to construct annually-repeating composite baselines, denoted as BLC in the figures and discussion.

## Column Ozone Response

Figure 9 shows time series of monthly-mean zonal average column ozone as a function of latitude from the BL1 baseline (figure 9(a)) and AHS elevated aerosol (figure 9(b)) simulations, and the difference between the two (figure 9(c)). The large NH spring high-latitude variability shown in figure 4(e) is a consequence of large interannual differences apparent in the baseline simulation (figure 9(a)). With elevated aerosol (figure 9(b)), decreases in column O<sub>3</sub> are apparent in tropical latitudes during Years 2 and 3 and in the collar of high O<sub>3</sub> equatorward of the SH polar vortex during Years 3 and 4. Relatively persistent declines of over 10 Dobson Units (DU) are apparent in both northern and southern mid- to high-latitudes through 1992 and 1993 (figure 9(c)). Very large high-latitude differences, both positive and negative, result during almost every winter/spring period in this comparison of individual simulation years (figure 9(c)); these differences largely reflect model interannual variability rather than a consistent response to elevated aerosol.

The time evolution of near-global (from 60°S to 60°N) mean area-weighted column ozone is shown in figure 10 for the two elevated-aerosol simulations, the annually-repeating composite baseline simulation, and observational data from the TOMS instrument. The TOMS data are adjusted for QBO, ENSO, and solar cycle (Appendix B); during this time period the effect of these adjustments on the near-global average is a decrease of 4 DU in mid-1991, diminishing to no net effect by late 1992, and an increase fluctuating between 0 and 2 DU in 1993 and 1994. The dark shading indicates the baseline 7-year standard deviation, and the light shading shows twice the standard deviation. All model results shown in figure 10 have been incremented by 3.2 DU, the mean amount by which the near-global averages of the 7-year mean column O<sub>3</sub> computed from the model and TOMS data differ. The elevated-aerosol simulations have initial column O<sub>3</sub> values that are lower than the mean because they were initialized from the BL1 simulation during a month in which anomalously low column O<sub>3</sub> was experienced. During the first year following the eruption, the simulation with elevated aerosol heating (AH) yields a decline in column O<sub>3</sub> (relative to the baseline) of 2-3 DU, which compares very well with TOMS data. Although this good agreement is primarily due to the initial offset of the AH simulation relative to the composite baseline, the calculated decline is slightly larger than the 2-sigma envelope. The AH simulation response diminishes after mid-1992 and decays to within the 2-sigma variability. The simulation with aerosol heating and SAD (AHS) predicts a large O<sub>3</sub> decrease of approximately 7 DU during the first year following the eruption, about 5 DU larger than the decrease apparent in the TOMS record. From late 1992 through 1993, the AHS simulation continues to predict a decrease of 6-8 DU, comparing very well with TOMS data. During 1994 the AHS simulation predicts a near-recovery in column O<sub>3</sub>, again in good agreement with TOMS observations.

Over the simulation period, the largest differences between the observed and modeled (AHS) near-global ozone occur in the latter half of 1991 and in mid-1992, during which times the model predicts lower O<sub>3</sub> than observed. The model's interannual variability in the near-global average is highest during the May-June period, and the differences between the AHS simulation and TOMS during these months in 1992 appear larger than the variability. (However, the AHS-simulated response is a single realization of the "true" model response, and it is possible that 2-sigma envelopes of multiple model realizations might overlap with TOMS, rendering these differences insignificant.) There are several possibilities for the model overestimate of the O<sub>3</sub> decline in the first year following the eruption. Through late 1991 it is possible that some of the difference is attributable to the initialization during a period of anomalously low model O<sub>3</sub>, as discussed above. Other possibilities are overestimates of the aerosol radiative heating and/or chemical effects. Because the radiative perturbation decays rapidly in the second year, a heating overestimate could explain

why the observed O<sub>3</sub> loss is well represented by the heating anomaly alone (AH) during the first year. Alternatively, an overestimate of the chemical response when SAD is greatly elevated would yield overestimates of O<sub>3</sub> depletion during the first year of the AHS simulation. These possibilities will be addressed throughout the paper.

The responses of column ozone to elevated aerosol within different latitude bands are presented as time series of monthly-mean anomalies in figure 11. These area-weighted anomalies are calculated with respect to the 7-year composite baseline (BLC), and dark and light shading indicate the baseline 1-sigma and 2-sigma envelopes. The near-global average (figure 11(a)) presents the information shown in figure 10 as percentage anomalies. The column O<sub>3</sub> decrease in the AH simulation grows to 1.5% by early 1992 and remains within a marginally-significant 1% through 1992. The decline in the AHS simulation grows to almost 4% by early 1993, then decays to a marginally-significant 1% by mid-1994. The AHS simulation yields a tropical column O<sub>3</sub> decline (figure 11(b)) which rapidly peaks at 5% in late 1991, decays to a marginally-significant 2% by mid-1993, and thereafter remains at 1-2%, significant only during the months November through February. The tropical response of the AH simulation is very similar during the first few months following the injection, then falls to approximately half the AHS response by early 1993, after which the response diminishes to within the background variability. The model interannual variability in mid-latitudes (figures 11(c) and 11(d)) is approximately 2 times larger than in the tropics, and the heating response (AH) is typically within the interannual variability. However, the AHS simulation shows significant declines in mid-latitude column O<sub>3</sub> in both hemispheres, of up to 4% in the NH and 5% in the SH, with largest declines occurring from late 1992 through 1993. Highest values of SAD in the extratropical lower stratosphere were observed in the latter part of 1992, following poleward transport and descent of the aerosol particles, thus accounting for the timing of this peak photochemical response. The variability in high latitudes (figures 11(e) and 11(f)) has a strong seasonal variation, with highest variability in spring attributable to the breakdown of the stratospheric winter vortex. The NH high-latitude O<sub>3</sub> response (figure 11(e)) is approximately 50% larger than the mid-latitude response, however the high-latitude response is not significant with respect to the variability. The SH high-latitude response (figure 11(f)) includes maximum declines in excess of 10% in late 1992 and declines of over 5% persisting through 1993. These responses tend to be significant mainly during summer and autumn seasons. These model results suggest that the initial (first three months) decline in O<sub>3</sub> following the injection is largely due to enhanced tropical upwelling resulting from the increase in radiative heating in the lower stratosphere, while the longer-term response is due to both the altered circulation and increased photochemical destruction.

The response of column ozone during the post-Pinatubo period as derived from TOMS data (adjusted as in Appendix B) within these same latitude bands is shown in figure 12. These area-weighted anomalies are calculated with respect to the 1984-1990 mean presented in figure 4(a), and dark and light shading indicate one and two times the monthly standard deviation from these years. This analysis of TOMS observations compares very well with the similar study of Randel et al. [1995]. The decline in the near-global response (figure 12(a)) becomes significant at 1% in early 1992, grows to 3% by late 1992, remains between 2 and 3% through 1993, and diminishes to a marginally-significant 1% by mid-1994. As discussed for figure 10, the observed decrease is smaller than modeled (AHS simulation) until late 1992 and is very similar thereafter. In the tropics (figure 12(b)) a significant response is observed only in mid-1992, with a decrease of about 3%, and mid- to late-1993 with a decrease of about 2%. The modeled response (figure 11(b)) is very similar during these periods, although the model yields a large decline in late 1991 which is

not apparent in the TOMS observations. In NH mid-latitudes (figure 12(c)) a decrease of about 3% is observed in 1992 and from mid-1993 to mid-1994, mainly significant when interannual variability is a minimum during the summer and autumn seasons. This level of decline is similar to that predicted by the model (figure 11(c)). However during the winter and spring of 1992-1993 a large decline of up to 10% is observed, larger than resulted from the model during any mid-latitude winter/spring. This observed anomaly is discussed below. The only significant response observed in SH mid-latitudes (figure 12(d)) is a decrease of 2-4% from late 1993 to early 1994, somewhat smaller than the modeled decrease of up to 5% (figure 11(d)). Declines of 3% are also observed in October 1992 and May-September 1993, but the interannual variability is of similar magnitude during these months. During the summer months when TOMS is able to observe polar latitudes, consistent declines of approximately 10% are apparent in the NH in 1993 (figure 12(e)) and the SH from 1992-1994 (figure 12(f)), however the variability in the SH is too large to consider the decreases significant.

The large column O<sub>3</sub> decrease in NH mid-latitudes in the spring of 1993 shown in this analysis of TOMS data is also shown in other observationally-based studies [e.g., Randel et al., 1995; WMO, 1999, figures 4-14 and 4-15]. Tie et al. [1997] use a 2-D model to show the temperature sensitivity of winter high-latitude heterogeneous reaction rates and resulting O<sub>3</sub> loss in the post-Pinatubo period. They show that because winter 1991/92 was warmer than average and winter 1992/93 was colder than average, using actual temperatures rather than multi-year averages results in 3% less column O<sub>3</sub> depletion in spring 1992 and 3% more depletion in spring 1993. Hadjinicolaou et al. [1997] use a CTM driven by analyzed meteorological fields to show that the majority of the large decrease in spring 1993 may be accounted for by transport processes. Chipperfield [1999] shows that a CTM driven by analyzed fields and a representative aerosol distribution reproduces the observed spring 1993 O<sub>3</sub> decline, and further concludes that chemical processing on sulfate aerosol is not important for producing this response. In the present analysis this observed O<sub>3</sub> decrease is much larger than the two-sigma standard deviation computed from 1984-1990 TOMS observations. An unresolved issue is whether the presumed transport anomaly (implicitly included in the CTM studies through use of analyzed fields) is a response to the volcanic aerosol perturbation. Although the present study does not show such a large transport anomaly, a GCM simulation cannot represent the observed dynamical evolution of a particular year, and an ensemble of simulations might yield this response as one possible outcome.

Following Angell [1997(a)], Table 1 summarizes the time and size of maximum post-Pinatubo column O<sub>3</sub> anomalies within global, tropical, and NH mid-latitude regions as determined from the present analyses (e.g., figures 11 and 12) and analysis of ground-based Dobson network data [Angell, 1997(a)]. Secondary maxima are included for the model results where relevant. The largest modeled global decline is in good agreement with the present TOMS analysis and is larger than in the ground-based analysis but occurs at about the same time. In the tropics, the model minimum appears too large and too soon; a second minimum of 4.7% 13 months post-eruption is in reasonable agreement with the present TOMS analysis, but is still significantly larger and occurs sooner than in the ground-based estimate. Angell [1997(a)] does however show secondary tropical minima at 3 and 15 months post-eruption that are not significant at a 95% confidence level. This episodic nature of the tropical decline is also noted by Randel et al. [1995]. It appears that the derived maxima of individual episodes may be sensitive to the techniques used for removal of quasi-periodic tropical signals. In NH mid-latitudes, there is very good agreement of the model with observations in the timing of the peak decline, but the largest anomaly in the model is smaller than in Angell [1997(a)] (although in agreement within the uncertainty estimates), and

significantly smaller than the present TOMS analysis, as discussed above.

The results shown in figure 11 also compare favorably with previous modeling studies. Tie et al. [1994] and Rosenfield et al. [1997] show near-global peak reductions of about 3% in the latter half of 1992, versus present estimates of about 4%. Rosenfield et al. [1997] predict column O<sub>3</sub> decreases of 2-3% in low latitudes, with approximately half the decline due to circulation changes, and Tie et al. [1994] estimate peak tropical declines of about 3%. The IMPACT simulations yield a larger peak tropical decline, of up to 5%, but also show that approximately half the decline is due to circulation changes through much of 1992. Rosenfield et al. [1997] predict up to 8% decreases in mid-latitudes and 10-12% decreases in high latitudes, and larger decreases in SH rather than NH mid-latitudes. Tie et al. [1994] predict similar NH declines, but do not present SH results. Mid-latitude results from the present simulations compare well with these studies.

The recent study of Portmann et al. [1999] addresses the influence of updated reaction rate coefficients important in determining the stratospheric NO<sub>x</sub> abundance. Their results show that modeled photochemical O<sub>3</sub> depletion with post-Pinatubo aerosol levels may be reduced by approximately 30% at 45°N latitude with these updated rates. If comparable changes occur in low latitudes, such a reduction in modeled photochemical depletion would improve the present comparison with observations in tropical and global averages.

### **Circulation response**

The influence of elevated aerosol on the middle atmospheric circulation is illustrated using the annually-averaged Transformed Eulerian Mean (TEM) circulation. Although large aerosol effects on the TEM circulation are observed in monthly and seasonal averages, the interannual variability of the model TEM circulation is also large over these shorter timescales. Thus an annual average is used to examine persistent circulation changes unobscured by short-period variability.

The mean TEM circulation for the first year following the eruption, June of Year 2 (1991) through May of Year 3 (1992), is shown in figure 13. Figure 13(a) shows the TEM circulation from the AHS simulation; coherent northern and southern hemisphere cells are apparent in this annual mean. The corresponding vertical (W) component (figure 13(b)) clearly shows tropical ascent (positive W) and extratropical descent (negative W). Figure 13(c) shows the TEM anomaly due to elevated aerosol, defined by subtracting the BLC from the AHS results. Regions where the response exceeds the interannual one- and two-sigma standard deviation are shaded to indicate where the aerosol response is significant. Significant strengthening of both the Southern and Northern Hemisphere circulation occurs throughout the stratosphere and extends into the lower mesosphere. Comparable strengthening results in both hemispheres, but the mid-latitude response does not exceed the 2-sigma variability in the upper stratosphere of the NH. The aerosol-induced anomaly in the TEM W component is shown in figure 13(d). Elevated aerosol results in significant increases in the upward motion throughout the tropical stratosphere. Enhanced extra-tropical downward motion is significant throughout the SH stratosphere and in the NH mid-latitude lower stratosphere and polar upper stratosphere. These vertical velocity anomalies are in broad agreement with the circulation changes shown in figure 13(c).

The strengthening of the TEM circulation is primarily due to the parameterized aerosol heating perturbation, which represents the increase in radiative heating resulting from absorption and scattering by the aerosol. This radiative heating perturbation yields enhanced tropical upwelling, which is compensated by increased poleward and downward motion in the extratropics.

The aerosol-induced TEM circulation anomalies during the second and third years following the eruption (not shown) have a similar distribution to those shown in figure 13 but diminish in

magnitude. Significant circulation anomalies still exist in the third year, although the anomalies are significant mainly in the upper stratosphere.

### Altitude-latitude response

Basic characteristics of the modeled response to elevated aerosol are illustrated with altitude versus latitude cross-sections for a single season one year following the eruption: June-July-August (JJA) of model Year 3, corresponding to 1992. Shown in figure 14 are seasonally-averaged temperature, CH<sub>4</sub>, and O<sub>3</sub> (panels (a)-(c)) from the AHS simulation, and corresponding anomalies with respect to the composite baseline (AHS minus BLC) (panels (d)-(f)). Light and dark shading indicate locations where the anomaly is larger than one and two times the yearly standard deviation, respectively. Significant warm anomalies result in low- and mid-latitudes throughout the stratosphere (figure 14(d)), maximizing at about 5 K (2.5%) in the tropical middle stratosphere. This warming is due to the radiative heating anomaly resulting from aerosol absorption and scattering. Marginally significant warm anomalies also result in the SH polar upper stratosphere, of about 2K, and in the NH polar lower stratosphere, of about 1 K. The main response in methane (figure 14(e)) is an increase throughout the low-latitude stratosphere, with peak increases of about 0.08 ppmv (10%) in the extra-tropical mid-stratosphere of both hemispheres. This increase is due to the enhanced tropical upwelling associated with the aerosol radiative heating. Because the methane mixing ratio decreases with altitude (figure 14(b)), upward motion increases the methane mixing ratio. The most significant O<sub>3</sub> response (figure 14(f)) is a decline of up to 0.40 ppmv (about 8%) in the tropical lower stratosphere, and a significant decline of about 0.10 ppmv exists throughout the NH lower stratosphere during this period.

The maximum warm anomaly shown in figure 14(d), 5 K at 50 mb in tropical latitudes, is slightly larger than that shown in other studies. Labitzke and McCormick [1992] show peak warm anomalies of 3.5 to 4 K in the tropical lower stratosphere during late 1991. Angell [1997(b)] uses radiosonde data to derive a peak equatorial temperature anomaly of  $3.0 \pm 0.7$  K, occurring at 50 mb 6 months after the eruption; this anomaly decays to about 2 K 15 months after the eruption, a time period comparable to figure 14(d). The Rosenfield et al. [1997] model study yields largest warmings of about 2.5 K in the tropical lower stratosphere in mid-1992. During this time Rosenfield et al. [1997] also show O<sub>3</sub> changes at 15°N latitude including decreases of greater than 0.3 ppmv below 28 km and increases of about 0.3 ppmv above 28 km. Current results (figure 14(f)) show a decrease of 0.4 ppmv at 30 mb (about 25 km), but no significant change above 10 mb (about 32 km); up to 0.1 ppmv of the O<sub>3</sub> increase above 28 km shown by Rosenfield et al. [1997] is attributable to aerosol-induced photolysis changes which are only partially included in the present results, as noted above.

The influence of aerosol on nitrogen species is shown in figure 15. The main significant response in NO<sub>y</sub> (figure 15(a)) is a decrease in the tropical middle stratosphere of over 0.8 ppbv or 15% (figure 15(e)). Marginally significant increases of about 0.4 ppbv occur in the tropical and SH extratropical upper stratosphere and in the SH high-latitude lower stratosphere. The NO<sub>y</sub> response, positive above the altitude of the peak NO<sub>y</sub> mixing ratio (figure 15(a)) and negative below the NO<sub>y</sub> peak, is a result of the circulation changes associated with increased tropical upwelling. HNO<sub>3</sub> (figure 15(b)) maximizes in the winter (i.e., SH) high-latitude stratosphere, and is significantly enhanced with elevated aerosol at all latitudes except for summer (i.e., NH) high-latitudes (figure 15(f)). Largest increases occur in the winter hemisphere, exceeding 2.4 ppbv (100%) in polar latitudes. These increases are a direct response to the heterogeneous reactions on sulfate aerosol, which produce HNO<sub>3</sub>. The hydrolysis of N<sub>2</sub>O<sub>5</sub> (reaction 88, Table A3) is effi-

cient throughout the lower stratosphere, and the hydrolysis of ClONO<sub>2</sub> (reaction 89, Table A3) becomes important at the cold temperatures characteristic of the winter polar stratosphere. Corresponding decreases are apparent in NO<sub>x</sub> and N<sub>2</sub>O<sub>5</sub> (figures 15(g) and 15(h)); because N<sub>2</sub>O<sub>5</sub> is a nighttime stratospheric reservoir for NO<sub>x</sub>, both species are depleted as nitrogen partitioning is shifted toward HNO<sub>3</sub>. N<sub>2</sub>O<sub>5</sub> concentrations are small in latitudes experiencing continuous sunlight (e.g., figure 15(d)), and temperatures are too warm for ClONO<sub>2</sub> hydrolysis to be efficient, which explains the lack of a response in HNO<sub>3</sub> in the summer polar stratosphere (figure 15(f)).

The influence of aerosol on chlorine species is shown in figure 16. Shown are Cly, HCl, Clx, and ClONO<sub>2</sub> (panels (a)-(d)) from the AHS simulation, and corresponding aerosol-induced anomalies (panels (e)-(h)). Significant responses in Cly (figure 16(e)) include a decrease of over 0.075 ppbv (5%) in the tropical stratosphere and increases of up to 0.075 ppbv (5%) in the SH mid-latitude lower stratosphere and 0.025 ppbv in the NH extra-tropical lower stratosphere. These responses in Cly again reflect circulation changes; because Cly increases with altitude (figure 16(a)), enhanced tropical upwelling lowers tropical Cly mixing ratios, while corresponding extra-tropical downwelling (e.g., figure 13(d)) increases mixing ratios in the extratropical lower stratosphere. These downwelling signatures are also weakly apparent in CH<sub>4</sub> (figure 14(e)) and NO<sub>y</sub> (figure 15(e)). The signature is stronger in Cly because Cly has a larger vertical gradient in the lower stratosphere, where production of Cly from source gas precursors becomes significant. Elevated aerosol decreases HCl in the lower stratosphere exclusive of polar latitudes (figure 16(f)); decreases of about 0.05 ppbv (5%) result in the summer hemisphere (i.e., NH) and of over 0.10 ppbv (10%) in the winter hemisphere (i.e., SH). Significant decreases also occur in low- and mid-latitude ClONO<sub>2</sub> (figure 16(h)), with largest decreases of 0.10 ppbv (10%) in the tropical lower stratosphere. These decreases in HCl and ClONO<sub>2</sub> in the lower stratosphere are associated with increases in Clx (figure 16(g)), with largest increases of about 0.10 ppbv (100%) in winter (i.e., SH) mid-latitudes. In the upper stratosphere, there is a significant increase in HCl of up to 0.05 ppbv (2%) in SH extra-tropics (figure 16(f)), and compensating decreases in Clx and ClONO<sub>2</sub> (figures 16(g) and (h)). Here, the elevated CH<sub>4</sub> levels induced by the aerosol (figure 14(e)) shift chlorine partitioning toward HCl. Large changes are apparent in all chlorine species in the winter polar stratosphere, however the variability is also large there, and the only significant changes are an increase in HCl between 10 and 20 mb (figure 16(f)), increases in Clx at 10 mb and below 80 mb (figure 16(g)), and decreases in ClONO<sub>2</sub> above 15 mb and near 40 mb (figure 16(h)). The chemical response to elevated aerosol is difficult to discern in this region because significant heterogeneous processing on PSC surfaces normally occurs here. As shown in figure 16, significant responses are thus mainly expected at the boundaries of the region where PSCs normally form, where cool temperatures increase the efficiency of the ClONO<sub>2</sub> hydrolysis reaction (reaction 89 in Table A3). Heterogeneous reactions not included in the model, such as reactions of HCl with ClONO<sub>2</sub> and with HOCl, are also likely to have their largest effect in these regions (e.g., Zhao et al. [1997]).

### Globally-averaged altitude-time response

In this section we show the globally-averaged response to elevated aerosol with respect to altitude and time. Responses are shown as anomalies which are derived by computing global (area-weighted) averages at each model pressure level and time for each simulation, and then taking the difference between two simulations. Specifically, heating-only anomalies are calculated by subtracting baseline (BLC) from AHS averages, SAD-only anomalies by subtracting AH from AHS averages, and combined aerosol anomalies by subtracting BLC from AHS averages. Changes in



temperature, CH<sub>4</sub>, and Ox are shown first, followed by changes in the nitrogen and chlorine families.

Figure 17 shows anomalies of temperature, methane, and odd oxygen for both the combined (panels (a)-(c)) and heating-only (panels (d)-(f)) perturbations. The combined thermal response to elevated aerosol (figure 17(a)) is a warming throughout the stratosphere, with a peak warming at 50 mb which reaches 4K (2%) during the first half of 1992 and decays to less than 0.5K by the end of 1993. Rosenfield et al. [1997] estimate the largest near-global (65S-65N) temperature change as a warming of almost 1.5 K below 50 mb, in comparison with the present estimate of 4 K at 50 mb. Angell [1997(b)] estimates the largest global temperature anomaly in the 100-50 mb layer to be  $1.1 \pm 0.3$  K 6 months after the eruption; present estimates are 2 K at 100 mb and up to 4 K at 50 mb, thus a 100-50 mb layer average would exceed the Angell [1997(b)] estimate. There is no consistent thermal response in the troposphere (figure 17(a)), although episodic cooling of up to 0.5 K occurs in the latter half of 1992 and mid-1993. Previous studies have shown declines of from 0.2-0.5 K in 1992 and smaller declines in 1993 [McCormick et al., 1995]. It is possible that we underestimate tropospheric cooling due to the neglect of aerosol-induced changes in radiative fluxes at the surface [Stenchikov et al., 1998]. Elevated aerosol results in an increase in methane above 50mb which persists through the entire simulation (figure 17(b)). This increase is due to enhanced tropical upwelling, as discussed above. Air with high methane mixing ratios is lofted into the middle and upper stratosphere, where methane has a photochemical lifetime on the order of a year. Methane enhancements of over 0.03 ppmv (5-15%) are still present throughout the upper stratosphere at the end of 1994. Nedoluha et al. [1998] show negative trends in upper stratospheric CH<sub>4</sub> as observed by HALOE during 1991-1997. They argue that the most likely cause of these trends is a decrease in lower stratospheric tropical upwelling, such as occurred during the decay of the Pinatubo aerosol cloud, however they note that Pinatubo effects on CH<sub>4</sub> are thought to be small and confined to altitudes below 25 km (30 mb). The present results show significant globally-averaged CH<sub>4</sub> increases of up to 0.06 ppmv (15%) throughout the upper stratosphere. Although our modeled peak anomalies and the decay rates which follow (approximately 0.01 ppmv/year) are only about 25% of the values deduced by Nedoluha et al. [1998], they demonstrate that Pinatubo-induced circulation changes are important in the upper stratosphere. The combined aerosol response in Ox (figure 17(c)) is a significant decrease below about 12 mb, including a peak decrease of over 0.20 ppmv (5%) at 30 mb from late 1991 to late 1992. Significant decreases of about 0.05 ppmv (2%) are still experienced during 1994. No consistent significant response is indicated at 10 mb and above. The lack of an upper stratospheric response is due to the shorter Ox photochemical lifetime there.

The heating-only temperature (figure 17(d)) and methane (figure 17(e)) anomalies are similar to those derived from the combined aerosol perturbation, confirming that the temperature and CH<sub>4</sub> responses are largely due to aerosol radiative heating. Relative to the combined anomaly, the heating-only temperature anomaly is about 0.5 K larger at the altitude of the peak warming (50 mb) but about 0.5 K smaller near 10 mb. Upper stratospheric differences between the CH<sub>4</sub> anomalies illustrate a circulation response consistent with the middle-stratospheric temperature difference: lofting of CH<sub>4</sub> in the upper stratosphere is modulated by heating differences in the mid-stratosphere. A significant negative Ox anomaly (figure 17(f)) exists between 60 and 10 mb, with a peak decrease of up to 0.15 ppmv (3%) at 20 mb in early 1992. This anomaly is due to the enhanced diabatic upwelling of lower O<sub>3</sub> values below the O<sub>3</sub> peak near 10 mb (e.g., figure 14(c)). The negative anomaly has largely dissipated by early 1993.

Figure 18 shows the SAD-only temperature anomaly as a function of the corresponding odd

oxygen anomaly. Shown are data from the entire simulation period where both the temperature and Ox anomalies are significant (larger than interannual 2-sigma standard deviation). Odd oxygen decreases below 25 mb and increases above 25 mb, accounting for the differences between the combined (figure 17(c)) and heating-only (figure 17(f)) Ox anomalies. These changes in O3 result from changes in the in-situ photochemical destruction caused by the chemical repartitioning which occurs in the presence of elevated sulfate aerosol, as discussed in a subsequent section. The temperature response is of the same sign as the O3 response and has a magnitude of about 0.5 K per 0.1 ppmv of Ox. This correlation between temperature and ozone reflects the direct coupling between photochemical changes associated with elevated aerosols and resulting dynamical responses due to perturbed radiative heating rates. This feedback of O3 on temperature explains the differences in the temperature anomalies shown in figures 17(a) and (d). Such feedbacks can only be captured with coupled chemical/dynamical models.

The combined response of nitrogen species to aerosol heating and SAD is shown in figure 19. The response in NOy (figure 19(a)) is a decrease in the mid-stratosphere of up to 0.4 ppbv (4%) and an increase in the upper stratosphere of up to 0.6 ppbv (6%). The NOy response reaches a maximum in mid- to late- 1992. The mid-stratospheric decline persists through early 1993, coincident with the period of the largest radiative heating anomaly (figure 17(a)). The upper-stratospheric increase is still pronounced at the end of the simulation, descends and decays slowly throughout the simulation period, and has a seasonal component (maximizing in October/November). As discussed above, the NOy response is explained by circulation changes associated with increased tropical upwelling. The NOx response (figure 19(b)) mirrors that of NOy in the upper stratosphere because NOx species are the dominant components of NOy in this region. The negative middle-stratospheric anomalies of NOx (figure 19(b)) and its nighttime reservoir N2O5 (figure 19(d)), and the corresponding positive HNO3 anomaly (figure 19(c)), demonstrate the repartitioning which occurs within the NOy family due to enhanced heterogeneous hydrolysis of N2O5 with elevated aerosol. This chemical response maximizes at 20 mb, and the largest effect occurs in late 1991 and early 1992, including HNO3 increases of up to 1.4 ppbv (30%), NOx decreases of 0.8 ppbv (40%), and N2O5 decreases of 0.4 ppbv (80%). The response decays but remains significant throughout the remainder of the simulations, and HNO3 enhancements in excess of 0.4 ppbv (10%) remain at the end of 1994.

The response of chlorine species to elevated aerosol is more clearly illustrated by first separately considering the heating and heterogeneous chemical (SAD) responses. Figure 20 shows the response of chlorine species to aerosol heating only. Significant decreases in Cly (figure 20(a)) are apparent above 40 mb, while significant increases result below 40 mb. These changes in Cly are circulation-induced; in this global anomaly, the negative response is primarily a tropical signature of enhanced upwelling, and the positive response in the lower stratosphere is primarily an extratropical signature of enhanced downwelling. Largest Cly increases exceed 0.02 ppbv (4%) near 70 mb through most of 1992, and a significant increase of 0.01 ppbv (2%) persists through 1993. These lower stratospheric Cly increases are largely in the form of HCl (figure 20(c)). Largest Cly decreases, of up to 0.04 ppbv (2%), initially occur between 10 and 20 mb in late 1991. The peak decrease slowly diminishes and ascends with time, and significant decreases of up to 0.02 ppbv (1%) still exist near 10 mb in mid-1994. The Cly decrease is largely reflected in decreased ClONO2 in the mid-stratosphere (figure 20(d)), in addition to decreased Clx above 10 mb (figure 20(b)). The region over which ClONO2 is decreased coincides with an aerosol heating-induced reduction in NOx of approximately 0.10 ppbv (not shown), and the decrease in NOx shifts inorganic chlorine partitioning from ClONO2 to ClO (Clx) [Stimpfle et al., 1994]. The upper strato-

spheric increase in HCl (figure 20(c)) and corresponding decrease in Clx (figure 20(b)), reflecting a mid-latitude shift in chlorine partitioning in response to elevated CH<sub>4</sub> levels (e.g., figure 17(b)), are significant through 1993.

The response of chlorine partitioning to elevated SAD only is shown in figure 21. The increase in Clx (figure 21(b)) in the presence of elevated aerosol is almost entirely at the expense of HCl (figure 21(c)). Little consistent change is observed in either Cly (figure 21(a)) or ClONO<sub>2</sub> (figure 21(d)). Although a direct effect of sulfate aerosol on chlorine partitioning is the conversion of ClONO<sub>2</sub> to HOCl (i.e., Clx; reaction 89, Table A3), this reaction is efficient only at cold temperatures and is unlikely to yield a large global response. Instead, this repartitioning is due to the repartitioning within the NO<sub>y</sub> family. Photolysis of the elevated HNO<sub>3</sub> enhances OH radical production (e.g., Rosenfield et al. [1997]), which increases Clx at the expense of HCl. Thus the altitude distribution and temporal evolution of the Clx anomaly closely follow those of the HNO<sub>3</sub> anomaly (figure 19(c)). Largest Clx enhancements, of over 0.08 ppbv (60%), occur at 20 mb from late 1991 through mid-1992, and the anomaly slowly decays thereafter.

Figure 22 shows the combined response of chlorine species to aerosol heating and SAD. The Cly response (figure 22(a)) is primarily attributable to the circulation changes induced by the aerosol heating. Clx (figure 22(b)) is generally elevated in the lower stratosphere (below 10 mb) through the entire simulation period, although the anomaly episodically diminishes to insignificant levels during periods corresponding to NH spring in 1993 and 1994. This Clx enhancement is a chemical response, while the Clx reduction in the upper stratosphere is a dynamical response. Largest decreases of HCl (figure 22(c)) and ClONO<sub>2</sub> (figure 22(d)) are of similar magnitude to each other, in excess of 0.06 ppbv (5%), and coincide in time and space with the Clx enhancement, however the HCl decrease has been shown to be primarily a chemical response and the ClONO<sub>2</sub> decrease to be a dynamical response. The increase in Cly in the lower stratosphere, of over 0.03 ppbv (5%) 1<sup>1</sup>/<sub>2</sub> years after the eruption, is largely reflected in increased Clx and HCl.

### Comparison with UARS measurements

Model results from baseline (composite, BLC) and elevated-aerosol (AH and AHS) simulations are compared with observations made from instruments onboard the UARS satellite in figure 23. Shown are zonally-averaged distributions of temperature, CH<sub>4</sub>, O<sub>3</sub>, HNO<sub>3</sub>, HCl, and ClONO<sub>2</sub> at 30 mb during May 1992, the approximate altitude and time of the peak modeled ozone response to elevated aerosol (figure 17). Also shown are instrument uncertainty estimates (solid thin lines) and the model 1-sigma and 2-sigma yearly standard deviation estimates (dark and light shading, respectively). Longer-lived species experience tropical stratospheric variability apparently related to the QBO, which Luo et al. [1997] have characterized for species observed by the HALOE instrument. At 30 mb during May 1992, they estimate tropical (averaged over 10°S to 10°N) QBO anomalies of about 0.1 ppmv for O<sub>3</sub>, 0.04 ppmv for CH<sub>4</sub>, and -0.10 ppbv for HCl.

Temperature is compared with data from the HALOE archive in figure 23(a). The temperature distributions from the two elevated-aerosol simulations are similar to each other, and aerosol heating yields a net warming at all latitudes. The warming of about 4 K throughout the tropics and mid-latitudes yields temperatures that compare well with HALOE data; the model is cool by about 1 K in the tropics, comparable to the model variability, and by up to 3 K in mid-latitudes, slightly greater than the model variability. Pierce et al. [2000] show that the IMPACT model has a cold bias of about 2.5 K at 30 mb, similar to these estimates. The modeled high-latitude response, poleward of about 60°, is within the 2-sigma variability and therefore not significant.

The modeled CH<sub>4</sub> response to elevated aerosol does not differ significantly from the baseline

at this time and altitude (figure 23(b)). The simulations generally compare well with HALOE CH<sub>4</sub> observations, including excellent agreement in the NH and a model high bias of about 0.1 ppmv in SH mid-latitudes, at the upper range of HALOE uncertainty (as similarly noted in the discussion of figure 1). This agreement indicates that the IMPACT model is adequately representing the atmospheric residual circulation. Recall (figure 17(b)) that the peak CH<sub>4</sub> response to elevated aerosol occurs at higher altitudes, above 10 mb. Because the majority of the temperature and CH<sub>4</sub> response is due to the aerosol heating, the results from the two elevated-aerosol simulations are similar for these quantities.

Model O<sub>3</sub> is compared with HALOE observations in figure 23(c). Throughout tropical latitudes, aerosol heating significantly decreases the O<sub>3</sub> mixing ratio and elevated SAD yields further decreases. These low-latitude decreases yield good qualitative comparison with the HALOE observations. In particular, O<sub>3</sub> from the AHS simulation is within the estimated HALOE uncertainty, although consistently higher than HALOE by 0.5 ppmv (about 12%) at all latitudes. This model high bias is consistent with figure 2, which shows a bias of 10-20% at 30 mb with low aerosol loading. No significant high-latitude response occurs at this time and altitude.

Modeled HNO<sub>3</sub> is compared with CLAES observations in figure 23(d). Results from the AHS simulation are in excellent agreement with the observations, particularly in NH mid-latitudes; the significant mid-latitude increases of over 1 ppbv in the NH and 0.5 ppbv in the SH result from heterogeneous chemical processing with elevated SAD. Relative to the baseline, aerosol heating alone (AH) yields a significant HNO<sub>3</sub> decrease in equatorial and northern tropical latitudes. This decrease is a response to the enhanced tropical upwelling, as the HNO<sub>3</sub> mixing ratio profile peaks above this altitude at about 20 mb (figure 15(b)). Elevated SAD then yields an increase in the tropical HNO<sub>3</sub> mixing ratio (AHS relative to AH), resulting in excellent agreement with CLAES observations throughout the tropics. The AHS simulation also yields increases in SH high latitudes which are significant with respect to the large interannual variability there, however CLAES did not view these latitudes during this month.

Chlorine partitioning is examined by comparing model results with HALOE HCl (figure 23(e)) and CLAES ClONO<sub>2</sub> (figure 23(f)). There is very little effect of aerosol heating on the HCl distribution at this altitude. Elevated SAD decreases HCl mixing ratios by a small but significant 0.05 ppbv from equatorial to NH mid-latitudes, and by over 0.10 ppbv in SH mid-latitudes; large decreases in high latitudes (about 0.10 ppbv) are not significant with respect to model variability. Although these decreases improve the agreement with HALOE observations, the AHS simulation predicts HCl mixing ratios that are more than 0.10 ppbv higher than HALOE in equatorial latitudes, higher than the estimated HALOE uncertainty, and in the NH extra-tropics, within the estimated HALOE uncertainty. Luo et al. [1997] show that QBO effects decrease the equatorial HCl mixing ratio by about 0.10 ppbv at this time and altitude; compensating for this effect would improve the agreement of the AHS result with HALOE to about the estimated uncertainty limit. These results are consistent with the biases shown in figure 3 in tropical latitudes, but are not consistent in mid-latitudes because different seasons are shown and the mid-latitude HCl comparison exhibits seasonal changes at 30 mb (figures 3(c) and (f)). Elevated aerosol significantly decreases ClONO<sub>2</sub> by less than 0.1 ppbv in tropical latitudes, resulting in very good agreement with the CLAES observations. In mid-latitudes, model results show little effect of elevated aerosol on ClONO<sub>2</sub> and are almost 0.2 ppbv lower than CLAES observations, comparable to the estimated CLAES uncertainty estimates. The apparent model overestimate of HCl and corresponding underestimate of ClONO<sub>2</sub> in NH mid-latitudes indicates that some inaccuracy in the model chlorine partitioning may exist, likely due to the neglect of heterogeneous reactions of HCl in liquid sulfate

aerosol in the model version used for these simulations (e.g., Michelsen et al., [1999]). Although these reactions are most efficient at the cold temperatures typical of the lower tropical stratosphere and high-latitude winter stratosphere, preliminary studies have indicated that inclusion of these reactions in the IMPACT model may decrease HCl and increase ClONO<sub>2</sub> mixing ratios throughout the lower and middle stratosphere - particularly in the presence of elevated sulfate aerosol. Tie and Brasseur [1996] show that with high aerosol loading, heterogeneous bromine chemistry can also significantly enhance ClONO<sub>2</sub> and ClO at the expense of HCl in the lower stratosphere.

### Photochemical Loss of O<sub>3</sub>

As shown above, stratospheric abundances of reactive nitrogen are reduced in the presence of sulfate aerosol while those of reactive chlorine and hydrogen are increased. These changes alter the balance of processes which control photochemical destruction of O<sub>3</sub> in the lower stratosphere, and may lead to either increases or decreases in the O<sub>3</sub> abundance depending on the altitude [Solomon et al., 1996; Zhao et al., 1997; Rosenfield et al., 1997]. Figure 24 shows the effect of elevated aerosol on in-situ photochemical O<sub>3</sub> destruction near the time and altitude of the largest aerosol-induced change in O<sub>3</sub>: May of Year 3 (1992) at 30 mb. The catalytic O<sub>x</sub> loss cycles, and the apportioning of O<sub>x</sub> loss between hydrogen, nitrogen, and halogen radicals, follow standard stratospheric definitions [e.g., Wennberg et al., 1994; Crutzen and Shmailzl, 1983]. Figure 24(a) shows the total photochemical destruction of O<sub>3</sub> for both the BL1 and AHS simulations. To first order the loss increases with increasing solar insolation, thus in May the largest loss is in the Northern Hemisphere. Elevated aerosol increases the photochemical loss within the extratropics of both hemispheres by up to 0.1 ppmv/month. The other panels of figure 24 show that in the baseline simulation at this altitude, the NO<sub>x</sub>, HO<sub>x</sub>, and halogen catalytic loss cycles contribute approximately equally to the total O<sub>x</sub> destruction. The NO<sub>x</sub> loss fraction is largest in northern midlatitudes, HO<sub>x</sub> fraction is largest in the tropics, and halogen fraction is largest in high southern latitudes. The net effect of the aerosol-induced repartitioning of radical species on O<sub>3</sub> photochemical destruction is a reduction in the nitrogen-catalyzed fraction by about 50% in the SH and 25-33% in the NH (figure 24(b)), an enhancement in the halogen-catalyzed fraction by 25-33% (figure 24(c)), and an increase in the HO<sub>x</sub>-catalyzed fraction of up to 10% in the SH and 25% in the NH (figure 24(d)).

The O<sub>x</sub> loss at the higher altitude of 20 mb is shown in figure 25. The relative importance of the NO<sub>x</sub>-catalyzed loss increases with altitude through the lower stratosphere, as can be seen by comparing results from the BL1 simulation at 20 mb (figure 25(b)) to those at 30 mb (figure 24(b)). The loss fractions due to both halogen and hydrogen catalysis show corresponding decreases with increasing altitude. The aerosol-induced changes in the loss fractions are similar to those at 30 mb: increased halogen and HO<sub>x</sub> loss and decreased NO<sub>x</sub> loss. However, as shown in figure 25(a), the total photochemical O<sub>x</sub> loss at 20 mb is decreased in the tropics with elevated aerosol. At this altitude the decrease in NO<sub>x</sub>-catalyzed loss with elevated aerosol is larger than the increased loss from the other catalytic cycles. These changes are in good qualitative agreement with model results shown by Tie and Brasseur [1995] for March at 65°N. They show decreased NO<sub>x</sub> destruction of O<sub>3</sub> maximizing in the middle stratosphere, increased Cl<sub>x</sub> destruction maximizing in the lower stratosphere, and slightly increased HO<sub>x</sub> destruction throughout the middle stratosphere, yielding a net increase in O<sub>3</sub> destruction below 22 km and decrease in destruction above 22 km.

The increase in the relative importance of the NO<sub>x</sub>-catalyzed loss with altitude, together with

the shift in halogen, hydrogen, and nitrogen radicals mediated by heterogeneous chemistry, explain the globally-averaged response of lower-stratospheric O<sub>3</sub> to elevated SAD shown in figure 18. Below about 25 mb the increases in photochemical Ox destruction due to the enhanced halogen and HOx catalytic cycles outweigh the decrease in NOx-catalyzed destruction, yielding a net increase in photochemical Ox loss and decrease in O<sub>3</sub>. Above 25 mb the decrease in NOx-catalyzed O<sub>3</sub> loss begins to outweigh the increases in the other catalytic cycles, yielding a net decrease in Ox loss and increase in O<sub>3</sub>.

The difference in 20 mb photochemical Ox loss at northern high latitudes (figure 25(a)) is largely due to interannual variability. The elevated-aerosol simulation experiences a later final warming of the winter stratospheric vortex than does the baseline simulation during this year (e.g., figure 9). During the warming, air with high Ox mixing ratios is transported poleward, where it undergoes a period of relatively rapid photochemical loss (in the mid- to upper-stratosphere) until Ox levels approach typical ambient concentrations. During May of Year 3 the baseline simulation has already experienced this period of rapid loss, while the elevated-aerosol simulation is still experiencing it.

## Conclusion

We have analyzed the global response of the atmosphere to a large volcanic eruption using multi-year simulations conducted with a GCM with coupled comprehensive chemistry. A new approach is the use of a 3-D time-dependent aerosol surface area density distribution which is reconstructed from observationally-based regressions. This study is the first application of such a model to investigate the combined chemical, radiative, and dynamical response to volcanically-elevated stratospheric sulfate aerosol over a multi-year period.

Both radiative and chemical effects are shown to contribute to the changes in atmospheric structure and composition which occur following an eruption of the magnitude of Pinatubo. Significant warming of the tropical stratosphere results from aerosol-induced heating. Important stratospheric chemical/dynamical feedback effects are shown, as ozone reductions modulate this heating by about 0.5 K per 0.1 ppmv of ozone, or up to 10% in the lower stratosphere and 25% in the middle stratosphere. Differing causes of changes in composition are illustrated in the partitioning of chlorine species in the mid-stratosphere, where the decrease of HCl has been shown to be primarily a chemical response, while that of ClONO<sub>2</sub> is primarily a dynamical response.

In agreement with previous studies, the direct radiative response to the aerosol perturbation has largely decayed within 2 years of the eruption. However, signatures of the altered circulation are still apparent in the upper stratosphere at the end of these simulations (3<sup>1</sup>/<sub>2</sub> years following the eruption), as long-lived species such as CH<sub>4</sub> are still recovering from anomalous concentrations induced by enhanced tropical upwelling in the months just after the eruption. Chemical changes initiated by heterogeneous reactions in the presence of increased sulfate aerosol are largely confined to the lower and middle stratosphere, but still persist at the end of these simulations because sulfate aerosol is still elevated over pre-volcanic “clean” aerosol levels by about a factor of 2.

Relative to TOMS observations, the model appears to overestimate the O<sub>3</sub> reduction during the first year following the eruption in the tropics and in a global average. Thereafter the modeled and observed globally-averaged reductions are very similar, peaking at 3<sup>1</sup>/<sub>2</sub>-4% in late 1992 and decaying to within the interannual variability of 1% by mid-1994. Based on this initial overestimate of O<sub>3</sub> reduction, and on our maximum stratospheric warming anomaly of about 5 K in comparison to previous estimates of 4 K, it appears that our modeled radiative response to the elevated

aerosol is overestimated by about 20% in the lower stratosphere. Also, the modeled photochemical depletion of O<sub>3</sub> with elevated aerosol may be overestimated by up to 30% in mid-latitudes on the basis of recently revised rate recommendations for key nitrogen radical partitioning reactions. Below 20 mb enhanced tropical upwelling and increased photochemical loss contribute approximately equally to decreasing O<sub>3</sub>, while above 20 mb reduced photochemical O<sub>3</sub> destruction compensates the decrease in O<sub>3</sub> due to enhanced upwelling. Some studies have shown small aerosol-induced O<sub>3</sub> increases between 20 and 10 mb, suggesting that the O<sub>3</sub> increase due to decreased destruction exceeds the transport-induced O<sub>3</sub> reduction in this altitude range. A slight overestimate of our modeled radiative response would be consistent with such behavior.

Modeled mid-latitude column O<sub>3</sub> reductions are similar to observed reductions over most of the simulation period. In the NH good agreement includes significant decreases of 3-4% from mid-1992 to mid-1994, however the observed large reduction of up to 10% in winter/spring 1992-93 is not simulated by the model. Modeled SH mid-latitude reductions of over 4% beginning in late 1992 exceed observed reductions, but modeled and observed reductions of near 3% compare well in late 1993 and early 1994. It is likely that these particular discrepancies in mid-latitudes result from interannual dynamical variability, which can not be addressed in these single realizations of time-dependent elevated aerosol simulations. In particular, the observed large NH reduction in winter/spring 1992-93 has been largely attributed to dynamical variability rather than a direct response to Pinatubo.

This sensitivity in O<sub>3</sub> response illustrates the challenge of confidently predicting future chemical/climate interactions. The modeled atmospheric response to a large transient perturbation can be clear and unambiguous in regions where the variability is either low or can be reasonably characterized, as in tropical QBO cycles. However, even large perturbations must be considered in the context of other sources of variability when characterizing responses in regions of the atmosphere naturally subject to large variability, such as the middle and high latitude stratosphere in winter and spring. Improved confidence in the prediction of possible responses to time-dependent forcings in such regions may require, at the minimum, an ensemble of simulations in which the extrema of other sources of variability are considered in the model.

Models such as the IMPACT model are well-suited for establishing causal relationships important in determining future likely atmospheric states. With continued increases in computing speed, such interactive models will evolve into climate models which allow a full range of physical interactions, giving increased confidence in global change predictions. The results of these simulations, including our abilities to extract trends that are significant with respect to internal variability, diagnose both dynamical and photochemical forcings for the observed changes, and identify dynamical-chemical feedbacks, demonstrate that we can realistically investigate chemistry/climate coupling issues over decadal time scales.

## Appendix A: Description of the IMPACT model

The LaRC IMPACT model is a global, three-dimensional coupled dynamics, radiation and chemistry model of the troposphere and middle atmosphere [Grose et al., 1984; Grose et al., 1987; Blackshear et al., 1987; Pierce et al., 1993; Fairlie et al., 1998; Pierce et al., 2000]. The dynamics component is a general circulation model based on the primitive equations, and the chemistry component is composed of constituent mass continuity equations for 24 individual constituents and chemical families. The model is radiatively coupled through the computed ozone distribution, and includes full tropospheric physics with cloud-radiative feedbacks. The terrain-following sigma coordinate is used throughout. A spectral representation with triangular truncation at 32 waves (T32) is employed in the horizontal. Nonlinear terms are evaluated using the transform method on a latitude-longitude grid of approximately  $2.8^\circ \times 2.8^\circ$ . The vertical domain extends from the ground to 90 km using 34 levels in the dynamics component, and from the ground to 60 km using 24 levels in the chemistry component. Vertical resolution is approximately 100 hPa in the troposphere and 3 km in the stratosphere. Vertical transport is conducted with a third-order upwind-biased flux-limited finite difference scheme. Time integration is accomplished using a centered second-order (leapfrog) method with a time step of 15 minutes, and a 1-2-1 centered time filter is applied at a frequency of every six time steps to control odd-even time splitting. Complete details and characteristics of the dynamics component are presented in Pierce et al. [2000]. Recent developments in the chemistry component are detailed here.

The chemical component of the IMPACT model has evolved from the chemistry-transport model described in detail in Eckman et al. [1995]. Recent developments include the explicit transport of ten additional constituents, an improved treatment of the partitioning of active chlorine species, a new photochemical tendency calculation which is more accurate for species with “short” photochemical lifetimes, and an improved parameterization of polar stratospheric cloud (PSC) formation and associated heterogeneous chemical processing.

The present version of the chemistry model considers 53 chemical species (Table A1) using 41 photolytic reactions (Table A2) and 105 chemical reactions (Table A3). Twenty-four chemical families or individual species are explicitly transported, and the concentrations of the remaining species are obtained by partitioning of the chemical families using standard photochemical equilibrium techniques. The 24 transported constituents are odd oxygen ( $O_x = O + O(^1D) + O_3$ ), total odd nitrogen ( $NO_y = N + NO + NO_3 + 2N_2O_5 + HNO_3 + HO_2NO_2 + ClONO_2 + BrONO_2$ ), total inorganic chlorine ( $Cl_y = Cl + ClO + HOCl + HCl + ClONO_2 + 2Cl_2 + 2Cl_2O_2 + ClO_2 + OClO + BrCl$ ),  $HNO_3$ ,  $N_2O_5$ ,  $H_2O_2$ ,  $HCl$ ,  $ClONO_2$ ,  $N_2O$ ,  $CFCl_3$ ,  $CF_2Cl_2$ ,  $CCl_4$ ,  $CH_3Cl$ ,  $CH_3CCl_3$ , total inorganic bromine ( $Br_y = Br + BrO + HOBr + HBr + BrONO_2 + BrCl$ ),  $CH_3Br$ ,  $CF_3Br$ ,  $CF_2ClBr$ ,  $HF$ ,  $CFCIO$ ,  $CF_2O$ ,  $CH_4$ ,  $HO_2NO_2$ , and  $HOCl$ . The last ten members of this list have been added since the study of Eckman et al. [1995]. Inorganic bromine is relevant in several catalytic odd-oxygen destruction cycles, thus it and its source halocarbon gases are now transported.  $HF$  is the predominant fluorine-containing reservoir species in the stratosphere;  $CFCIO$  and  $CF_2O$ , also fluorine reservoir species, are intermediates between the halocarbon source gases and  $HF$  [Kaye et al., 1991].  $CH_4$  concentration had previously been specified in the model as a seasonal zonal mean climatology. Both  $HO_2NO_2$  and  $HOCl$  had previously been treated in photochemical equilibrium in the model, however with a 15-minute time step it is possible to explicitly transport both species throughout much of the troposphere and stratosphere.  $HO_2NO_2$  is an important nitrogen reservoir in the upper troposphere and lower stratosphere - the region of the atmosphere receiving increasing emphasis in our modeling efforts.  $HOCl$  can be a very important species in the hetero-



geneous conversion of chlorine to active forms because it is both a product of (i.e., reaction 89 in Table A3) and a reactant in (i.e., reaction 43 in Table A3) potential heterogeneous reactions. Transport of HOCl allows a more realistic partitioning of active chlorine during nighttime. This realistic partitioning is critical for proper representation of the above heterogeneous reactions during polar night, and also results in improved prediction of ClONO<sub>2</sub> concentrations at latitudes not experiencing continuous sunlight.

Odd hydrogen (HO<sub>x</sub>) is assumed to be in photochemical equilibrium throughout the model domain. A simplified methane oxidation scheme is included through the representation of CH<sub>x</sub> chemistry. The present version of the model includes gas-phase bromine chemistry but does not consider heterogeneous bromine reactions. Three of the species considered in the model (H<sub>2</sub>O, H<sub>2</sub>, and CO) are specified as a function of latitude, altitude and time, as detailed in Eckman et al. [1995]. At present this water vapor climatology, rather than the explicitly-transported water vapor resulting from tropospheric moist processes, is used in photochemical calculations.

Kinetic rates are taken from the compilation of DeMore et al. [1997], and bimolecular and termolecular rate constants are calculated at each time step. As noted in Eckman et al. [1995], the reaction of ClO + OH with a branching ratio of 5% to the HCl + O<sub>2</sub> channel is included; recently published results (e.g., Lipson et al. [1997], Khosravi et al. [1998]) continue to support this inclusion, with a recommended branching ratio of 6±2%. The concentrations of transported halocarbons, methane, and nitrous oxide at the ground are specified with constant mixing ratios using tropospheric abundance recommendations appropriate for 1990 [WMO, 1991].

Photodissociation rates are obtained using a table lookup method (S. R. Kawa, private communication, 1996) to reduce computational time. Tabulated radiative flux functions are stored as a function of solar zenith angle, overhead ozone column and wavelength. The radiative flux in each wavelength interval is obtained through bilinear interpolation with respect to overhead column and zenith angle. Photolysis rates are then calculated as the sums (over all wavelength intervals) of the products of the absorption cross sections and the radiative fluxes. Absorption cross sections are obtained from Demore et al. [1997]. At present the radiative flux tabulations assume a uniform surface albedo of 30%. Multiple scattering is parameterized following the methodology of Meier et al. [1982]. Photodissociation rates for nitric oxide and methane are not obtained from the table lookup method. Photodissociation of NO is parameterized according to the recommendation of Nicolet [1979], and CH<sub>4</sub> photodissociation is treated according to the recommendation of Nicolet [1985] at the solar Lyman-alpha band. The ultraviolet solar irradiances are derived from the recommendations of Frederick et al. [1986] based on satellite and rocket measurements.

The model representation of polar stratospheric cloud (PSC) formation and associated heterogeneous chemical processing has recently undergone substantial improvement. At present we consider that 5 reactions (reactions 43, 68, 73, 76 and 80 in Table A3) may occur on PSC particles. A heterogeneous chemistry model adapted from the University of Cambridge TOMCAT model [Chipperfield, 1999] is used to determine whether PSCs exist at the local atmospheric conditions and constituent concentrations, and if so, the rate constants for the 5 heterogeneous reactions. The fractions of total HNO<sub>3</sub> and H<sub>2</sub>O that exist in condensed phase are instantaneously diagnosed from local saturation vapor pressure relations [Hanson and Mauersberger, 1988]. The local thermodynamic conditions and the amounts of these condensed phase species determine particle sizes and thus reaction rate constants. The use of such a PSC parameterization requires that the evolution of winter polar lower stratospheric conditions in our model compare well with climatology; such verification is presented in Pierce et al. [2000]. Denitrification, a local removal of odd nitrogen from the system, is parameterized as sedimentation of HNO<sub>3</sub> in PSC particles.

The presence of condensed phase  $\text{HNO}_3$  is taken as an indicator of type I PSCs, with an associated weak removal time constant of 75 days; the presence of condensed phase  $\text{H}_2\text{O}$  is taken as an indicator of type II PSCs, with a much faster removal time constant of 2 days. The sedimentation parameterization preserves the column mass of  $\text{HNO}_3$  (and of odd nitrogen) by allowing evaporation into lower model levels as governed by local saturation vapor pressure. Dehydration through this sedimentation process is not treated explicitly by the model because climatological water is used for chemical calculations. However, when  $\text{H}_2\text{O}$  ice is present, the local vapor-phase concentration is reduced accordingly.

Heterogeneous chemical processing on stratospheric liquid sulfate aerosols is simulated by considering the hydrolysis reactions of  $\text{N}_2\text{O}_5$  and  $\text{ClONO}_2$  (reactions 88 and 89 in Table A3). These reactions are represented as first order processes with rate coefficients dependent on the reaction probability, aerosol surface area density, and mean molecular speed [e.g., Rodriguez et al., 1989]. The reaction probabilities in these expressions follow the recommendations of Hanson et al. [1994]. For non-volcanic conditions the aerosol surface area density follows recommendations for a background scenario [WMO, 1991].

An improved method for computing the photochemical tendencies of individual species has been implemented. This method is based on the exact solution of the ordinary differential equation governing the time rate of change of constituent concentration with constant production and loss, and is referred to as pseudo-exact. A simple Euler-forward method was previously used to calculate all photochemical tendencies, and is still used for long-lived constituents (e.g., halocarbon source gases and the families Ox, NOy, Cly, Bry). The pseudo-exact method is significantly more accurate than the Euler-forward method when the chemical loss lifetime is short, as is the case for several of the individually-transported species over some portion of the model domain, and the two methods yield nearly identical results when the chemical loss lifetime is long.

Newly transported long-lived species ( $\text{Br}_y$ ,  $\text{CH}_3\text{Br}$ ,  $\text{CF}_3\text{Br}$ ,  $\text{CF}_2\text{ClBr}$ , HF,  $\text{CFCIO}$ ,  $\text{CF}_2\text{O}$ ,  $\text{CH}_4$ ) were initialized using results from a lower resolution CTM simulation [Eckman et al., 1995]. These new species were initialized in the CTM with zonal mean climatologies. The CTM was then integrated over multiple years, using annually-repeating winds and temperatures, until annually-repeating constituent distributions resulted - approximately 10 model years. Relationships were then developed between the new species and  $\text{N}_2\text{O}$ , a long-lived tracer which has been transported in both models for several model years. Finally, these new species were mapped to the initial conditions of the present coupled simulation using  $\text{N}_2\text{O}$  as an independent variable. This technique ensures that the new long-lived tracers are in approximate balance with the model flow-field. The newly transported “fast” species ( $\text{HO}_2\text{NO}_2$ ,  $\text{HOCl}$ ) were simply initialized to zero and allowed to evolve. These species reached an approximate diurnal steady state throughout most of the model domain within 7 days, and throughout the entire domain within 3 weeks.

Present simulations are conducted in a coupled interactive mode. At each time step, the complete wind and temperature fields are obtained from the dynamics component of the IMPACT model. These thermodynamic conditions are used in the calculation of photochemical tendencies, as discussed above. Time integration of the constituent continuity equations is then performed using these photochemical and transport tendencies. The resulting ozone distribution is used in the determination of stratospheric radiative heating rates by the dynamics component of the IMPACT model [Pierce et al., 2000].

## **Appendix B: Removal of Non-Volcanic Variations from TOMS Data**

Much of the variability in column ozone on interannual timescales is either attributable to or correlated with natural forcings having specific timescales (e.g., WMO [1999], Randel and Cobb [1994]). Such forcings include the quasi-biennial oscillation (QBO), El-Nino southern oscillation (ENSO), and solar cycle or some other quasi-decadal variation for which solar cycle may serve as proxy (e.g., Baldwin and Dunkerton [1998], Salby et al. [1997], Randel and Cobb [1994]). To better evaluate and compare the modeled and observed responses to volcanically-enhanced aerosol, periodic variations resulting from external forcings not represented in the model are removed from the TOMS data shown herein. The approach taken is to use a simple multiple linear regression model to fit the TOMS data record, exclusive of the post-Pinatubo period, then subtract the terms for these specific natural forcings from the entire data record.

The regressions were performed using the longest available data record to improve confidence that longer-period variations are properly represented. Version 7 TOMS monthly zonal mean data in 5-degree latitude bins were obtained from the NASA/GSFC TOMS Ozone Processing Team for the NIMBUS-7, METEOR-3, and Earth Probe instruments for the period 1978-1999. Data from the NIMBUS-7 and METEOR-3 instruments were averaged during months when both were operational (between February 1992 and April 1993). The multiple linear regression model was used to fit the TOMS data within each latitude bin between 65°S and 65°N from November 1978 through December 1999, excluding the post-Pinatubo period June 1991 through December 1994. Because no TOMS observations are available from December 1994 to July 1996, the fits are therefore constrained during November 1978 through May 1991 and August 1996 through December 1999. A separate regression was performed for each calendar month to account for the seasonality of these variations [e.g., as in Bojkov et al., 1990]. The regression model included linear, QBO, ENSO, and solar terms. Reference series used to represent the forcings are a weighted average over 70-10 mb of monthly-mean tropical winds [Randel et al., 1995] for the QBO, normalized Southern Oscillation Index for the ENSO, and solar F10.7-cm flux for the solar cycle. Each reference series is smoothed with a 1-2-1 filter, adjusted to have a time-mean of zero, and normalized to a maximum magnitude of 1. A lag of up to 11 months (3 months in tropical latitudes) with respect to each reference series was considered in the regression to allow for seasonally-delayed responses to remote forcing. The final regression for each latitude and month includes only terms which reduce the regression error at a significance level of 90%. During the period 1978-1999, the combined adjustments to TOMS O<sub>3</sub> from removing the QBO, ENSO, and solar signatures range between  $\pm 8$  Dobson Units in tropical latitudes and  $\pm 12$  Dobson Units in extratropical latitudes.

## References

- Angell, James K., Estimated impact of Agung, El Chichon and Pinatubo volcanic eruptions on global and regional total ozone after adjustment for the QBO, *Geophys. Res. Lett.*, **24**, 647-650, 1997(a).
- Angell, J. K., Stratospheric warming due to Agung, El Chichon, and Pinatubo taking into account the quasi-biennial oscillation, *J. Geophys. Res.*, **102**, 9479-9485, 1997(b).
- Austin, John, Jeffrey Knight, and Neal Butchart, Three-dimensional chemical model simulations of the ozone layer: 1979-2015, *Q. J. R. Meteorol. Soc.*, **126**, 1533-1556, 2000.
- Baldwin, Mark P. and Timothy J. Dunkerton, Biennial, quasi-biennial, and decadal oscillations of potential vorticity in the northern stratosphere, *J. Geophys. Res.*, **103**, 3919-3928, 1998.
- Blackshear, W. T., W. L. Grose, and R. E. Turner, Simulated sudden stratospheric warming; synoptic evolution, *Q. J. R. Meteorol. Soc.*, **113**, 815-846, 1987.
- Bojkov, R. D., L. Bishop, W. J. Hill, G. C. Reinsel, and G. C. Tiao, A statistical trend analysis of revised Dobson total ozone data over the Northern Hemisphere, *J. Geophys. Res.*, **95**, 9785-9807, 1990.
- Bruhl, C., S. R. Drayson, J. M. Russell III, P. J. Crutzen, J. M. McInerney, P. N. Purcell, H. Claude, H. Gernandt, T. J. McGee, I. S. McDermid, and M. R. Gunson, Halogen Occultation Experiment ozone channel validation, *J. Geophys. Res.*, **101**, 10,217-10,240, 1996.
- Chipperfield, M.P., Multiannual simulations with a three-dimensional chemical transport model, *J. Geophys. Res.*, **104**, 1781-1805, 1999.
- Crutzen, Paul J. and Uta Schmailzl, Chemical budgets of the stratosphere, *Planet. Space Sci.*, **31**, 1009-1032, 1983.
- DeMore, W.B., et al., Chemical kinetics and photochemical data for use in stratospheric modeling, in Evaluation 12, *JPL Publ. 97-4*, Jet Propul. Lab., Pasadena, Calif., 1997.
- Douglass, Anne R., Clark J. Weaver, Richard B. Rood, and Lawrence Coy, A three-dimensional simulation of the ozone annual cycle using winds from a data assimilation system, *J. Geophys. Res.*, **101**, 1463-1474, 1996.
- Douglass, A. R., M. J. Prather, T. M. Hall, S. E. Strahan, P. J. Rasch, L. C. Sparling, L. Coy, and J. M. Rodriguez, Choosing meteorological input for the global modeling initiative assessment of high-speed aircraft, *J. Geophys. Res.* **104**, 27,545-27,564, 1999.
- Eckman, R. S., W. L. Grose, R. E. Turner, W. T. Blackshear, and J. M. Russell III, Stratospheric trace constituents simulated by a three-dimensional general circulation model: Comparison with UARS data, *J. Geophys. Res.*, **100**, 13,951-13,966, 1995.
- Fairlie, T. D., W. L. Grose, R. B. Pierce, and R. S. Eckman, A Three-Dimensional Simulation of Stratospheric Ozone Using a Coupled Dynamics, Chemistry and Radiation Model: Deactivation of Inorganic Chlorine Following Antarctic Ozone Depletion, in *Proceedings of the XVIII Quadrennial Ozone Symposium, L'Aquila, Italy, 12-21 September 1996*, pp. 707-710, edited by R. Bojkov and G. Visconti, International Ozone Commission, 1998.
- Frederick, J. E., et al., Radiative processes: Solar and terrestrial, in *Atmospheric Ozone 1985*, pp. 349-392, *WMO Rep. 16*, World Meteorol. Organ., Geneva, 1986.
- Gao, R. S. et al., A comparison of observations and model simulations of NO<sub>x</sub>/NO<sub>y</sub> in the lower stratosphere, *Geophys. Res. Lett.*, **26**, 1153-1156, 1999.
- Grose, W. L., Recent advances in understanding stratospheric dynamics and transport processes: application of satellite data to their interpretation, *Adv. Space Res.*, **4**, 19-28, 1984.
- Grose, W. L., J. E. Nealy, R. E. Turner, and W. T. Blackshear, Modeling the transport of chemi-

- cally active constituents in the stratosphere, in *Transport Processes in the Middle Atmosphere*, pp. 229-250, edited by G. Visconti and R. Garcia, D. Reidel, Norwell, MA, 1987.
- Hack, J. J., B. A. Boville, J. T. Kiehl, P. J. Rasch, and D. L. Williamson, Climate statistics from the National Center for Atmospheric Research community climate model CCM2, *J. Geophys. Res.*, **99**, 20,785-20,813, 1994.
- Hadjinicolaou, P., J. A. Pyle, M. P. Chipperfield, and J. A. Kettleborough, Effect of interannual meteorological variability on mid-latitude O<sub>3</sub>, *Geophys. Res. Lett.*, **24**, 2993-2996, 1997.
- Hansen, J., G. Russell, D. Rind, P. Stone, A. Lacis, S. Lebedeff, R. Ruedy, and L. Travis, Efficient 3-D global models for climate studies: Models I and II, *Mon. Weather Rev.*, **111**, 609-662, 1983.
- Hansen, J. et al., Forcings and chaos in interannual to decadal climate change, *J. Geophys. Res.*, **102**, 25,679-25,720, 1997.
- Hanson, D., and K. Mauersberger, Laboratory studies of the nitric acid trihydrate: implications for the south polar stratosphere, *Geophys. Res. Lett.*, **15**, 855-858, 1988.
- Hanson, D. R., A. R. Ravishankara, and S. Solomon, Heterogeneous reactions in sulfuric acid aerosols: A framework for model calculations, *J. Geophys. Res.*, **99**, 3615-3629, 1994.
- Harvey, V. Lynn, Matthew H. Hitchman, R. Bradley Pierce, and T. Duncan Fairlie, Tropical aerosol in the Aleutian High, *J. Geophys. Res.*, **104**, 6281-6290, 1999.
- Johnston, H. S., Global ozone balance in the natural stratosphere, *Rev. Geophys.*, **13**, 637-649, 1975.
- Kalnay, E. et al., The NCEP/NCAR 40-year reanalysis project, *Bull. Am. Meteorol. Soc.*, **77**, 437-472, 1996.
- Kaye, J. A., A. R. Douglass, C. H. Jackman, and R. S. Stolarski, Two-Dimensional Model Calculation of Fluorine-Containing Reservoir Species in the Stratosphere, *J. Geophys. Res.*, **96**, 12,865-12,881, 1991.
- Khosravi, R., G. P. Brasseur, A. K. Smith, D. W. Rusch, J. Waters, and J. M. Russell III, Significant reduction in the stratospheric ozone deficit using a three-dimensional model constrained with UARS data, *J. Geophys. Res.*, **103**, 16,203-16,219, 1998.
- Labitzke, K. and M. P. McCormick, Stratospheric temperature increases due to Pinatubo aerosols, *Geophys. Res. Lett.*, **19**, 207-210, 1992.
- Lary, D. J., M. P. Chipperfield, R. Toumi, and T. Lenton, Heterogeneous atmospheric bromine chemistry, *J. Geophys. Res.*, **101**, 1489-1504, 1996.
- Lawrence, Bryan N, Some aspects of the sensitivity of stratospheric climate simulation to model lid height, *J. Geophys. Res.*, **102**, 23,805-23,811, 1997.
- Lipson, J. B., M. J. Elrod, T. W. Beiderhase, L. T. Molina, and M. J. Molina, Temperature dependence of the rate constant and branching ratio for the OH + ClO reaction, *J. Chem. Soc. Faraday Trans.*, **93**, 2665, 1997.
- Luo, M., J. M. Russell III, and T. Y. W. Huang, Halogen Occultation Experiment observations of the quasi-biennial oscillation and the effects of Pinatubo aerosols in the tropical stratosphere, *J. Geophys. Res.*, **102**, 19,187-19,198, 1997.
- McCormick, M. Patrick, Larry W. Thomason, and Charles R. Trepte, Atmospheric effects of the Mt. Pinatubo eruption, *Nature*, **373**, 399-404, 1995.
- Meier, R. R., D. E. Anderson, Jr., and M. Nicolet, Radiation field in the troposphere and stratosphere from 240-1000 nm - I. General analysis, *Planet. Space Sci.*, **30**, 923-933, 1982.
- Michelsen, H. A., C. M. Spivakovsky, and S. C. Wofsy, Aerosol-mediated partitioning of stratospheric Cl<sub>y</sub> and NO<sub>y</sub> at temperatures above 200 K, *Geophys. Res. Lett.*, **26**, 299-302, 1999.

- Nedoluha, G. E., D. E. Siskind, J. T. Bacmeister, R. M. Bevilacqua, and J. M. Russell III, Changes in upper stratospheric CH<sub>4</sub> and NO<sub>2</sub> as measured by HALOE and implications for changes in transport, *Geophys. Res. Lett.*, 25, 987-990, 1998.
- Nicolet, M., Photodissociation of nitric oxide in the mesosphere and stratosphere: simplified numerical relations for atmosphere model calculation, *Geophys. Res. Lett.*, 6, 866-868, 1979.
- Nicolet, M., Aeronomical aspects of mesospheric photodissociation: Processes resulting from the solar H Lyman-Alpha line, *Planet. Space Sci.*, 33, 69-80, 1985.
- Osterman, G. B. et al., Partitioning of NO<sub>y</sub> species in the summer Arctic stratosphere, *Geophys. Res. Lett.*, 26, 1157-1160, 1999.
- Park, J. H., J. M. Russell III, L. L. Gordley, S. R. Drayson, D. C. Benner, J. M. McInerney, M. R. Gunson, G. C. Toon, B. Sen, J.-F. Blavier, C. R. Webster, E. C. Zipf, P. Erdman, U. Schmidt, and C. Schiller, Validation of Halogen Occultation Experiment CH<sub>4</sub> measurements from the UARS, *J. Geophys. Res.*, 101, 10,183-10,203, 1996.
- Pierce, R. B., W. T. Blackshear, T. D. Fairlie, W. L. Grose, and R. E. Turner, The interaction of radiative and dynamical processes during a simulated sudden stratospheric warming, *J. Atmos. Sci.*, 50, 3829-3851, 1993.
- Pierce, R. B., J. A. Al-Saadi, T. D. Fairlie, J. R. Olson, R. S. Eckman, W. L. Grose, G. S. Lingenfelter, and J. M. Russell III, Large-scale stratospheric ozone photochemistry and transport during the POLARIS campaign, *J. Geophys. Res.*, 104, 26,525-26,545, 1999.
- Pierce, R. B., J. A. Al-Saadi, R. S. Eckman, T. D. Fairlie, W. L. Grose, M. M. Kleb, M. Natarajan, and J. R. Olson, Dynamical Climatology of the NASA Langley Research Center Interactive Modeling Project for Atmospheric Chemistry and Transport (IMPACT) model, *J. Geophys. Res.*, in press, 2000.
- Podolske, J. R., and M. Loewenstein, Airborne tunable diode laser spectrometer for tracer gas measurement in the lower stratosphere, *Appl. Opt.*, 32, 5324-5333, 1993.
- Portmann, Robert W. et al., Role of nitrogen oxides in the stratosphere: A Reevaluation based on laboratory studies, *Geophys. Res. Lett.*, 26, 2387-2390, 1999.
- Randel, William J. and Janel B. Cobb, Coherent variations of monthly mean total ozone and lower stratospheric temperature, *J. Geophys. Res.*, 99, 5433-5447, 1994.
- Randel, William J., Fei Wu, J. M. Russell III, J. W. Waters, and L. Froidevaux, Ozone and temperature changes in the stratosphere following the eruption of Mount Pinatubo, *J. Geophys. Res.*, 100, 16,753-16,764, 1995.
- Rasch, P. J., B. A. Boville, and G. P. Brasseur, A three-dimensional general circulation model with coupled chemistry for the middle atmosphere, *J. Geophys. Res.*, 100, 9041-9071, 1995.
- Rind, D., J. Lerner, K. Shah, and R. Suozzo, Use of on-line tracers as a diagnostic tool in general circulation model development 2. Transport between the troposphere and stratosphere, *J. Geophys. Res.*, 104, 9151-9167, 1999.
- Roche, A. E., J. B. Kumer, J. L. Mergenthaler, G. A. Ely, W. G. Uplinger, J. F. Potter, T. C. James, and L. W. Sterritt, The cryogenic limb array etalon spectrometer (CLAES) on UARS: Experiment description and performance, *J. Geophys. Res.*, 98, 10,763-10,775, 1993.
- Rodriguez, J. M. et al., Nitrogen and chlorine species in the spring Antarctic stratosphere: comparison of models with airborne Antarctic ozone experiment observations, *J. Geophys. Res.*, 94, 16,683-16,703, 1989.
- Rosenfield, Joan E., David B. Considine, Paul E. Meade, Julio T. Bacmeister, Charles H. Jackman, and Mark R. Schoeberl, Stratospheric effects of Mount Pinatubo aerosol studied with a coupled two-dimensional model, *J. Geophys. Res.*, 102, 3649-3670, 1997.

- Russell, J. M. III, L. L. Gordley, J. H. Park, S. R. Drayson, W. D. Hesketh, R. J. Cicerone, A. F. Tuck, J. E. Frederick, J. E. Harries, and P. J. Crutzen, The Halogen Occultation Experiment, *J. Geophys. Res.*, **98**, 10,777-10,798, 1993.
- Russell, J. M. III, L. E. Deaver, M. Luo, J. H. Park, L. L. Gordley, A. F. Tuck, G. C. Toon, M. R. Gunson, W. A. Traub, D. G. Johnson, K. W. Jucks, D. G. Murcray, R. Zander, I. G. Nolt, C. R. Webster, Validation of hydrogen chloride measurements made by the Halogen Occultation Experiment from the UARS platform, *J. Geophys. Res.*, **101**, 10,151-10,162, 1996.
- Salby, Murry, Patrick Callaghan, and Dennis Shea, Interdependence of the tropical and extratropical QBO: Relationship to the solar cycle versus a biennial oscillation in the stratosphere, *J. Geophys. Res.*, **102**, 29,789-29,798, 1997.
- Schubert, S. D., R. B. Rood, and J. Pfaendtner, An assimilated data set for Earth science application, *Bull. Am. Meteorol. Soc.*, **74**, 2331-2342, 1993.
- Shindell, Drew T., David Rind, and Patrick Lonergan, Increased polar stratospheric ozone losses and delayed eventual recovery owing to increasing greenhouse-gas concentrations, *Nature*, **392**, 589-592, 1998.
- Solomon, S., R. W. Portmann, R. R. Garcia, L. W. Thomason, L. R. Poole, and M. P. McCormick, The role of aerosol variations in anthropogenic ozone depletion at northern midlatitudes, *J. Geophys. Res.*, **101**, 6713-6727, 1996.
- Steil, B., M. Dameris, C. Bruhl, P. J. Crutzen, V. Grewe, M. Ponater, and R. Sausen, Development of a chemistry module for GCMs: first results of a multiannual integration, *Ann. Geophysicae*, **16**, 205-228, 1998.
- Stenchikov, Georgiy L. et. al., Radiative forcing from the 1991 Mount Pinatubo volcanic eruption, *J. Geophys. Res.*, **103**, 13,837-13,857, 1998.
- Stimpfle, R. M., et al., The response of ClO radical concentrations to variations in NO<sub>2</sub> radical concentrations in the lower stratosphere, *Geophys. Res. Lett.*, **21**, 2543-2546, 1994.
- Thomason, L. W., L. R. Poole, and T. Deshler, A global climatology of stratospheric aerosol surface area density deduced from Stratospheric Aerosol and Gas Experiment II measurements: 1984-1994, *J. Geophys. Res.*, **102**, 8967-8976, 1997.
- Tie, Xue Xi and Guy Brasseur, The response of stratospheric ozone to volcanic eruptions: Sensitivity to atmospheric chlorine loading, *Geophys. Res. Lett.*, **22**, 3035-3038, 1995.
- Tie, Xue Xi and Guy Brasseur, The importance of heterogeneous bromine chemistry in the lower stratosphere, *Geophys. Res. Lett.*, **23**, 2505-2508, 1996.
- Tie, Xue Xi, Guy P. Brasseur, Bruce Briegleb, and Claire Granier, Two-dimensional simulation of Pinatubo aerosol and its effect on stratospheric ozone, *J. Geophys. Res.*, **99**, 20,545-20,562, 1994.
- Tie, Xue Xi, Claire Granier, William Randel, and Guy P. Brasseur, Effects of interannual variation of temperature on heterogeneous reactions and stratospheric ozone, *J. Geophys. Res.*, **102**, 23,519-23,527, 1997.
- Wennberg, P. O. et al., Removal of Stratospheric O<sub>3</sub> by Radicals: In Situ Measurements of OH, HO<sub>2</sub>, NO, NO<sub>2</sub>, ClO, and BrO, *Science*, **266**, 398-404, 1994.
- World Meteorological Organization (WMO), Scientific assessment of ozone depletion: 1991, *WMO Rep. 25*, World Meteorol. Organ., Geneva, 1991.
- World Meteorological Organization (WMO), Scientific assessment of ozone depletion: 1998, *WMO Rep. 44*, World Meteorol. Organ., Geneva, 1999.
- Zhao, Xuepeng, Richard P. Turco, C.-Y. Jim Kao, and Scott Elliott, Aerosol-induced chemical perturbations of stratospheric ozone: Three-dimensional simulations and analysis of mecha-

nisms, *J. Geophys. Res.*, *102*, 3617-3637, 1997.



## Figure Captions

- Figure 1.** Altitude versus latitude cross-sections of zonally- and seasonally-averaged methane obtained from approximately 7 years of data. HALOE V19 data from 1993-1999. (a) DJF HALOE observations (ppmv). (b) DJF IMPACT model results (ppmv). (c) DJF percent differences (model minus HALOE). (d) JJA HALOE observations (ppmv). (e) JJA IMPACT model results (ppmv). (f) JJA percent differences (model minus HALOE).
- Figure 2.** As in figure 1, except for ozone (ppmv).
- Figure 3.** As in figure 1, except for HCl (ppbv).
- Figure 4.** Baseline monthly-mean column ozone (Dobson Units) and standard deviation computed from 7 years of data. TOMS data from 1984-1990 with QBO, ENSO, and solar cycles removed (see text). (a) TOMS column O<sub>3</sub>. (b) Model column O<sub>3</sub>. (c) Difference in column O<sub>3</sub> (model minus TOMS). (d) TOMS standard deviation in column O<sub>3</sub>. (e) Model standard deviation in column O<sub>3</sub>. (f) Difference in column O<sub>3</sub> standard deviation (model minus TOMS).
- Figure 5.** Polar area where monthly-average temperature is colder than 195 K at 50 mb computed from the model and NCEP data. (a) Southern Hemisphere. (b) Northern Hemisphere.
- Figure 6.** Northern hemisphere 50 mb polar orthographic maps from the AHS elevated-aerosol simulation on March 17 of Year 3 (1992). (a) CH<sub>4</sub> (ppmv). (b) SAD ( $\mu\text{m}^2 \text{cm}^{-3}$ ).
- Figure 7.** September zonal-mean cross sections of aerosol surface area density (SAD) for the 4 successive years of the AHS elevated-aerosol simulation ( $\mu\text{m}^2 \text{cm}^{-3}$ ). (a) Year 2 (1991). (b) Year 3 (1992). (c) Year 4 (1993). (d) Year 5 (1994).
- Figure 8.** September cross sections of the zonally- and monthly-averaged aerosol radiative heating anomaly for the 4 successive years simulated (K/day). Contour levels  $\pm 0.01$ ,  $\pm 0.05$ ,  $\pm 0.10$ ,  $\pm 0.20$ , and  $\pm 0.30$ . (a) 1991. (b) 1992. (c) 1993. (d) 1994.
- Figure 9.** Timeseries of modeled total column ozone (Dobson Units) as a function of latitude. Contour interval 25 Dobson Units. (a) BL1 baseline simulation. (b) AHS elevated aerosol simulation. (c) AHS minus BL1. Contour levels of  $\pm 10$  added.
- Figure 10.** Timeseries of near-global (60S-60N) area-weighted mean column ozone from IMPACT model simulations and TOMS observations. Solid line is annually-repeating mean computed from 7 model baseline years, shading indicates baseline 1- and 2-sigma interannual standard deviation. TOMS observations adjusted for QBO, ENSO, solar (see text).
- Figure 11.** Timeseries of modeled monthly-mean column ozone change (percent) due to elevated aerosol heating and to both elevated heating and SAD. Shading indicates baseline 1- and 2-sigma interannual standard deviation. (a) Near-global. (b) Tropical. (c) NH mid-latitude. (d) SH mid-latitude. (e) NH high-latitude. (f) SH high-latitude.
- Figure 12.** Timeseries of monthly-mean column ozone response to elevated aerosol computed from TOMS data (see text for details). Shading indicates baseline 1- and 2-sigma interannual standard deviation. (a) Near-global. (b) Tropical. (c) NH mid-latitude. (d) SH mid-latitude. (e) NH high-latitude. (f) SH high-latitude.
- Figure 13.** Annually-averaged TEM circulation and vertical velocity for the first year following the eruption, June Year 2 (1991) through May Year 3 (1992). (a) TEM circulation from AHS simulation ( $\text{kg m}^{-1} \text{s}^{-1}$ ). (b) W velocity from AHS simulation ( $\text{kg m}^{-2} \text{s}^{-1}$ ). (c) TEM anomaly (AHS-BL1) ( $\text{kg m}^{-1} \text{s}^{-1}$ ). Shading indicates changes exceeding 1- and 2-sigma interannual variability. (d) W anomaly (AHS-BL1) ( $\text{kg m}^{-2} \text{s}^{-1}$ ). Shading as in panel (c).
- Figure 14.** Altitude-latitude cross-sections averaged over the June/July/August period of Year 3

(1992) from the elevated aerosol simulation (AHS), and aerosol-induced anomalies. (a) Temperature (K). (b) Methane (ppmv). (c) Ox (ppmv). (d) Temperature anomaly (K). (e) Methane anomaly (ppmv). (f) Ox anomaly (ppmv).

**Figure 15.** As in figure 14, except for nitrogen species (ppbv). (a) NO<sub>y</sub>. (b) HNO<sub>3</sub>. (c) NO<sub>x</sub>. (d) N<sub>2</sub>O<sub>5</sub>. (e) NO<sub>y</sub> anomaly. (f) HNO<sub>3</sub> anomaly. (g) NO<sub>x</sub> anomaly. (h) N<sub>2</sub>O<sub>5</sub> anomaly.

**Figure 16.** As in figure 14, except for chlorine species (ppbv). (a) Cly. (b) HCl. (c) Cl<sub>x</sub>. (d) ClONO<sub>2</sub>. (e) Cly anomaly. (f) HCl anomaly. (g) Cl<sub>x</sub> anomaly. (h) ClONO<sub>2</sub> anomaly.

**Figure 17.** Altitude-time series of globally-averaged model response to elevated aerosol. Shading indicates changes exceeding 1-sigma and 2-sigma interannual standard deviation. Zero contours not shown. Panels (a)-(c) show response to aerosol heating and SAD combined, panels (d)-(f) show response to aerosol heating only. (a) Temperature (K). (b) Methane (ppmv). (c) Ozone (ppmv). (d) Temperature (K). (e) Methane (ppmv). (f) Ozone (ppmv).

**Figure 18.** Temperature anomaly (K) versus odd oxygen anomaly (ppmv) resulting from elevated SAD only (AHS minus AH).

**Figure 19.** As in figure 17, except response in nitrogen species (ppbv) to aerosol heating and SAD combined. (a) NO<sub>y</sub>. (b) NO<sub>x</sub>. (c) HNO<sub>3</sub>. (d) N<sub>2</sub>O<sub>5</sub>.

**Figure 20.** As in figure 17, except response of chlorine species (ppbv) to aerosol heating only. (a) Cly. (b) Cl<sub>x</sub>. (c) HCl. (d) ClONO<sub>2</sub>.

**Figure 21.** As in figure 17, except response of chlorine species (ppbv) to elevated SAD only. (a) Cly. (b) Cl<sub>x</sub>. (c) HCl. (d) ClONO<sub>2</sub>.

**Figure 22.** As in figure 17, except response in chlorine species (ppbv) to aerosol heating and SAD combined. (a) Cly. (b) Cl<sub>x</sub>. (c) HCl. (d) ClONO<sub>2</sub>.

**Figure 23.** Zonally averaged quantities simulated by the model and observed by the UARS satellite at 30 mb during May 1992. Model results from mean baseline (BLC) and elevated-aerosol (AH and AHS) simulations. (a) Temperature (K) with HALOE observations. (b) CH<sub>4</sub> (ppmv) with HALOE observations. (c) O<sub>3</sub> (ppmv) with HALOE observations. (d) HNO<sub>3</sub> (ppbv) with CLAES observations. (e) HCl (ppbv) with HALOE observations. (f) ClONO<sub>2</sub> (ppbv) with CLAES observations.

**Figure 24.** Latitudinal distribution of odd-oxygen photochemical loss during May of Year 3 (1992) at 30 mb from the baseline (BL1) and elevated-aerosol (AHS) simulations. (a) Total photochemical loss (ppmv/month). (b) Fraction due to nitrogen-catalyzed cycles. (c) Fraction due to halogen-catalyzed cycles. (d) Fraction due to hydrogen-catalyzed cycles.

**Figure 25.** As in figure 24, except at 20 mb.

**Table 1.** Maxima in total column ozone anomaly (%) with post-Pinatubo aerosol loading. Variability estimates shown are 95% confidence limits for ground-based analysis and pre-volcanic yearly 2-sigma standard deviations for TOMS analysis and model results. Shown in parenthesis is the approximate number of months from the eruption to the anomaly maxima.

	Ground-based Dobson [Angell, 1997(a)]	TOMS (present analysis)	IMPACT model
Global	-1.9±0.7 (15)	-3.2±1.1 (16)	-3.8±1.1 (20); -3.7±0.7 (16)
Tropical	-1.7±1.4 (27)	-3.8±1.5 (12)	-5.2±0.6 (5); -4.7±1.9 (13)
NH mid-latitude	-6.1±1.6 (21)	-9.9±3.5 (20)	-3.8±1.5 (20)

**Table A1.** Chemical constituents used in the Model

No.	Constituent	No.	Constituent
(1)	O <sub>3</sub>	(28)	N
(2)	O	(29)	Cl <sub>2</sub>
(3)	NO	(30)	CH <sub>3</sub>
(4)	NO <sub>2</sub>	(31)	HCO
(5)	HNO <sub>3</sub>	(32)	CH <sub>3</sub> O <sub>2</sub>
(6)	HNO <sub>2</sub>	(33)	CH <sub>3</sub> O
(7)	NO <sub>3</sub>	(34)	ClO <sub>2</sub>
(8)	H <sub>2</sub> O <sub>2</sub>	(35)	O <sub>2</sub>
(9)	OH	(36)	H <sub>2</sub>
(10)	HO <sub>2</sub>	(37)	CH <sub>3</sub> CCl <sub>3</sub>
(11)	N <sub>2</sub> O	(38)	HOCl
(12)	N <sub>2</sub> O <sub>5</sub>	(39)	HO <sub>2</sub> NO <sub>2</sub>
(13)	H <sub>2</sub> O	(40)	Cl <sub>2</sub> O <sub>2</sub>
(14)	HCl	(41)	OCIO
(15)	CF <sub>2</sub> Cl <sub>2</sub>	(42)	Br
(16)	CFCl <sub>3</sub>	(43)	BrCl
(17)	ClONO <sub>2</sub>	(44)	BrO
(18)	CH <sub>4</sub>	(45)	HBr
(19)	CH <sub>2</sub> O	(46)	HOBr
(20)	CO	(47)	BrONO <sub>2</sub>
(21)	CH <sub>3</sub> OOH	(48)	CH <sub>3</sub> Br
(22)	CCl <sub>4</sub>	(49)	CF <sub>3</sub> Br
(23)	CH <sub>3</sub> Cl	(50)	CF <sub>2</sub> ClBr
(24)	Cl	(51)	HF
(25)	ClO	(52)	CFCIO
(26)	H	(53)	CF <sub>2</sub> O
(27)	O( <sup>1</sup> D)		

**Table A2.** Photolytic Reactions Used in the Model

No.	Reaction	No.	Reaction
(1)	$\text{O}_2 + h\nu \rightarrow 2\text{O}$	(22)	$\text{CCl}_4 + h\nu \rightarrow 4\text{Cl} + \text{products}$
(2)	$\text{O}_3 + h\nu \rightarrow \text{O}_2 + \text{O}$	(23)	$\text{CH}_3\text{Cl} + h\nu \rightarrow \text{CH}_3 + \text{Cl}$
(3)	$\text{O}_3 + h\nu \rightarrow \text{O}_2 + \text{O}(^1\text{D})$	(24)	$\text{CH}_2\text{O} + h\nu \rightarrow \text{H} + \text{HCO}$
(4)	$\text{NO}_2 + h\nu \rightarrow \text{NO} + \text{O}$	(25)	$\text{CH}_2\text{O} + h\nu \rightarrow \text{CO} + \text{H}_2$
(5)	$\text{CH}_3\text{CCl}_3 + h\nu \rightarrow 3\text{Cl} + \text{products}$	(26)	$\text{HOCl} + h\nu \rightarrow \text{Cl} + \text{OH}$
(6)	$\text{HNO}_3 + h\nu \rightarrow \text{NO}_2 + \text{OH}$	(27)	$\text{HO}_2\text{NO}_2 + h\nu \rightarrow \text{HO}_2 + \text{NO}_2$
(7)	$\text{HNO}_2 + h\nu \rightarrow \text{NO} + \text{OH}$	(28)	$\text{CH}_3\text{OOH} + h\nu \rightarrow \text{CH}_3\text{O} + \text{OH}$
(8)	$\text{H}_2\text{O} + h\nu \rightarrow \text{H} + \text{OH}$	(29)	$\text{Cl}_2\text{O}_2 + h\nu \rightarrow \text{Cl} + \text{ClO}_2$
(9)	$\text{H}_2\text{O}_2 + h\nu \rightarrow 2\text{OH}$	(30)	$\text{OCIO} + h\nu \rightarrow \text{O} + \text{ClO}$
(10)	$\text{NO}_3 + h\nu \rightarrow \text{O}_2 + \text{NO}$	(31)	$\text{BrCl} + h\nu \rightarrow \text{Br} + \text{Cl}$
(11)	$\text{NO}_3 + h\nu \rightarrow \text{O} + \text{NO}_2$	(32)	$\text{BrO} + h\nu \rightarrow \text{Br} + \text{O}$
(12)	$\text{N}_2\text{O} + h\nu \rightarrow \text{N}_2 + \text{O}(^1\text{D})$	(33)	$\text{HBr} + h\nu \rightarrow \text{H} + \text{Br}$
(13)	$\text{N}_2\text{O}_5 + h\nu \rightarrow \text{NO}_2 + \text{NO}_3$	(34)	$\text{HOBr} + h\nu \rightarrow \text{Br} + \text{OH}$
(14)	$\text{NO} + h\nu \rightarrow \text{N} + \text{O}$	(35)	$\text{BrONO}_2 + h\nu \rightarrow \text{BrO} + \text{NO}_2$
(15)	$\text{HCl} + h\nu \rightarrow \text{H} + \text{Cl}$	(36)	$\text{CH}_3\text{Br} + h\nu \rightarrow \text{Br} + \text{CH}_3$
(16)	$\text{ClO}_2 + h\nu \rightarrow \text{O} + \text{ClO}$	(37)	$\text{CF}_3\text{Br} + h\nu \rightarrow \text{Br} + \text{products}$
(17)	$\text{ClO} + h\nu \rightarrow \text{O} + \text{Cl}$	(38)	$\text{CF}_2\text{ClBr} + h\nu \rightarrow \text{Br} + \text{Cl} + \text{products}$
(18)	$\text{Cl}_2 + h\nu \rightarrow 2\text{Cl}$	(39)	$\text{CFCIO} + h\nu \rightarrow \text{HF} + \text{products}$
(19)	$\text{CFCl}_3 + h\nu \rightarrow 3\text{Cl} + \text{F} + \text{products}$	(40)	$\text{CF}_2\text{O} + h\nu \rightarrow 2\text{HF} + \text{products}$
(20)	$\text{CF}_2\text{Cl}_2 + h\nu \rightarrow 2\text{Cl} + 2\text{F} + \text{products}$	(41)	$\text{CH}_4 + h\nu \rightarrow \text{CH}_2 + \text{H}_2 \text{ (90\%)}$
(21)	$\text{ClONO}_2 + h\nu \rightarrow \text{ClO} + \text{NO}_2$		$\text{CH}_4 + h\nu \rightarrow \text{CH} + \text{H}_2 + \text{H} \text{ (10\%)}$

**Table A3.** Chemical Reactions Used in the Model

No.	Reaction	No.	Reaction
(1)	$O_2 + O(^1D) \rightarrow O_2 + O$	(54)	$HCl + O \rightarrow Cl + OH$
(2)	$N_2 + O(^1D) \rightarrow N_2 + O$	(55)	$Cl + O_2 + M \rightarrow ClO_2 + M$
(3)	$H_2O + O(^1D) \rightarrow 2OH$	(56)	$ClO_2 + M \rightarrow Cl + O_2 + M$
(4)	$O + O_2 + M \rightarrow O_3 + M$	(57)	$HO_2 + NO_2 + M \rightarrow HO_2NO_2 + M$
(5)	$O_3 + O \rightarrow 2O_2$	(58)	$Cl + ClO_2 \rightarrow 2ClO$
(6)	$O + OH \rightarrow H + O_2$	(59)	$Cl + ClO_2 \rightarrow Cl_2 + O_2$
(7)	$O + HO_2 \rightarrow OH + O_2$	(60)	$ClO + ClO + M \rightarrow Cl_2O_2 + M$
(8)	$NO_2 + O \rightarrow NO + O_2$	(61)	$Cl_2O_2 + M \rightarrow ClO + ClO$
(9)	$Cl + CH_2O \rightarrow HCl + HCO$	(62)	$HO_2NO_2 + M \rightarrow HO_2 + NO_2 + M$
(10)	$O + CH_2O \rightarrow OH + HCO$	(63)	$ClONO_2 + OH \rightarrow HOCl + NO_3$
(11)	$H + O_2 + M \rightarrow HO_2 + M$	(64)	$2OH + M \rightarrow H_2O_2 + M$
(12)	$O_3 + OH \rightarrow HO_2 + O_2$	(65)	$H_2O_2 + O \rightarrow OH + HO_2$
(13)	$O_3 + NO \rightarrow NO_2 + O_2$	(66)	$CH_4 + OH \rightarrow CH_3 + H_2O$
(14)	$NO_2 + O_3 \rightarrow NO_3 + O_2$	(67)	$ClO + NO_2 + M \rightarrow ClONO_2 + M$
(15)	$O_3 + H \rightarrow OH + O_2$	(68)	$ClONO_2 + HCl(s) \rightarrow Cl_2 + HNO_3(s)$
(16)	$2OH \rightarrow H_2O + O$	(69)	$ClONO_2 + O \rightarrow ClO + NO_3$
(17)	$OH + HO_2 \rightarrow H_2O + O$	(70)	$HO_2NO_2 + OH \rightarrow NO_2 + O_2 + H_2O$
	$OH + HO_2 + M \rightarrow H_2O + O_2 + M$	(71)	$HCl + O(^1D) \rightarrow Cl + OH$
(18)	$OH + NO_2 + M \rightarrow HNO_3 + M$	(72)	$H_2 + OH \rightarrow H_2O + H$
(19)	$OH + NO + M \rightarrow HNO_2 + M$	(73)	$ClONO_2 + H_2O(s) \rightarrow HOCl + HNO_3(s)$
(20)	$HO_2 + NO \rightarrow OH + NO_2$	(74)	$CF_2Cl_2 + O(^1D) \rightarrow 2Cl + \text{products}$
(21)	$OH + H_2O_2 \rightarrow H_2O + HO_2$	(75)	$CFCl_3 + O(^1D) \rightarrow 3Cl + \text{products}$
(22)	$2HO_2 \rightarrow H_2O_2 + O_2$	(76)	$N_2O_5 + HCl(s) \rightarrow ClONO_2 + HNO_3(s)$
	$2HO_2 + M \rightarrow H_2O_2 + O_2 + M$	(77)	$CH_3 + O_2 + M \rightarrow CH_3O_2 + M$
(23)	$NO + NO_3 \rightarrow 2NO_2$	(78)	$CH_3O_2 + HO_2 \rightarrow CH_3OOH + O_2$
(24)	$NO + O + M \rightarrow NO_2 + M$	(79)	$CH_3O_2 + NO \rightarrow CH_3O + NO_2$
(25)	$O(^1D) + N_2O \rightarrow N_2 + O_2$	(80)	$N_2O_5 + H_2O(s) \rightarrow 2HNO_3(s)$
(26)	$O(^1D) + N_2O \rightarrow 2NO$	(81)	$ClO + OH \rightarrow Cl + HO_2$ (95%)
(27)	$O(^1D) + N_2 + M \rightarrow N_2O + M$		$ClO + OH \rightarrow HCl + O_2$ (5%)
(28)	$O_3 + HO_2 \rightarrow OH + 2O_2$	(82)	$CH_3O + O_2 \rightarrow CH_2O + HO_2$
(29)	$HNO_3 + OH \rightarrow H_2O + NO_3$	(83)	$CH_2O + OH \rightarrow HCO + H_2O$
(30)	$O(^1D) + H_2 \rightarrow H + OH$	(84)	$HCO + O_2 \rightarrow CO + HO_2$
(31)	$OH + CH_3CCl_3 \rightarrow 3Cl + \text{products}$	(85)	$CO + OH \rightarrow H + CO_2$
(32)	$O(^1D) + CH_4 \rightarrow CH_3 + OH$	(86)	$CH_3Cl + OH \rightarrow Cl + \text{products}$
(33)	$HO_2 + ClO \rightarrow HOCl + O_2$	(87)	$CH_3OOH + OH \rightarrow CH_3O_2 + H_2O$
(34)	$NO_2 + O + M \rightarrow NO_3 + M$	(88)	$N_2O_5 + H_2O(l) \rightarrow 2HNO_3$
(35)	$NO_2 + NO_3 + M \rightarrow N_2O_5 + M$	(89)	$ClONO_2 + H_2O(l) \rightarrow HNO_3 + HOCl$
(36)	$N_2O_5 + M \rightarrow NO_2 + NO_3 + M$	(90)	$CH_3Br + OH \rightarrow Br + H_2O$

**Table A3.** Chemical Reactions Used in the Model

No.	Reaction	No.	Reaction
(37)		(91)	$\text{ClO} + \text{ClO} \rightarrow \text{Cl} + \text{OClO}$
(38)		(92)	$\text{ClO} + \text{ClO} \rightarrow \text{Cl} + \text{ClO}_2$
(39)	$\text{N} + \text{NO}_2 \rightarrow \text{N}_2\text{O} + \text{O}$	(93)	$\text{ClO} + \text{ClO} \rightarrow \text{Cl}_2 + \text{O}_2$
(40)	$\text{N} + \text{O}_2 \rightarrow \text{NO} + \text{O}$	(94)	$\text{Br} + \text{O}_3 \rightarrow \text{BrO} + \text{O}_2$
(41)	$\text{N} + \text{NO} \rightarrow \text{N}_2 + \text{O}$	(95)	$\text{Br} + \text{HO}_2 \rightarrow \text{HBr} + \text{O}_2$
(42)	$\text{O} + \text{HOCl} \rightarrow \text{OH} + \text{ClO}$	(96)	$\text{Br} + \text{CH}_2\text{O} \rightarrow \text{HBr} + \text{HCO}$
(43)	$\text{HOCl} + \text{HCl(s)} \rightarrow \text{Cl}_2 + \text{H}_2\text{O(s)}$	(97)	$\text{BrO} + \text{O} \rightarrow \text{Br} + \text{O}_2$
(44)	$\text{Cl} + \text{O}_3 \rightarrow \text{ClO} + \text{O}_2$	(98)	$\text{BrO} + \text{HO}_2 \rightarrow \text{HOBr} + \text{O}_2$
(45)	$\text{ClO} + \text{O} \rightarrow \text{Cl} + \text{O}_2$	(99)	$\text{BrO} + \text{NO} \rightarrow \text{Br} + \text{NO}_2$
(46)	$\text{ClO} + \text{NO} \rightarrow \text{Cl} + \text{NO}_2$	(100)	$\text{BrO} + \text{NO}_2 + \text{M} \rightarrow \text{BrONO}_2 + \text{M}$
(47)	$\text{CH}_4 + \text{Cl} \rightarrow \text{CH}_3 + \text{HCl}$	(101)	$\text{BrO} + \text{ClO} \rightarrow \text{Br} + \text{OClO}$
(48)	$\text{H}_2 + \text{Cl} \rightarrow \text{H} + \text{HCl}$	(102)	$\text{BrO} + \text{ClO} \rightarrow \text{Br} + \text{ClO}_2$
(49)	$\text{Cl} + \text{HO}_2 \rightarrow \text{HCl} + \text{O}_2$	(103)	$\text{BrO} + \text{ClO} \rightarrow \text{BrCl} + \text{O}_2$
(50)	$\text{Cl} + \text{H}_2\text{O}_2 \rightarrow \text{HCl} + \text{HO}_2$	(104)	$\text{BrO} + \text{BrO} \rightarrow 2\text{Br} + \text{O}_2$
(51)	$\text{ClONO}_2 + \text{Cl} \rightarrow \text{Cl}_2 + \text{NO}_3$	(105)	$\text{HBr} + \text{OH} \rightarrow \text{Br} + \text{H}_2\text{O}$
(52)	$\text{HOCl} + \text{OH} \rightarrow \text{ClO} + \text{H}_2\text{O}$	(106)	$\text{CFClO} + \text{O}(^1\text{D}) \rightarrow \text{products}$
(53)	$\text{HCl} + \text{OH} \rightarrow \text{Cl} + \text{H}_2\text{O}$	(107)	$\text{CF}_2\text{O} + \text{O}(^1\text{D}) \rightarrow \text{products}$

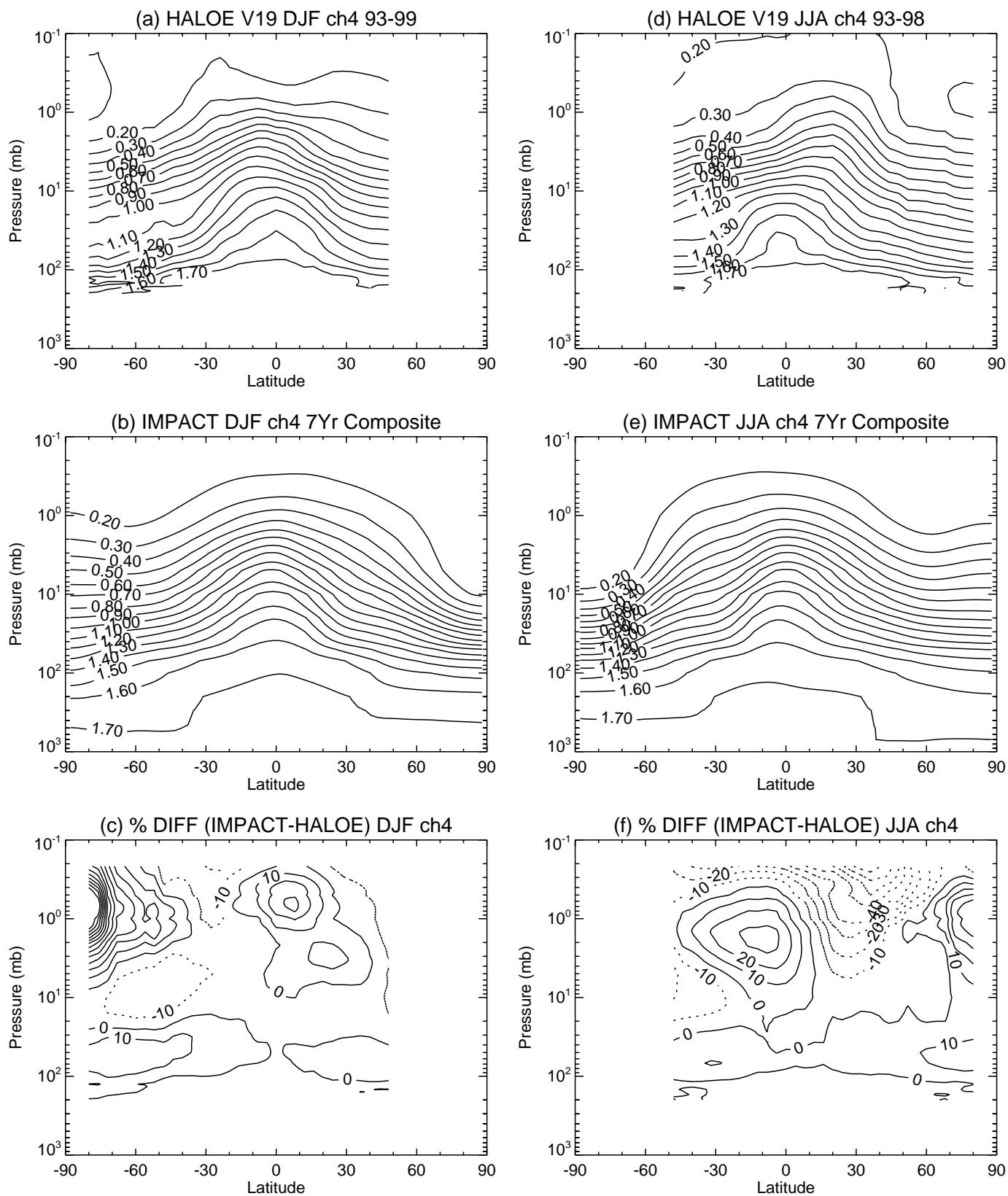


Figure 1



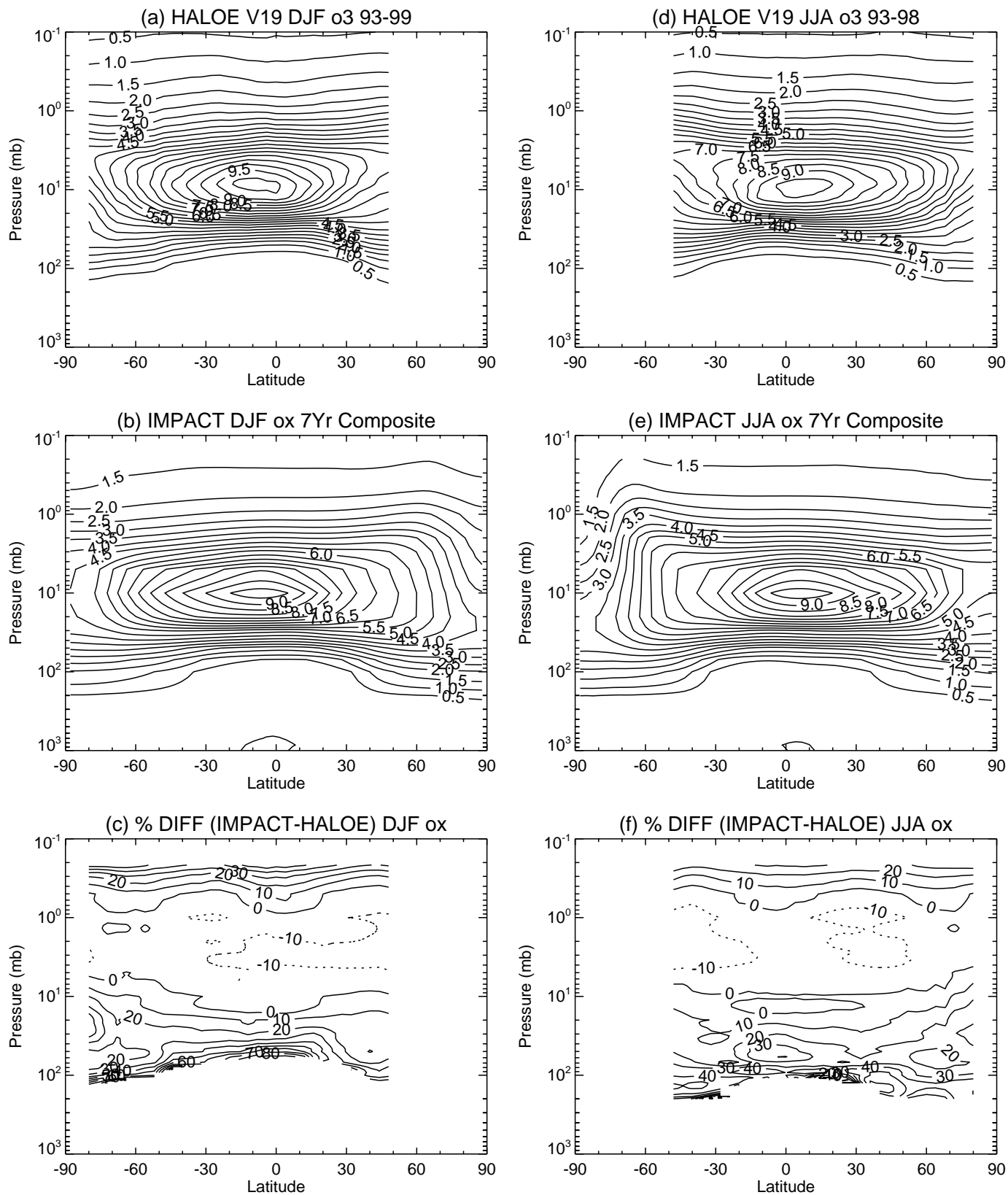


Figure 2

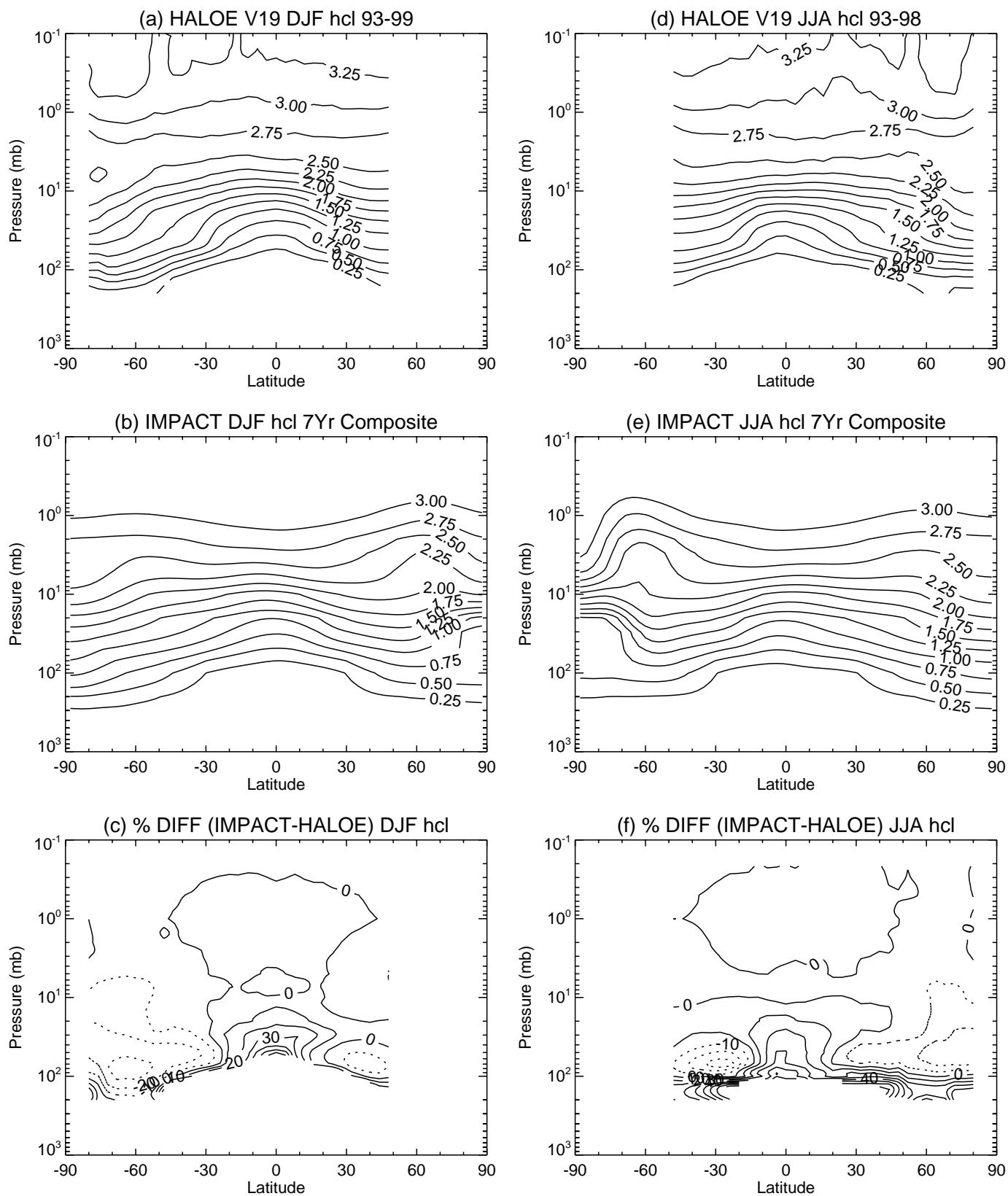


Figure 3

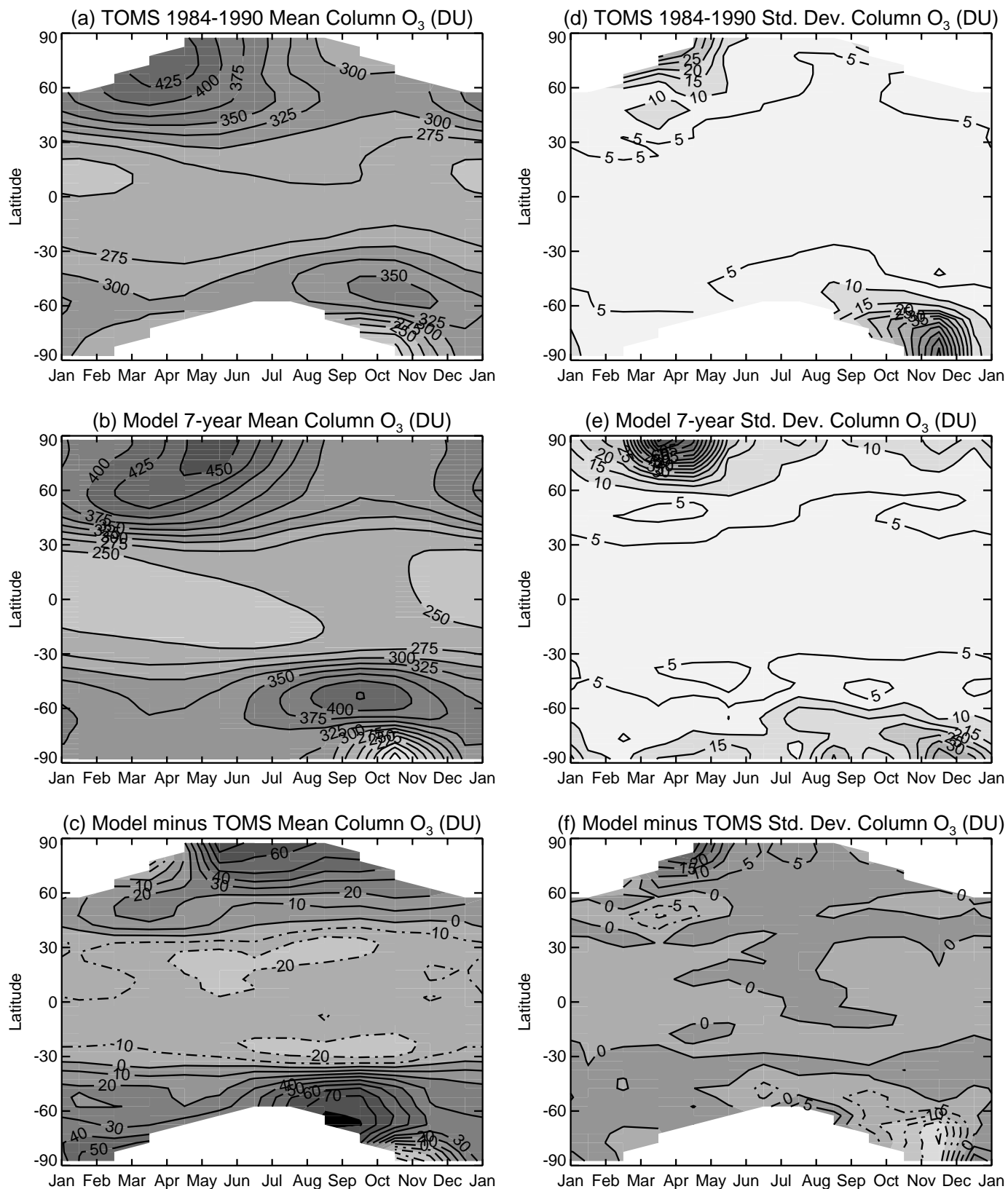


Figure 4

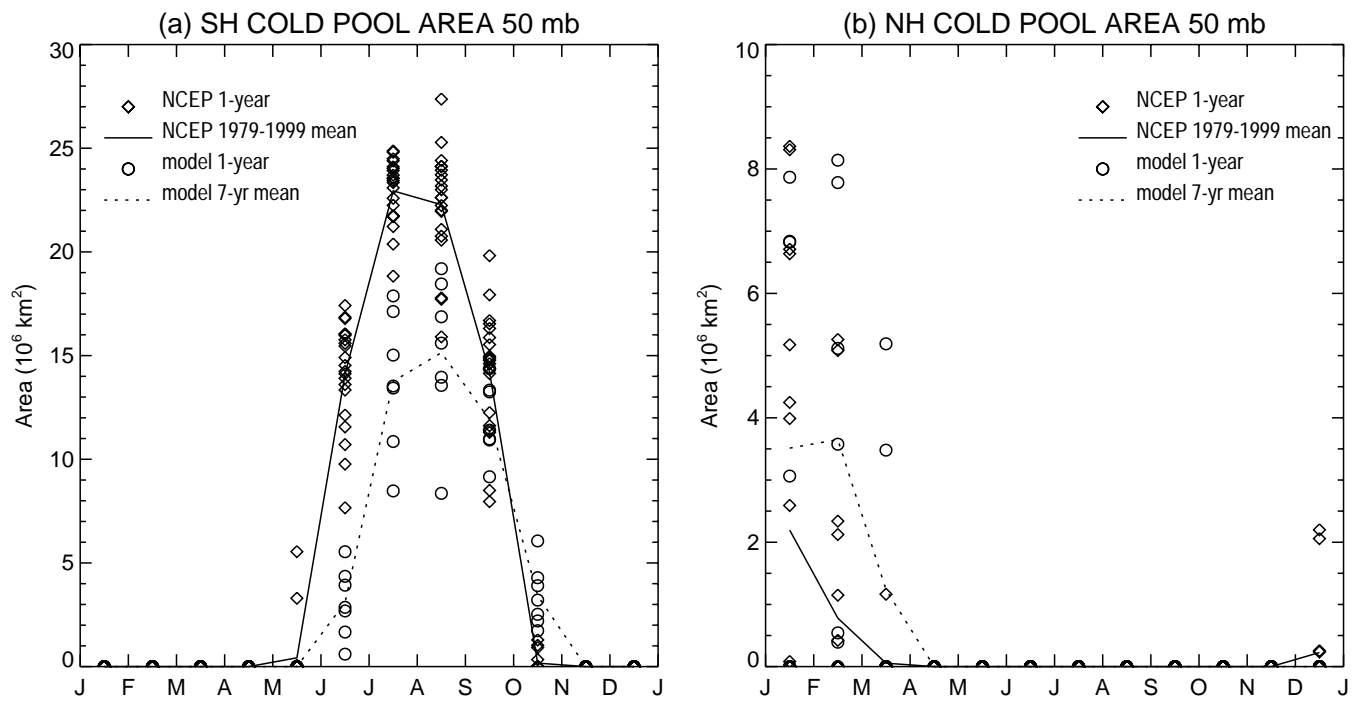
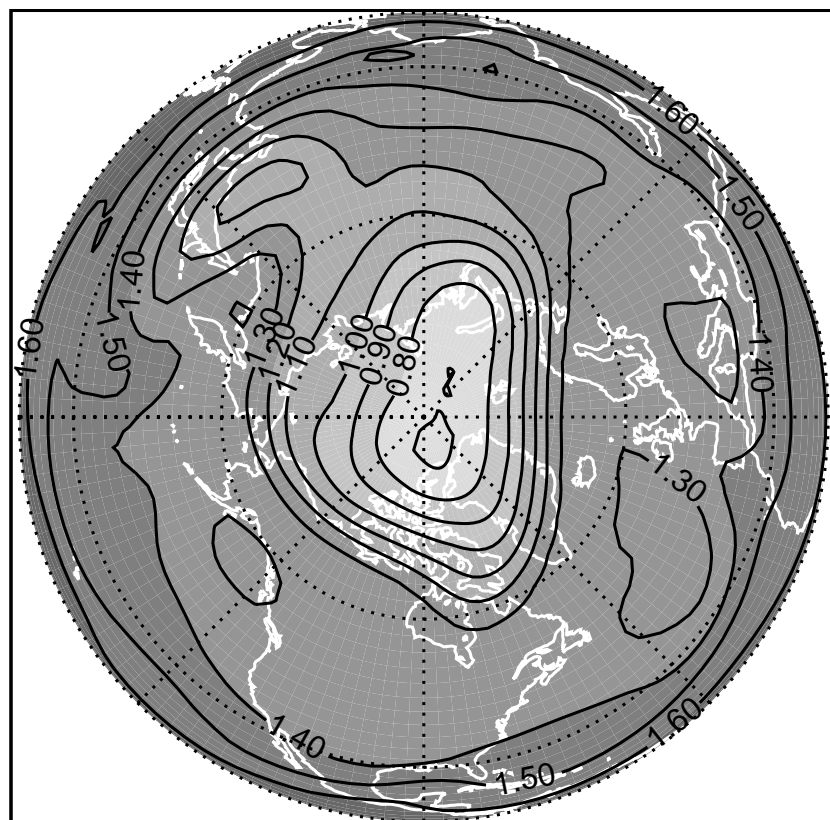


Figure 5

(a) CH<sub>4</sub>



(b) SAD

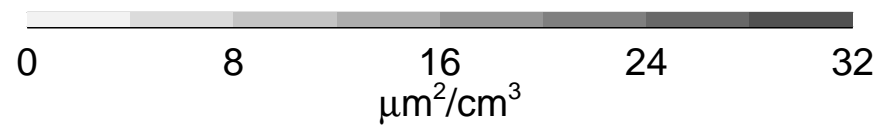
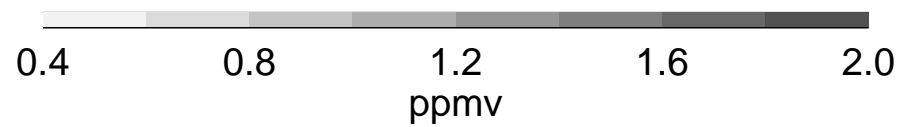
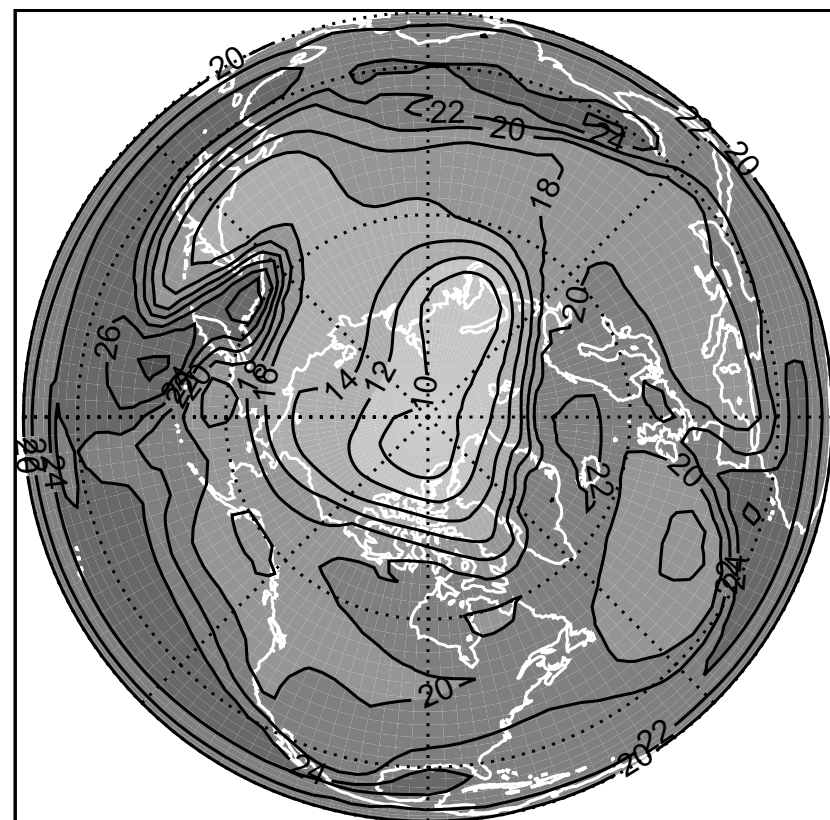


Figure 6

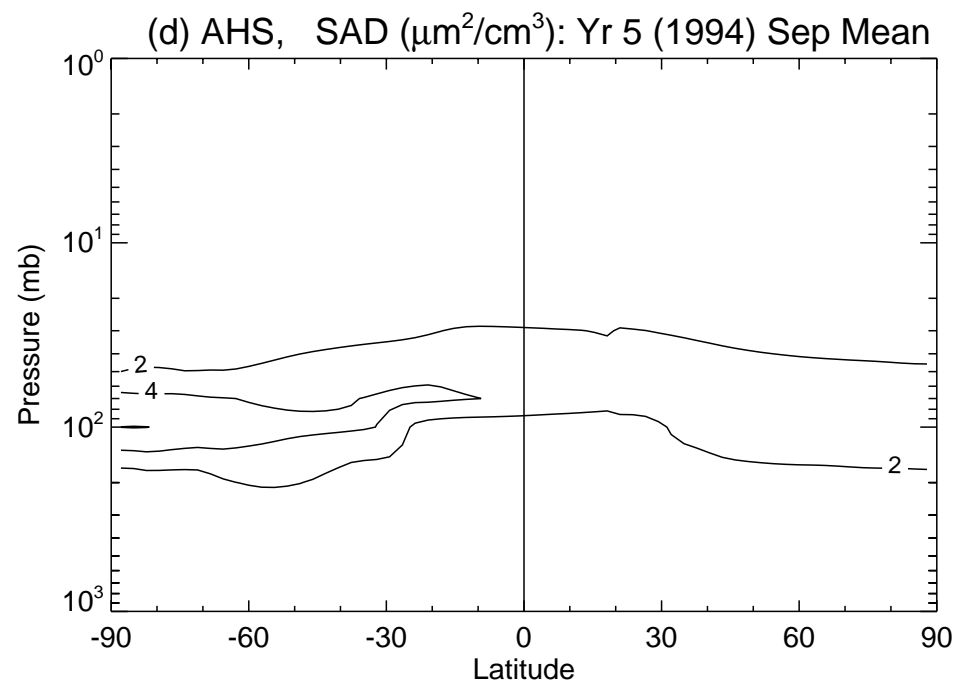
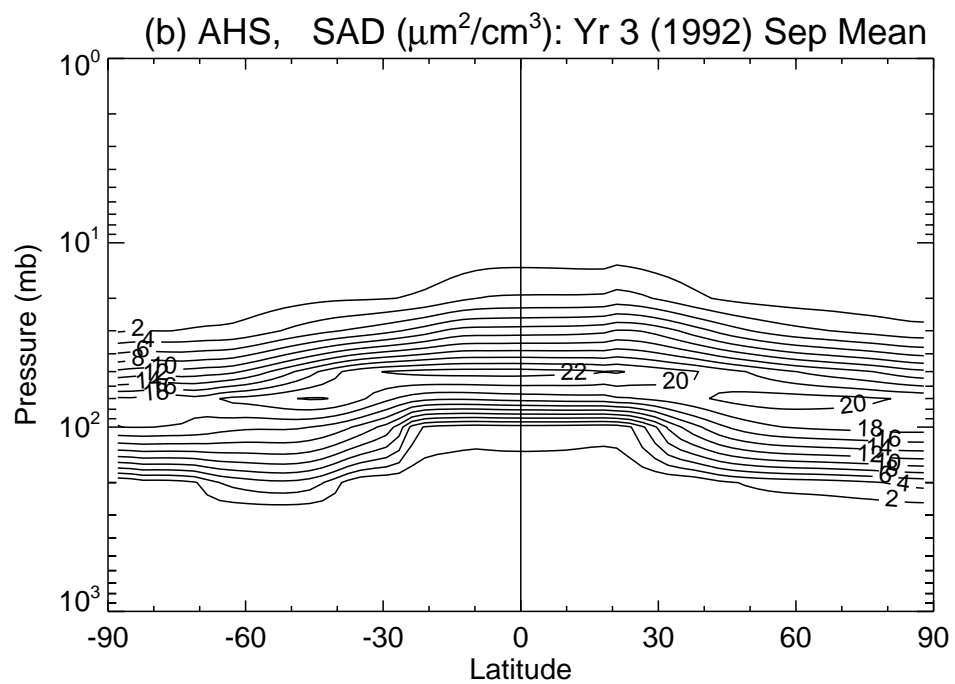
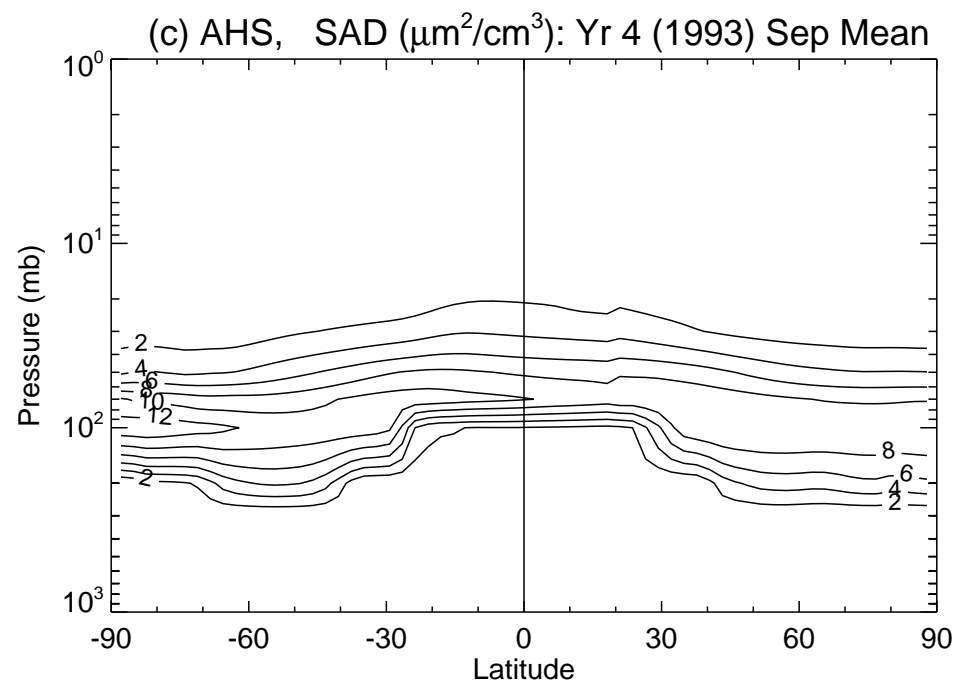
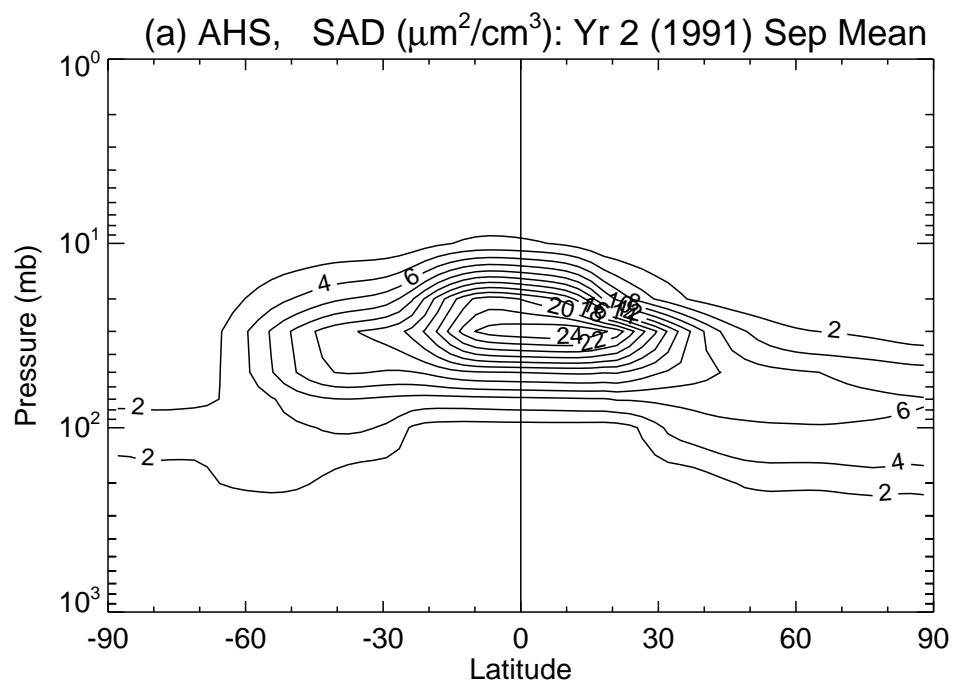


Figure 7

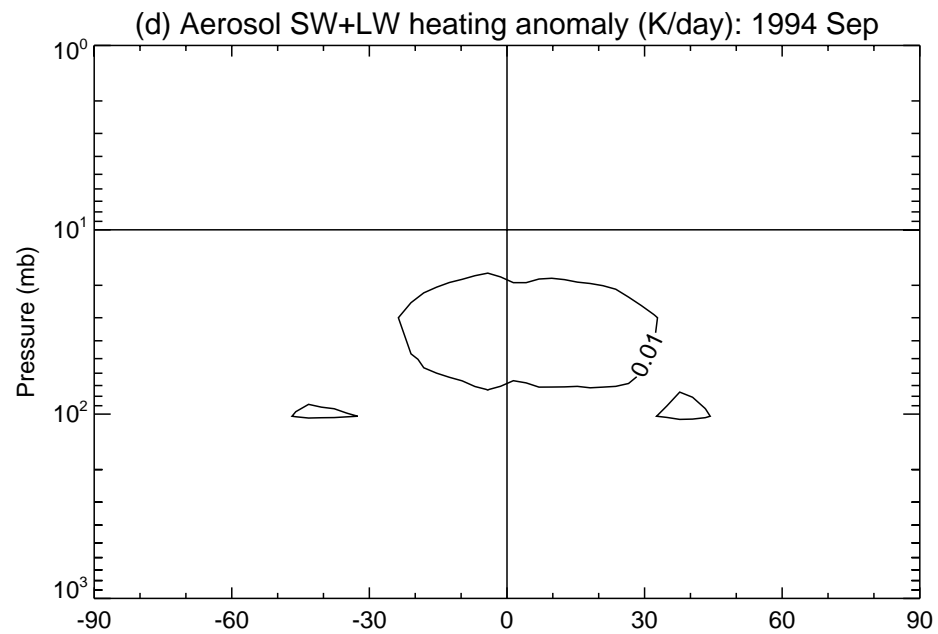
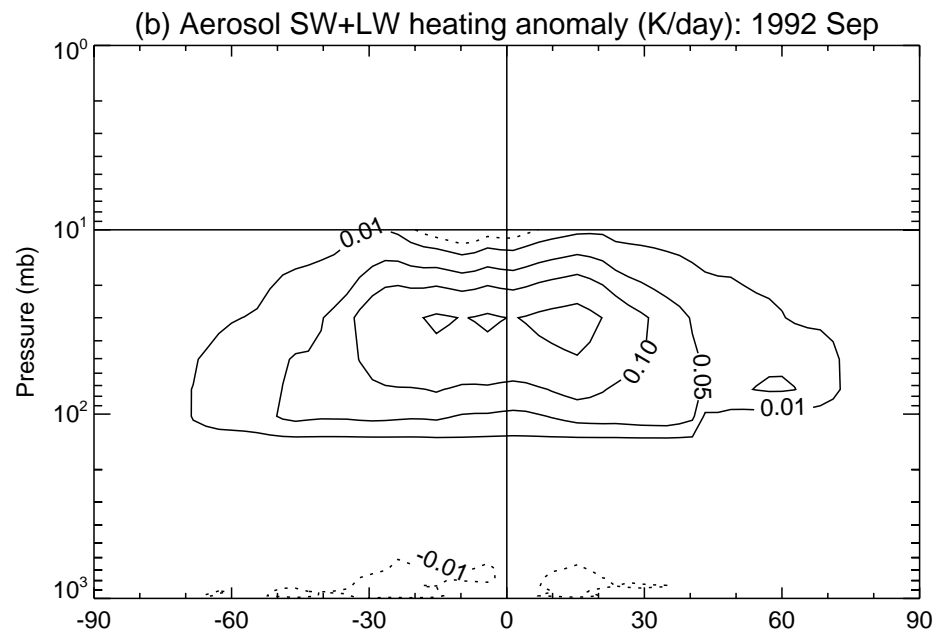
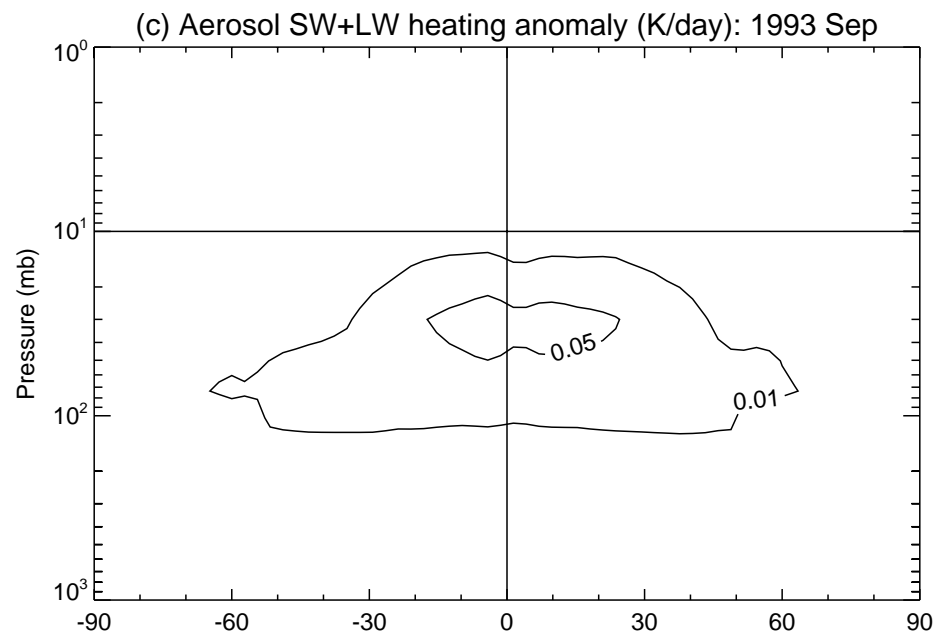
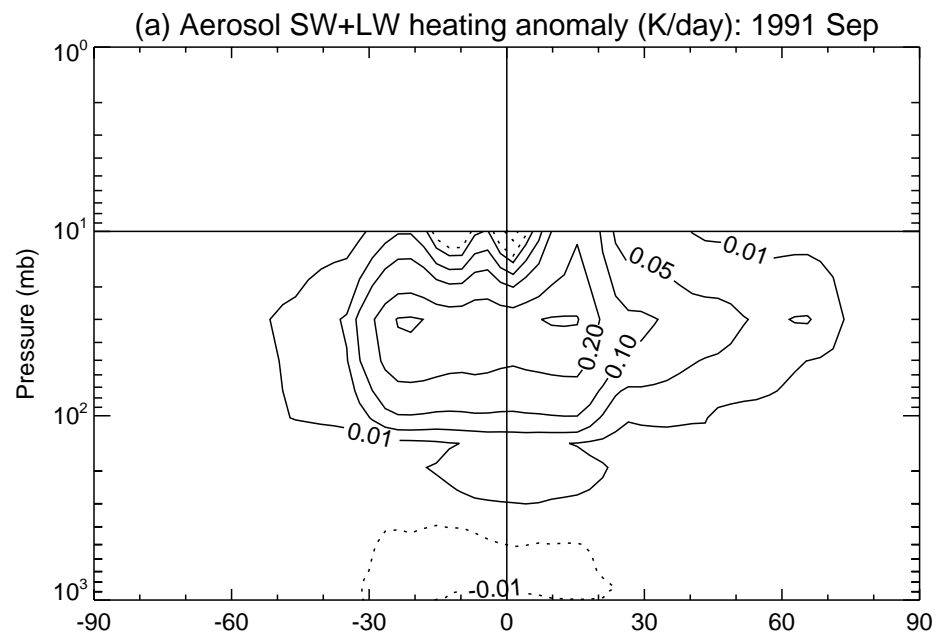


Figure 8

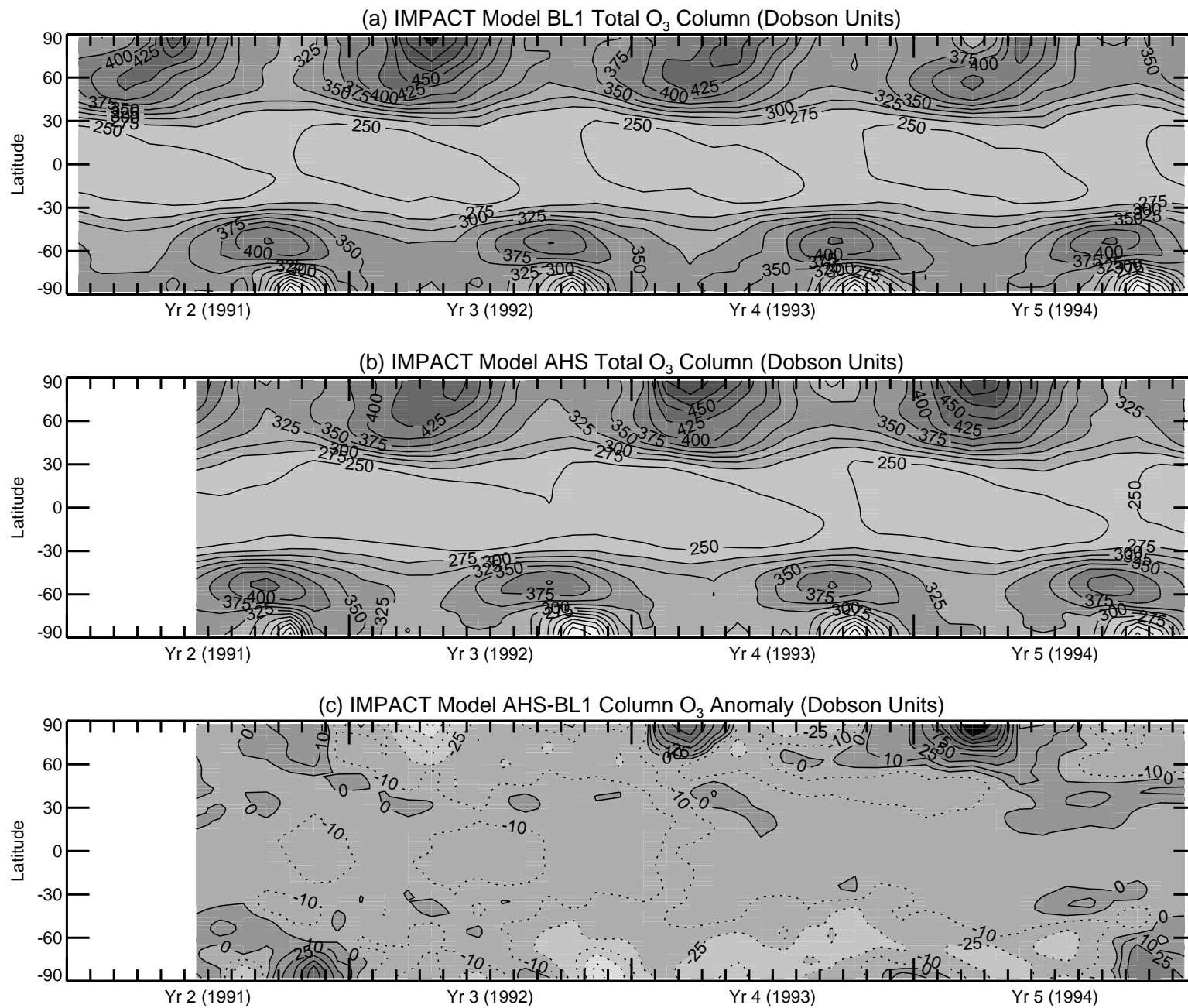


Figure 9



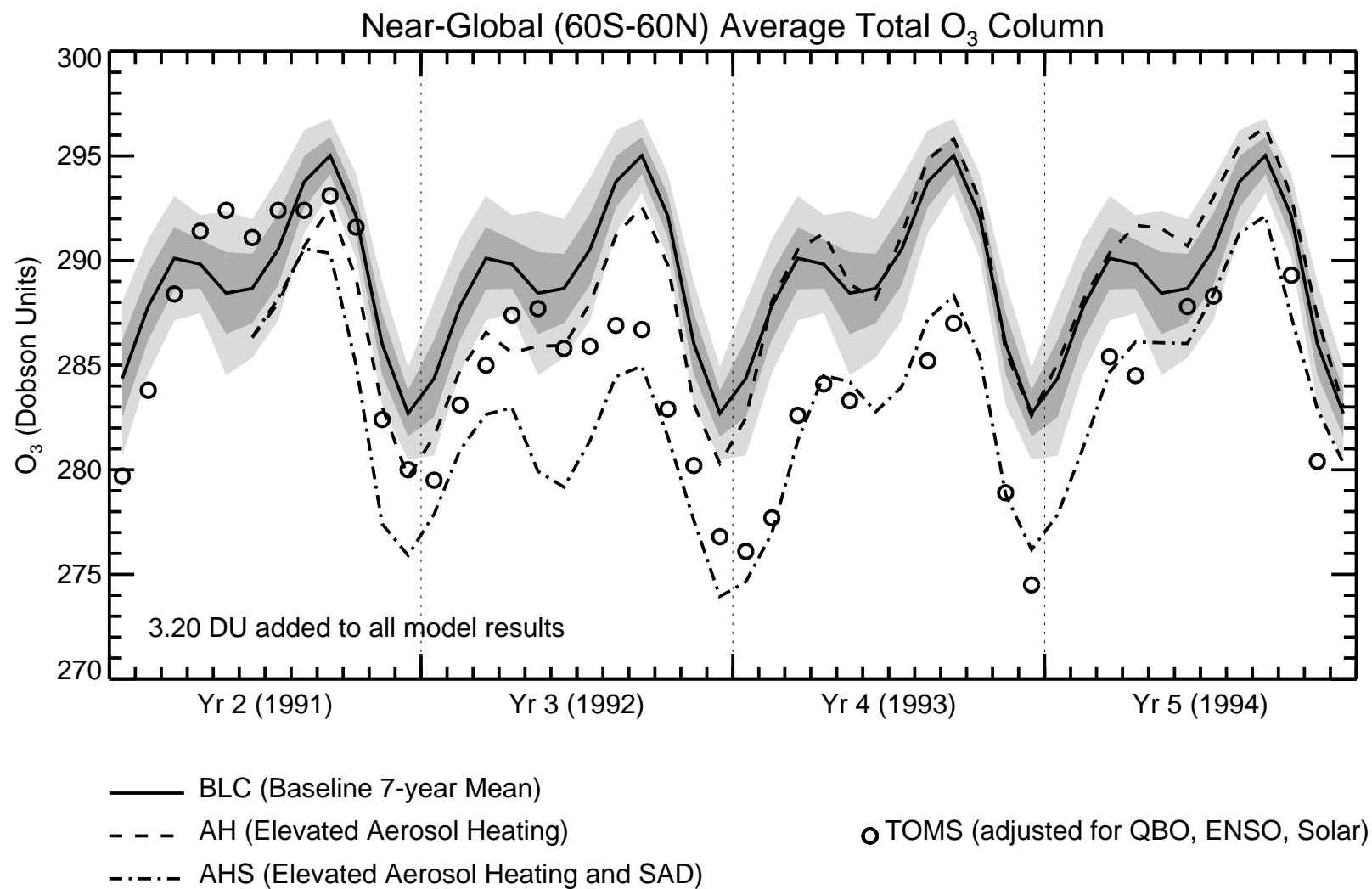


Figure 10

## Model Response of Column $O_3$ to Elevated Aerosol

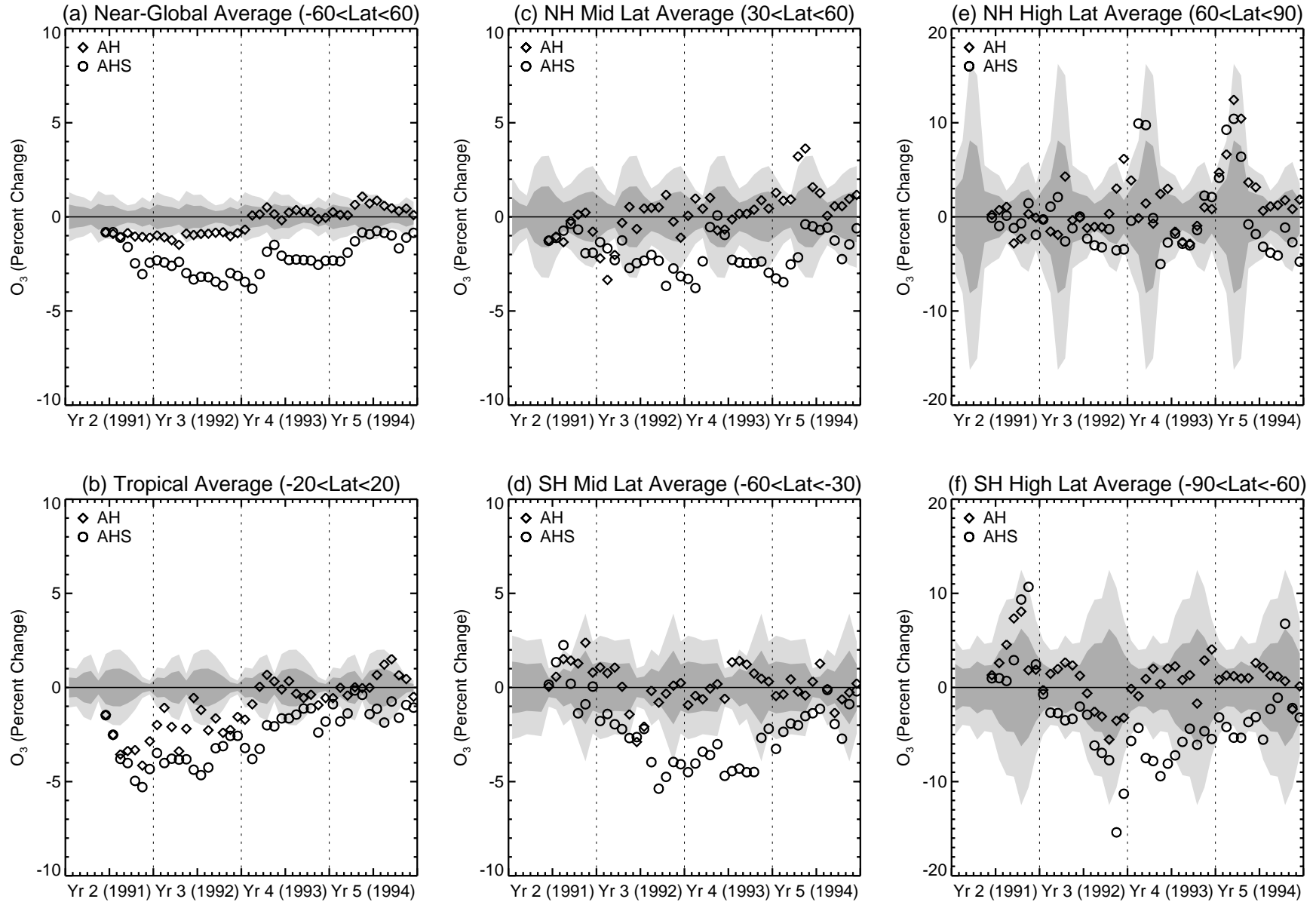


Figure 11

## TOMS Response of Column O<sub>3</sub> to Elevated Aerosol

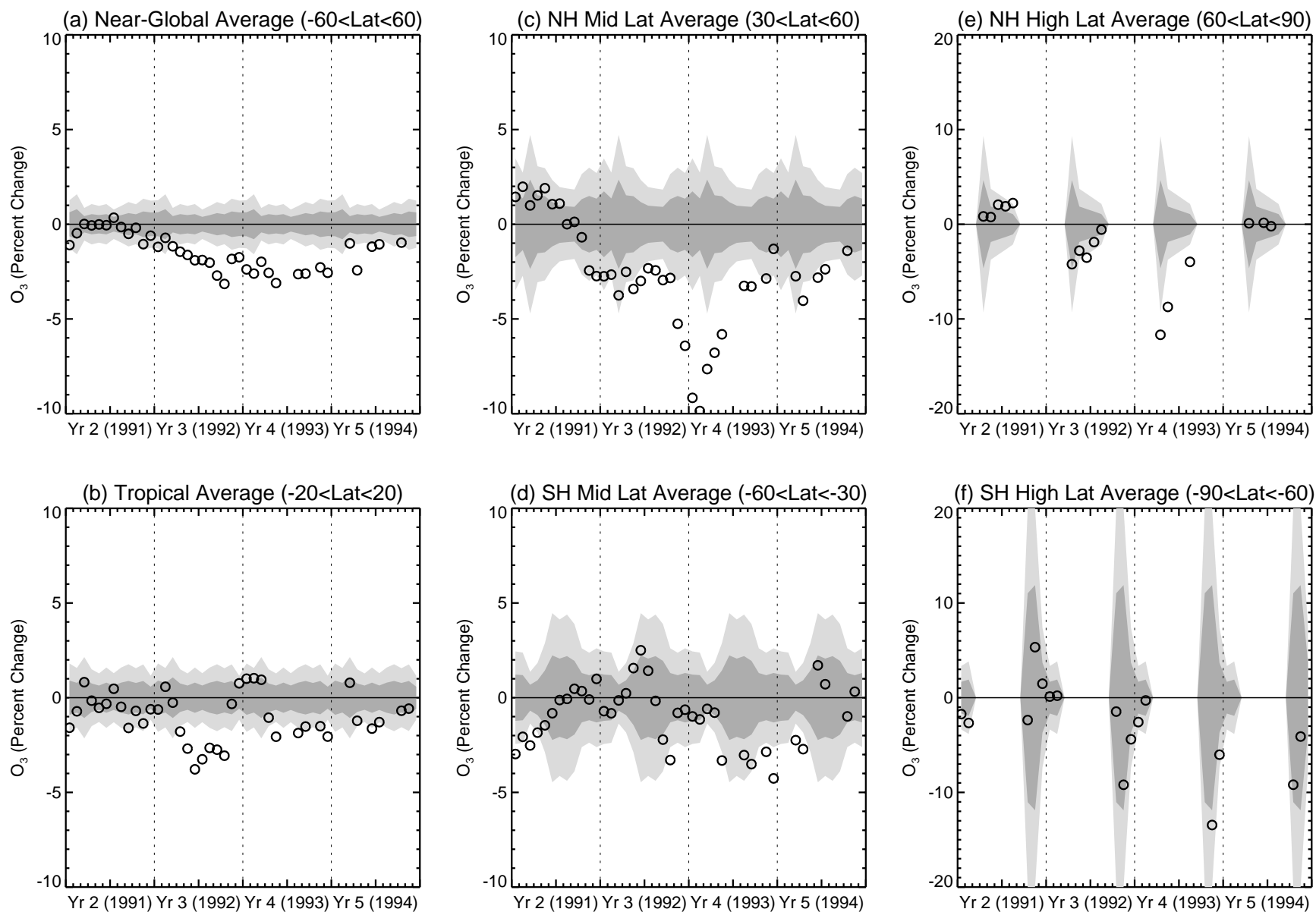


Figure 12



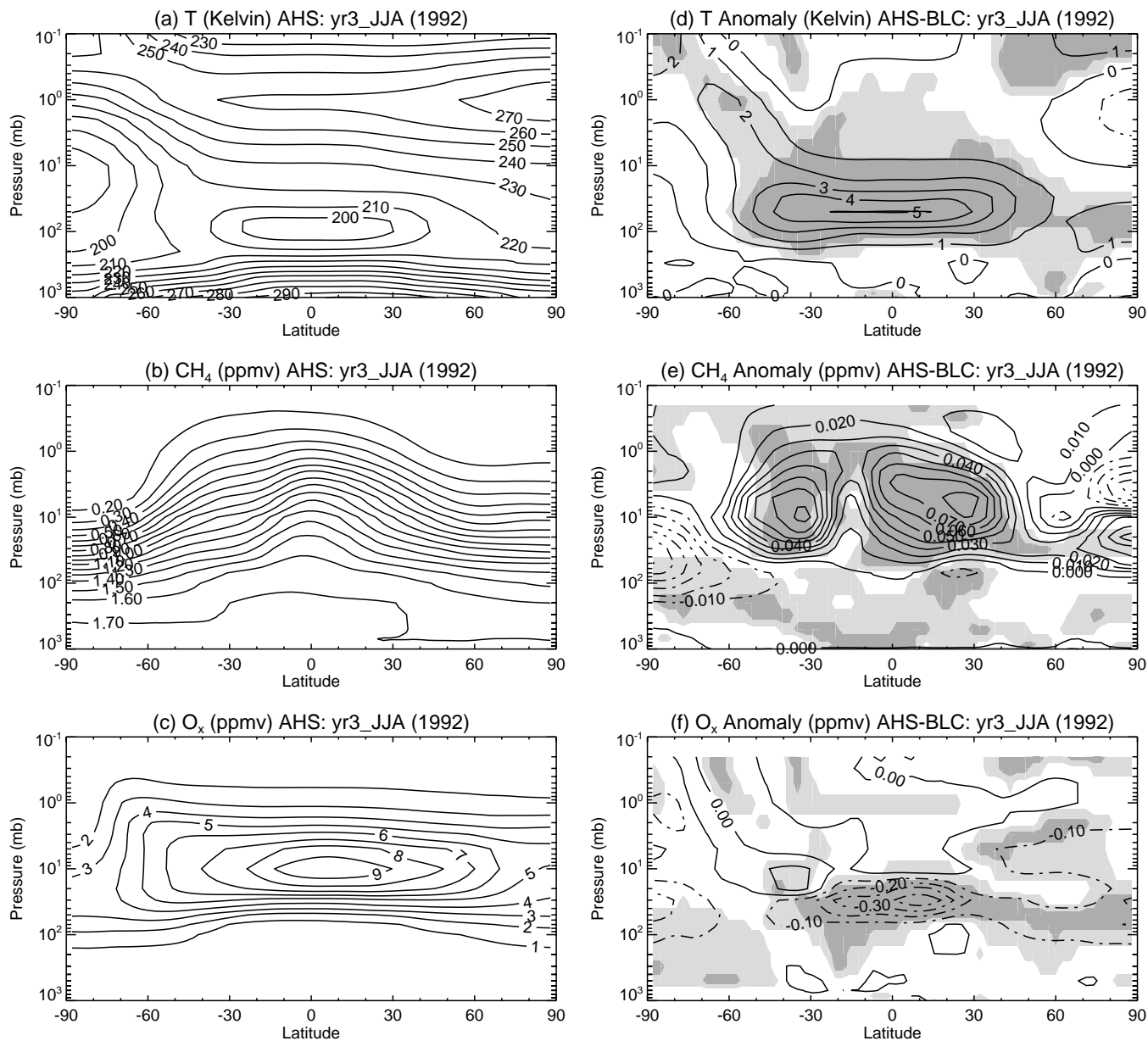


Figure 14

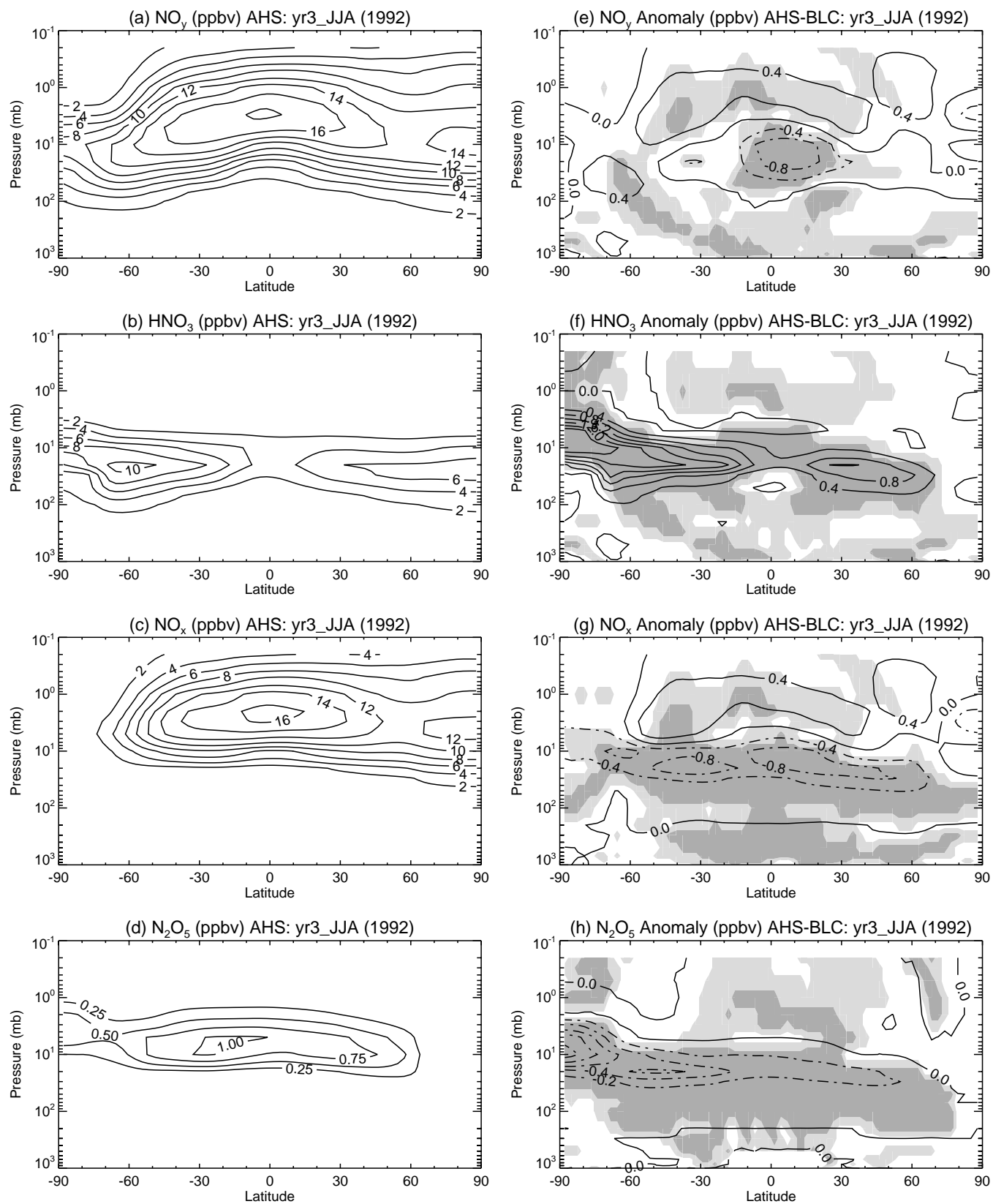


Figure 15

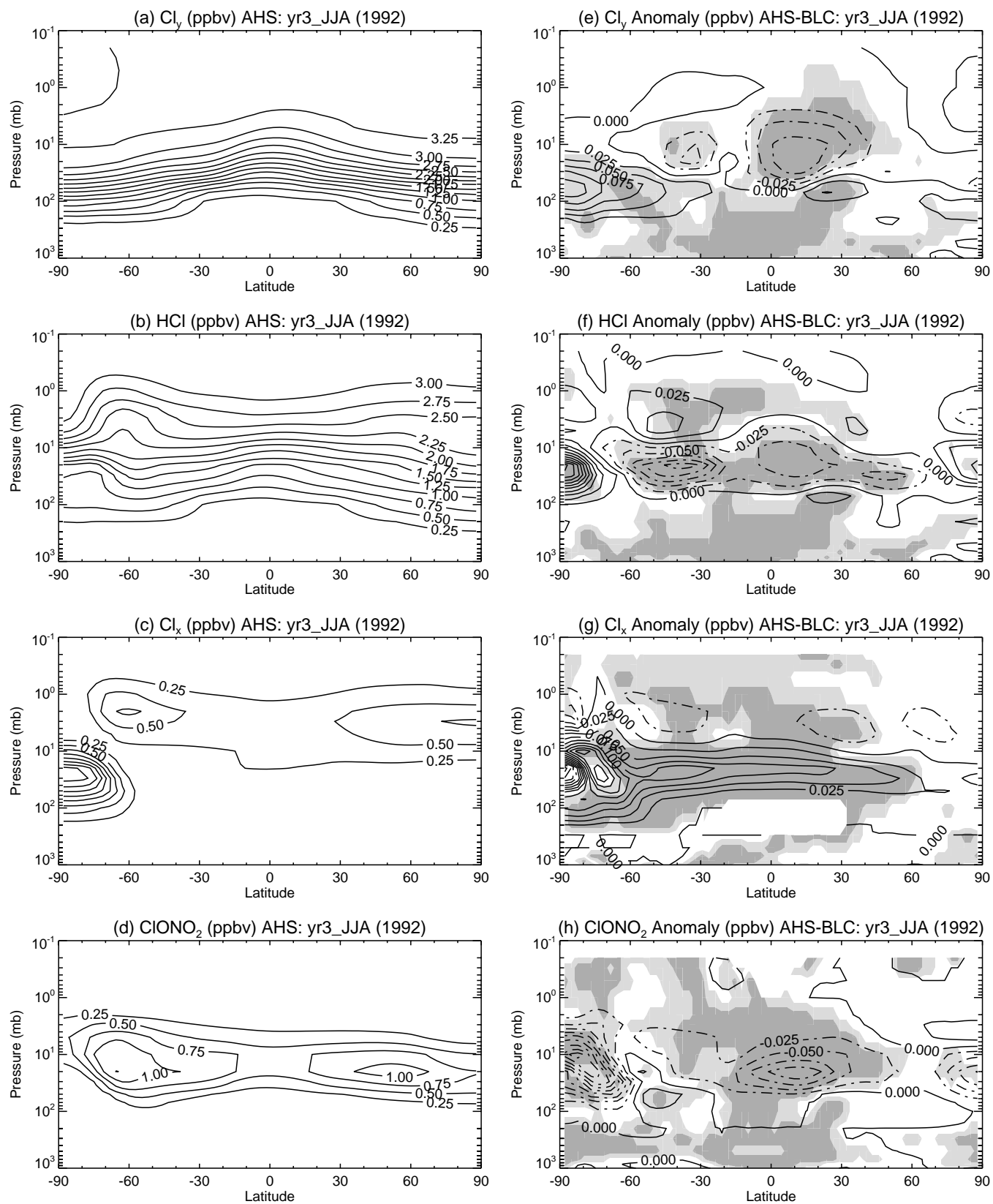


Figure 16

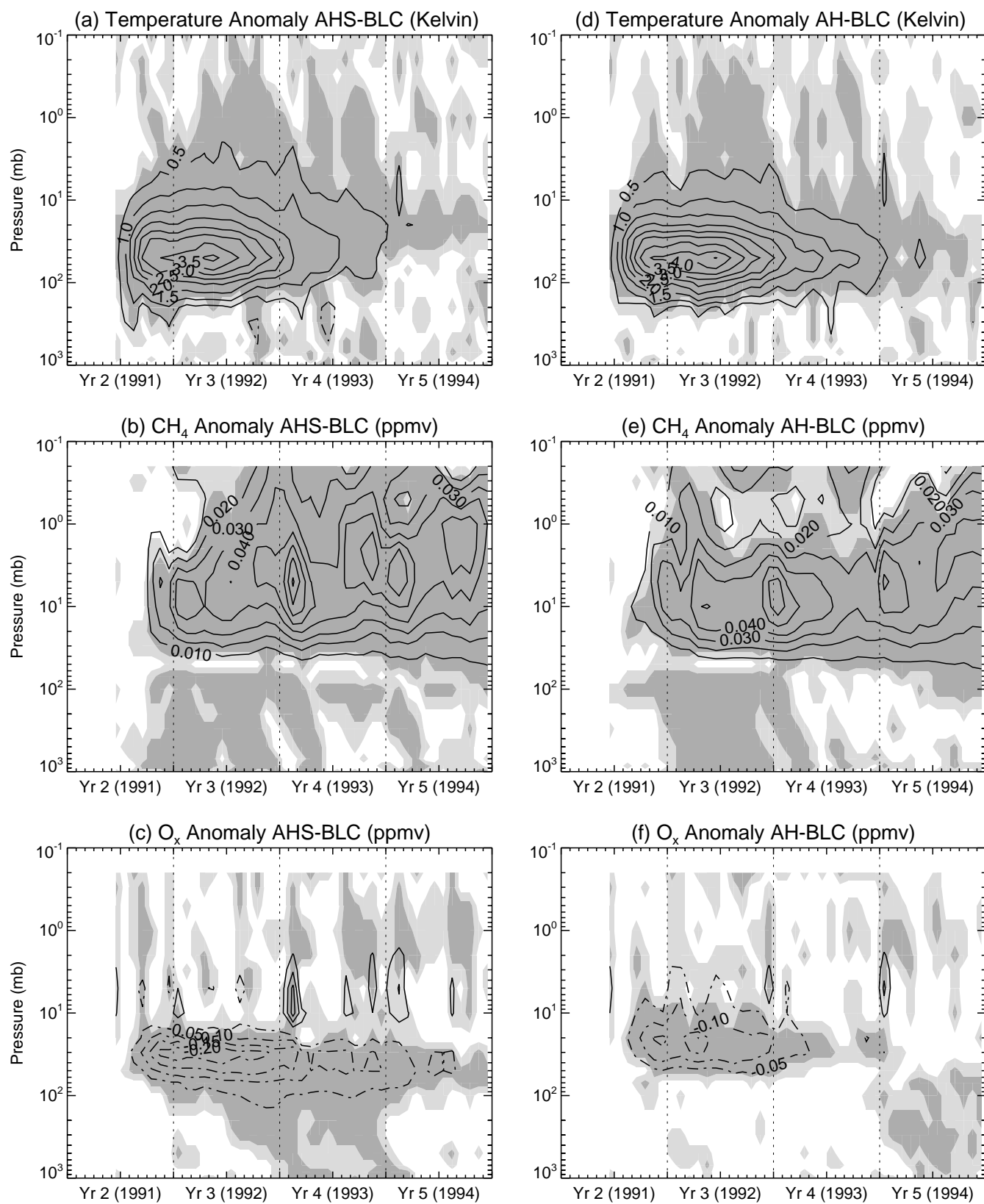


Figure 17



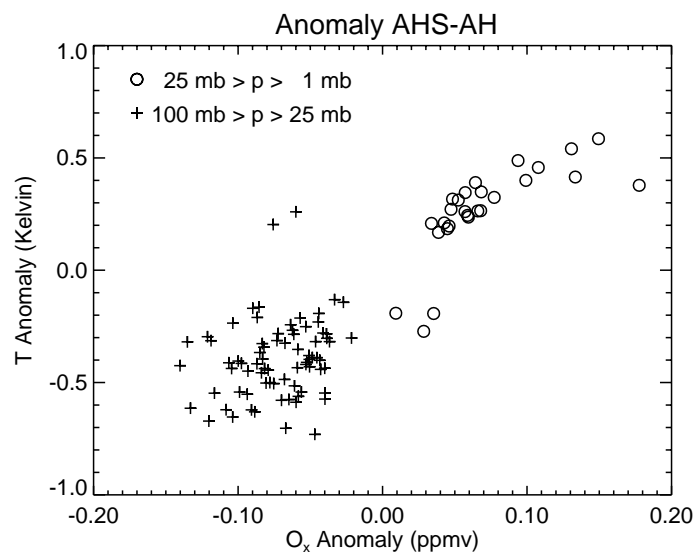


Figure 18

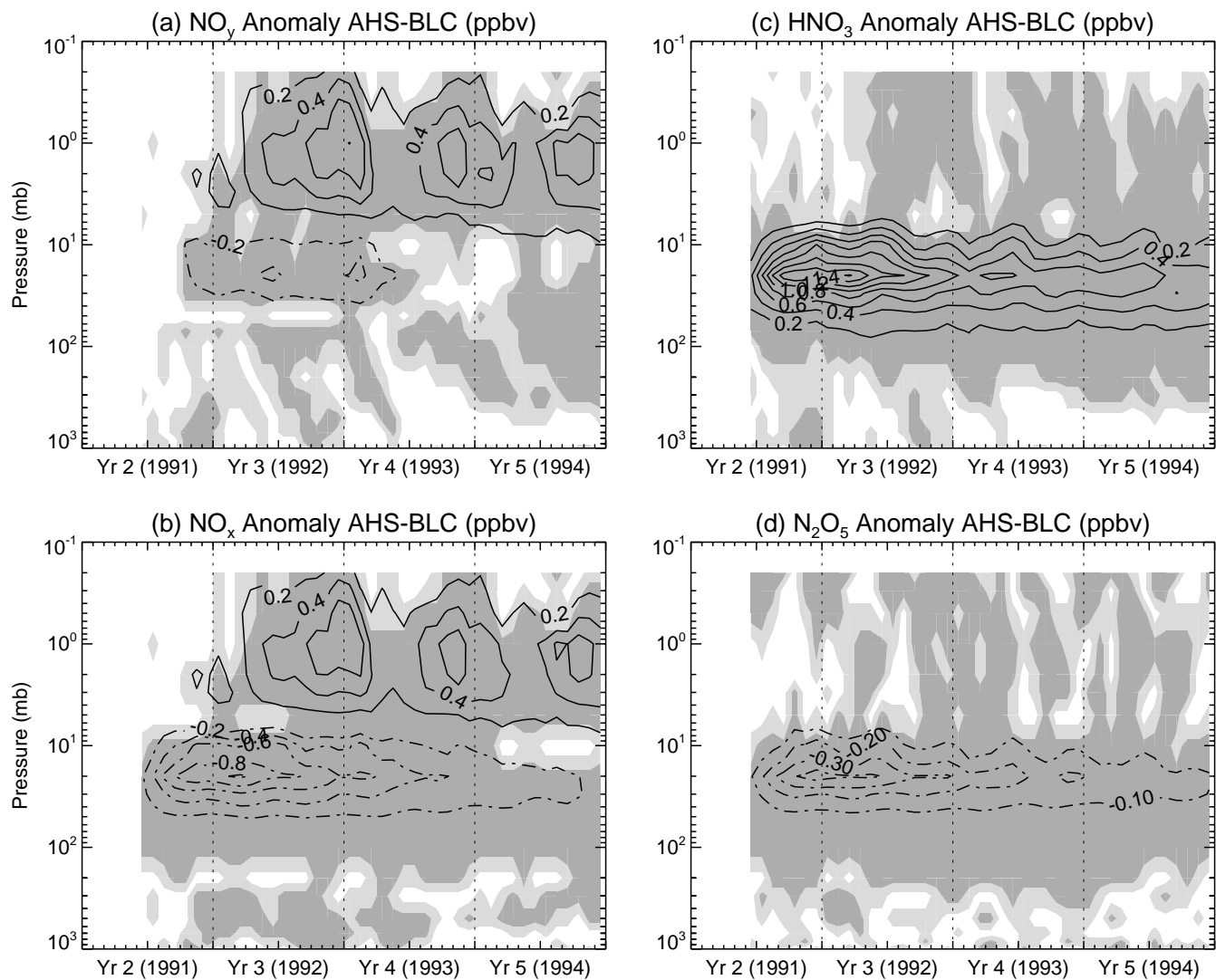


Figure 19

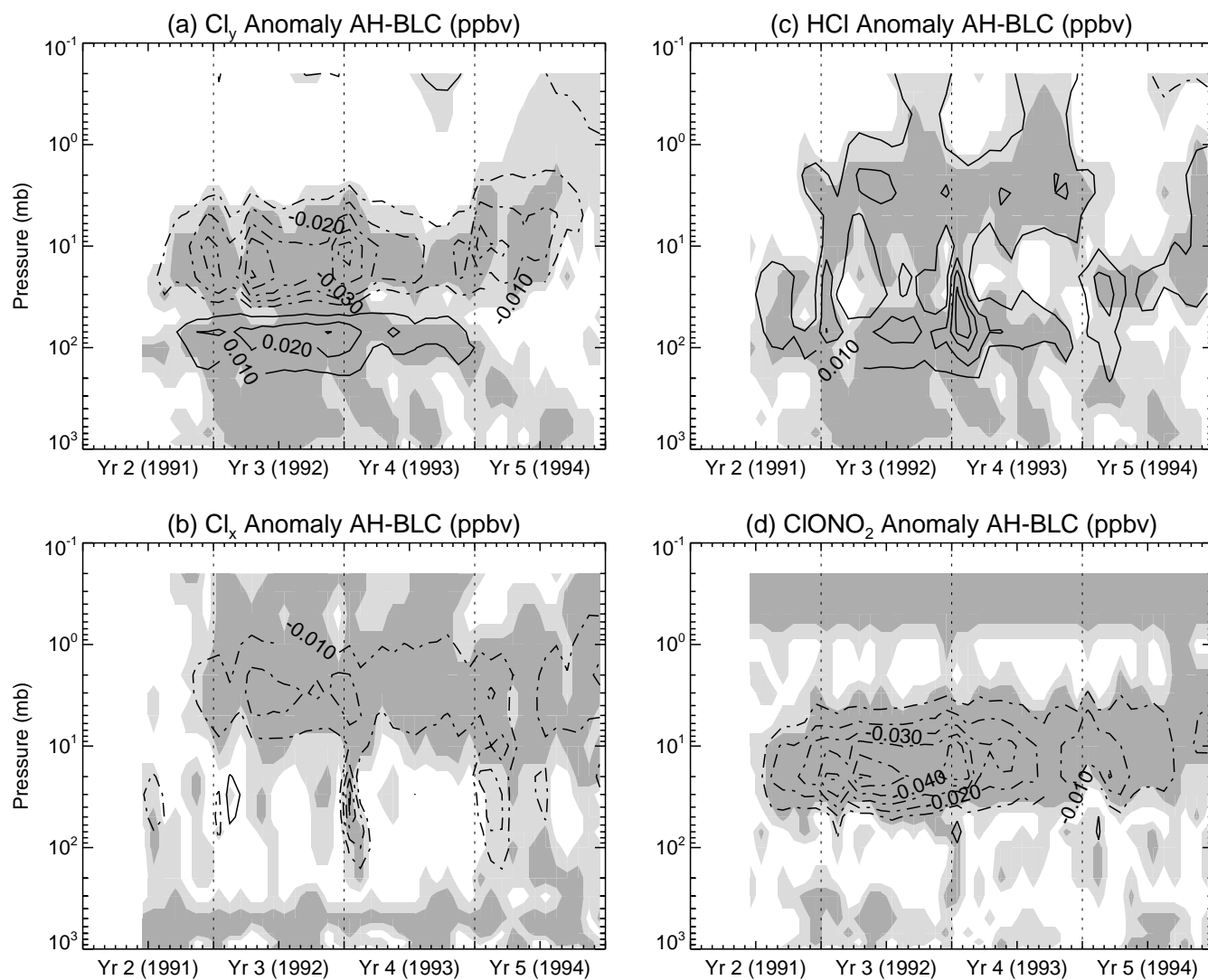


Figure 20

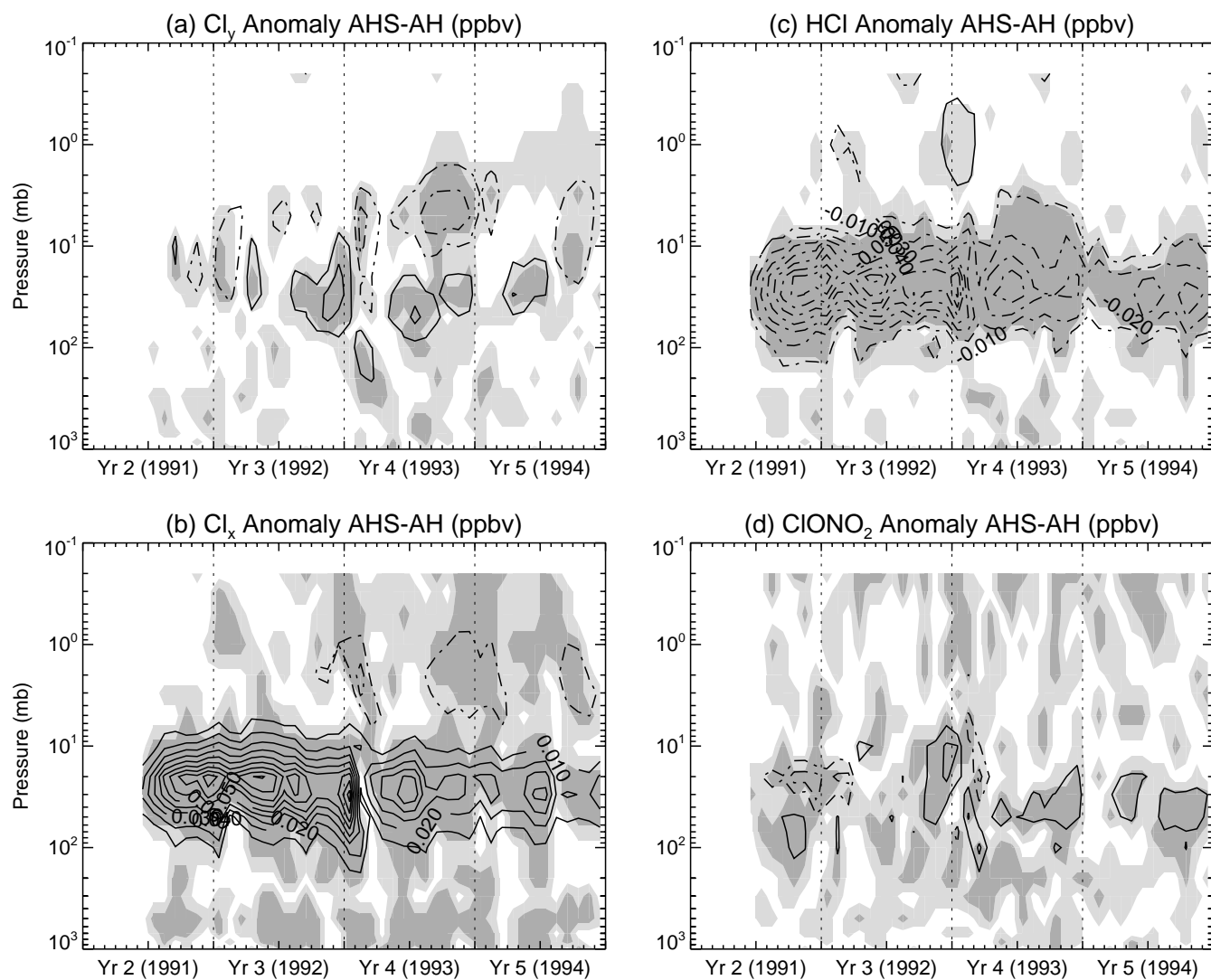


Figure 21

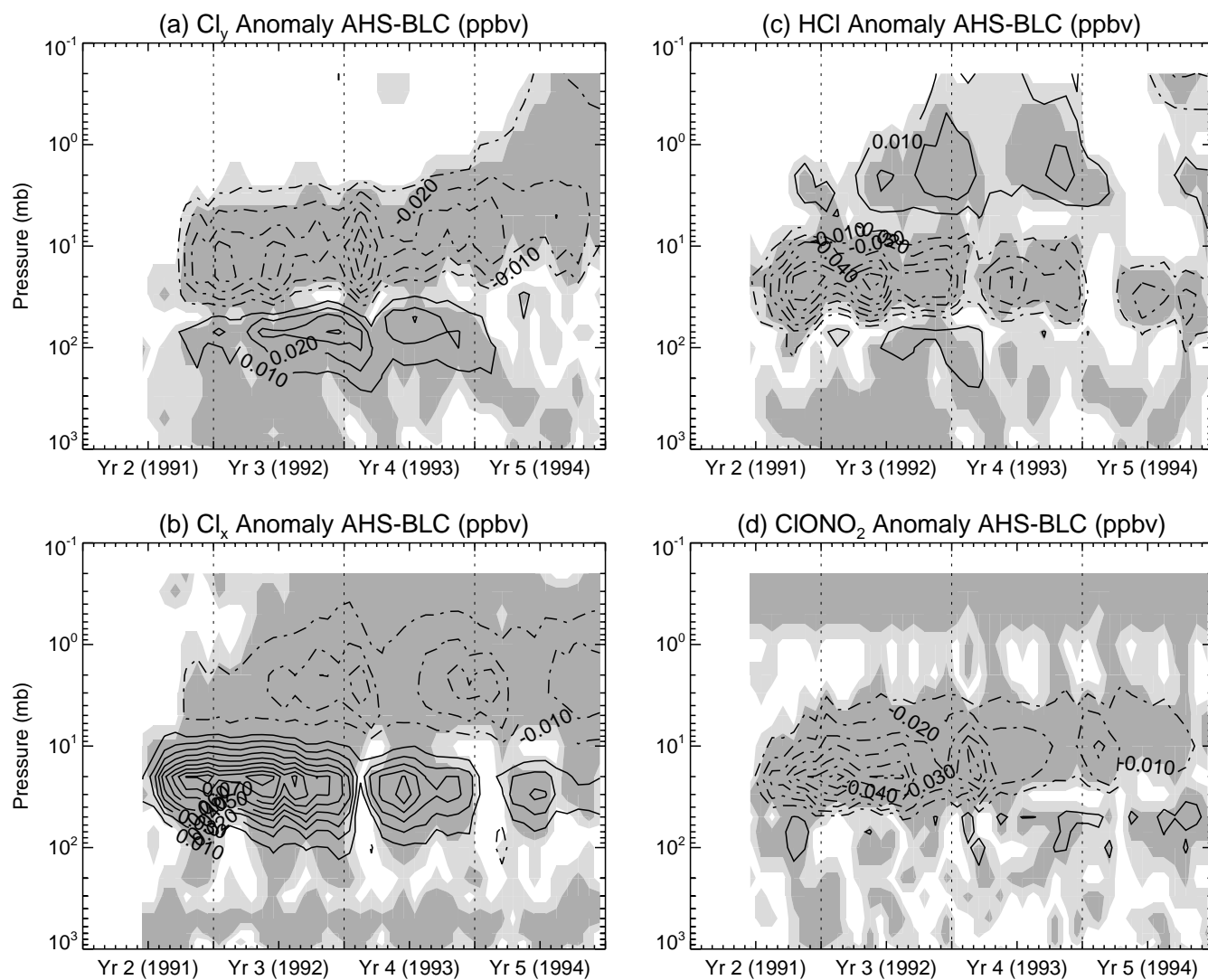


Figure 22

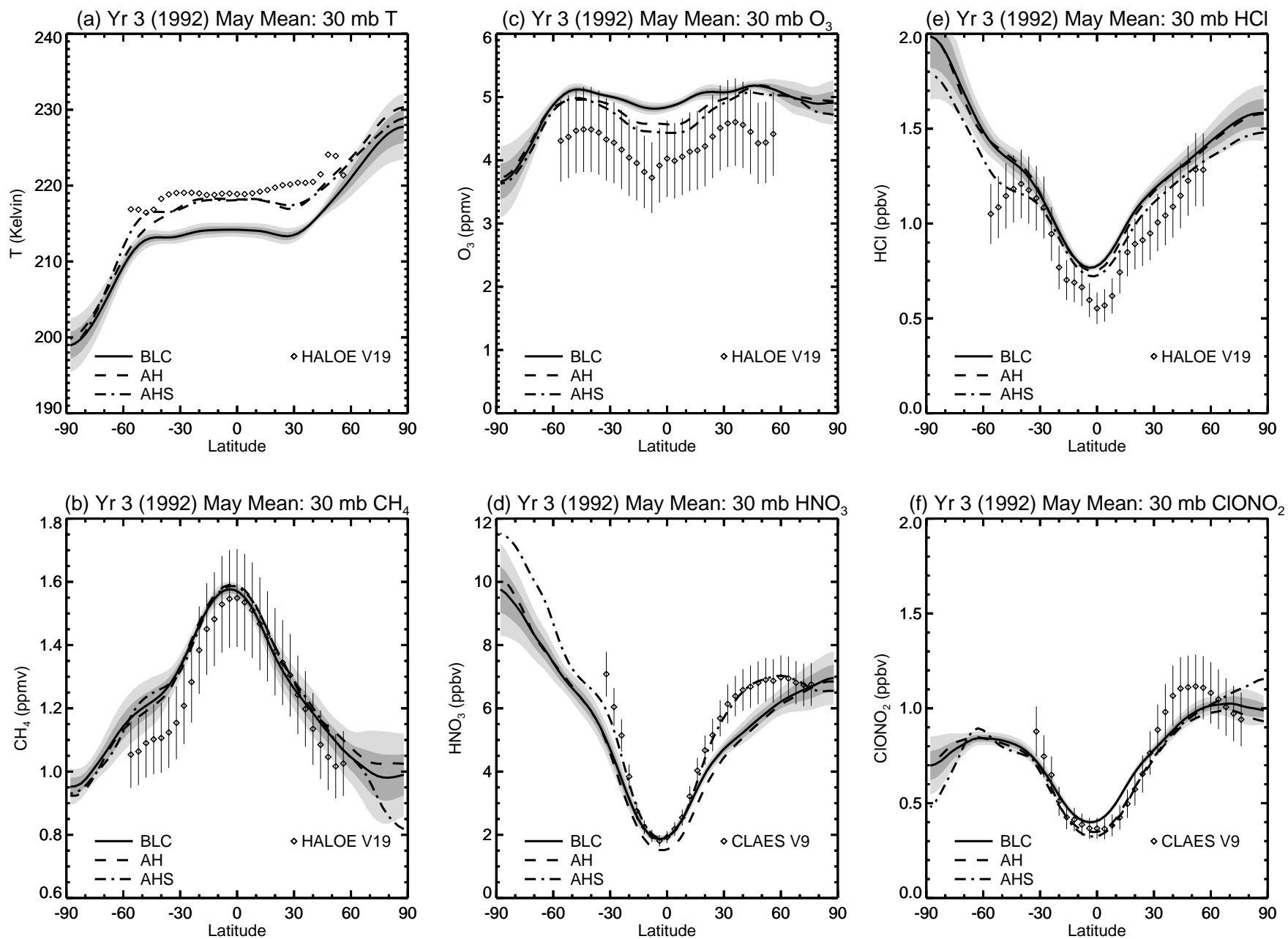


Figure 23

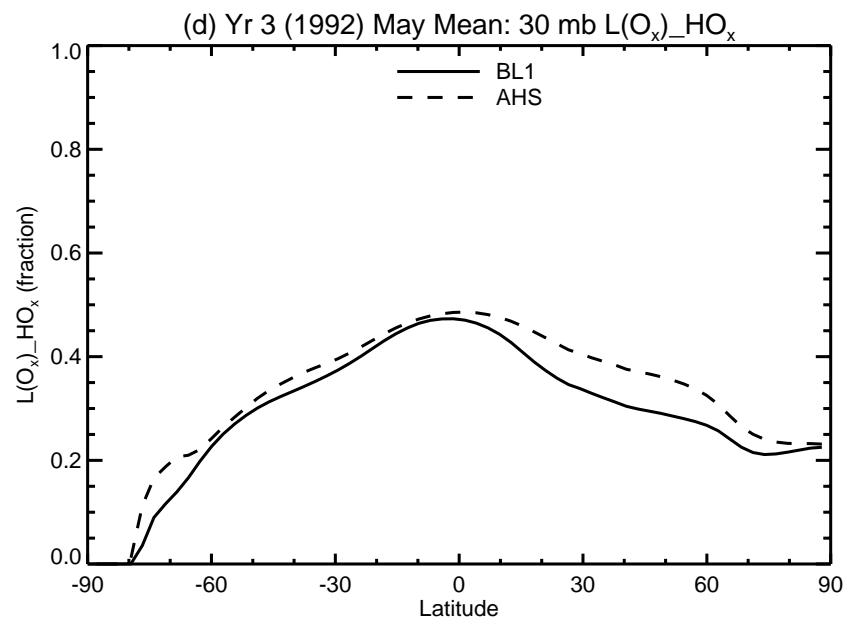
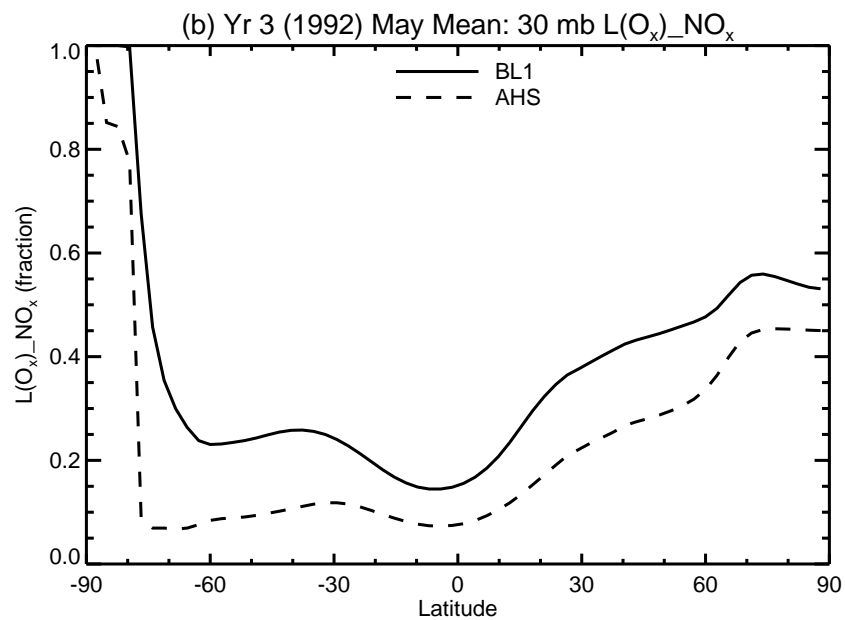
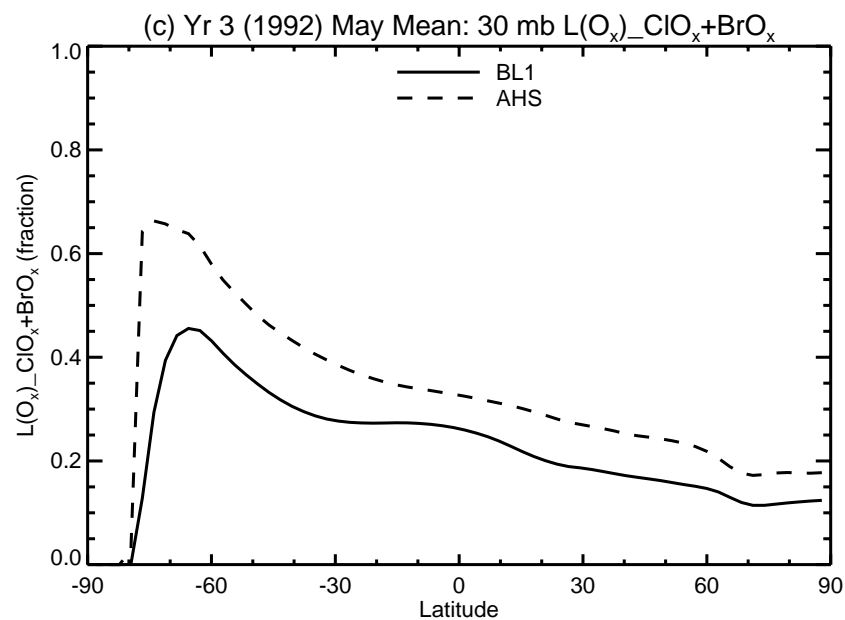
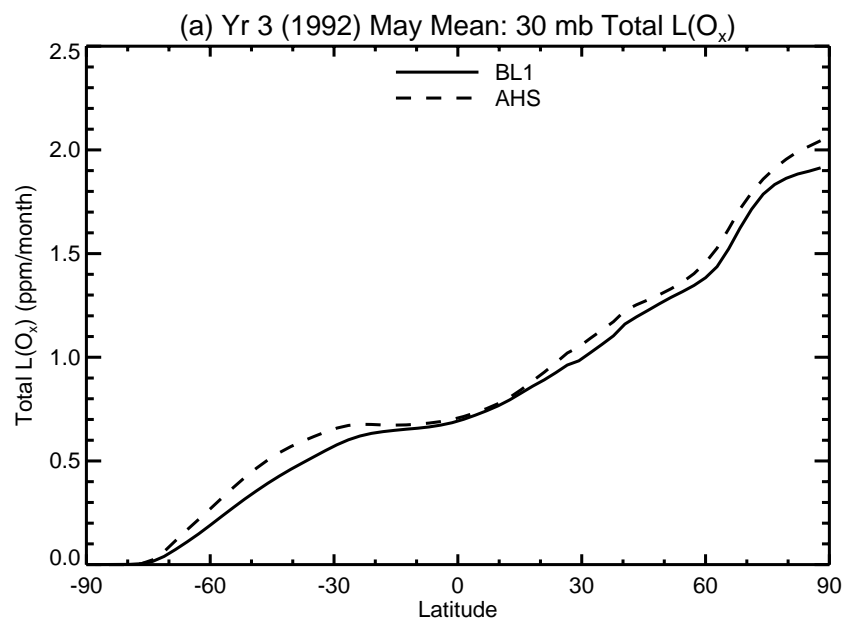


Figure 24

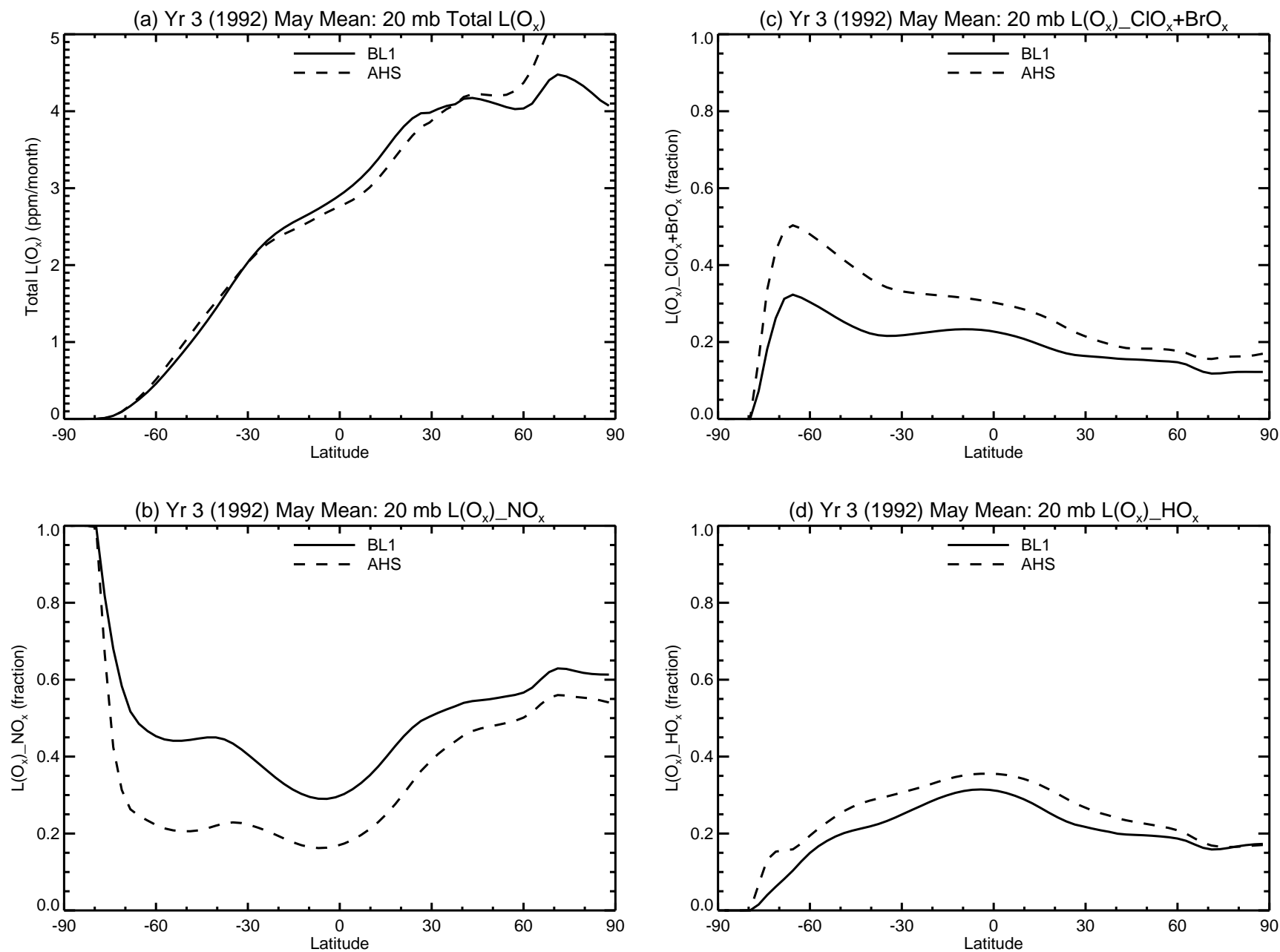


Figure 25